Search for Charged Higgs Bosons in Decays of Top Quarks in Proton-Antiproton Collisions at $\sqrt{s} = 1.96$ TeV

by

Geum Bong Yu

Submitted in Partial Fulfillment

of the

Requirements for the Degree

Doctor of Philosophy

Supervised by

Professor Arie Bodek

Department of Physics and Astronomy
Arts, Sciences and Engineering
School of Arts and Sciences

University of Rochester
Rochester, New York

2009

Curriculum Vitae

This author was born in Seoul, Republic of Korea in 1979. She attended Korea University from 1997 to 2001, and graduated with a Bachelor of Science degree in Physics. She went on to do graduate work at Korea University from 2001 to 2002, and graduated with a Master of Science degree in Physics. She came to the University of Rochester in 2003 and pursued research in experimental particle physics under the supervision of Professor Arie Bodek. She received a Master of Arts degree in Physics from the University of Rochester in 2005.

Acknowledgements

First of all, I thank to professor Arie Bodek, my thesis advisor, for his strong support to carry out this analysis at the Fermi National Accelerator Laboratory and for my participations in a variety of activities. He has guided me by directing the analysis and getting this dissertation written with clarity. His insight into the physics, endless curiosities, and passion for pursuing new knowledge inspired me on how a physicst should be. I am deeply thankful to you, Arie, again for the support during my years of graduate studies.

I am also very thankful to Yeonsei Chung and Un-ki Yang. We all discussed every single issue that arose in this analysis, and they have always stood by me through the years. Not only about physics, they also listened to me and cared about a variety of activities at Fermilab. I appreciate their kindness and patience with me. I also thank my long time office-mate, Willis Sakumoto. Working together on the CDF data logger, he showed me how to get technical issues solved and how to coordinate with coworkers in this gigantic experiment, with great patience. I am also deeply thankful to all members of the Rochester group, including Howard and Jiyeon, for their warm supports for me at CDF.

An analysis in high energy physics cannot be carried out by a single individual but requires that the collaboration work in harmony. I thank the members of the CDF collaboration, the laboratory staff, and the accelerator division. I appreciate the fruitful discussions with members of the top group who prompted me to look at the physics from different points of view. Among the group members, special thanks go to Veronica Sorin and Ricardo Eusebi for their patience with my endless questions about the physics and technical issues in the analysis.

Last but not least, I am deeply thankful to my parents. They always encouraged me to be aware of what I really want to do and have given me the strength to carry it out. Even though we were physically apart during my research for several years, they were a source of great support. I also thank all my friends at Fermilab and in Korea who acted as family, siblings, and sometimes as mentors regardless of the distance between us. I could not manage to come to this end without the heartful support of all these lovely people. I love you.

2009

Geumbong Yu

Abstract

In this dissertation we report on the first direct search for charged Higgs bosons in decays of top quarks in $p\bar{p}$ collisions at $\sqrt{s} = 1.96$ TeV. The search uses a data sample with an integrated luminosity of 2.2 fb^{-1} collected by the CDF II detector at Fermilab and looks for a resonance in the invariant mass distribution of two jets in the lepton+jets sample of $t\bar{t}$ candidates. We observe no evidence of charged Higgs bosons in top quark decays; hence 95% C.L. upper limits on the branching ratio are placed at $\mathcal{B}(t \rightarrow H^+b) < 0.1$ to 0.3 for charged Higgs boson masses of 60 to 150 GeV/c^2 assuming $\mathcal{B}(H^+ \rightarrow c\bar{s}) = 1.0$ and $\mathcal{B}(t \rightarrow Wb) + \mathcal{B}(t \rightarrow H^+b) = 1.0$. The upper limits on $\mathcal{B}(t \rightarrow H^+b)$ are also used as model independent limits on the decay branching ratio of top quarks to any charged scalar bosons beyond the standard model.

Table of Contents

List of Tables

List of Figures

Chapter 1

Introduction

The basic history of particle physics is outlined, emphasizing the motivation of this dissertation.

The field of Physics originated with the hypothesis of ancient western philosophers that all matter can be broken down to smaller pieces until reaching the ultimate unbreakable piece which they called the atom. Further understanding of the atom did not occur until the development of the field of chemistry. In the 19^{th} century the existence of atoms was inferred from the observations of microscopic phenomena such as Brownian motion and from studies of chemical compounds. In the beginning of the 20th century, it was determined that the atom is a bound state composed of a nucleus surrounded by a cloud of electrons. Later, the nucleus was discovered to be composed of neutrons and protons. In the latter half of the 20th century, nucleons were discovered to be composed of quarks, as illustrated in Fig. 1.1.

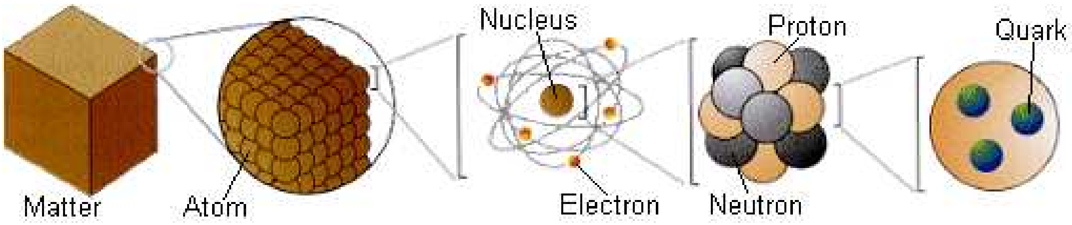

Figure 1.1: The composition of matter.

The 20^{th} century was a very exciting period in the history of physics. During that time, many physicists attempted to understand the phenomena of the subatomic world through a combination of various experiments as well as through a variety of novel theoretical ideas. Unlike everyday phenomena which are governed by gravity and the electromagnetic (EM) force, the subatomic world is governed by the EM and two additional forces: the strong and the weak interactions. The strong interaction binds protons (which are positively charged) and neutrons (a neutral twin of the proton) to one another to form a nucleus in spite of the repulsive EM forces between protons. Therefore, the strong force is known to be stronger than the EM force at short distances, i.e. at the scale of the size of the nucleus ($\sim 10^{-14}$m). The weak interaction was discovered from the radioactive β decay of a neutron to a proton and an electron (and a neutrino as was determined later). The weak interaction also only occurs at very short range. A significant achievement of the 20^{th} century physics is the unification of the strong, weak, and EM interactions using the gauge group theory of SU(3) × SU(2) × U(1). This unified theory is referred to as the standard model (SM) [1] of particle physics.

Although the SM is very successful in our understandings of subatomic physics, the model fails to address several important questions. For example, there are no explanations for gravity - the weakest force in subatomic scale, or dark matter, or non-zero neutrino masses. An important unresolved question is the mechanism of electroweak symmetry breaking (EWSB), which gives masses to weak bosons ($W^{\pm}$, Z^0) and fermions[1]. In the SM, the mechanism of EWSB is understood by introducing a single complex scalar doublet field, which can manifest in a new observable Higgs boson [2]. However, the Higgs boson has not been experimentally observed. Searches for the Higgs boson have received top priority in experimental particle physics.

Many diverse hypotheses beyond the SM have been proposed to resolve the questions that are not accounted for in the SM. Among all the hypothesis, the theory of supersymmetry (SUSY) has been the leading contender. SUSY proposes a new boson-fermion symmetry; every known boson has its super partner fermion

---

[1] Fermions are particles with half-integer spin. In the SM, the fundamental particles are fermions (six quarks and six leptons). Bosons are integer-spin particles. The fundamental particles in the SM are described in Sec. 2.1.

and vice versa. In the theory of SUSY, there are a number of branches which depend on additional assumptions. Among the various branches, the most widely used hypothesis is the minimal supersymmetric extension of the standard model (MSSM) [3]. It uses type II of the two complex Higgs doublets model for EWSB. This model predicts two charged ($H^{\pm}$) and three neutral (h^0, H^0, A^0) observable Higgs bosons. In particular, the charged Higgs boson does not have an analogous candidate in the SM. Therefore, observation of the charged Higgs bosons would provide crucial evidence for the existence of new physics beyond the SM.

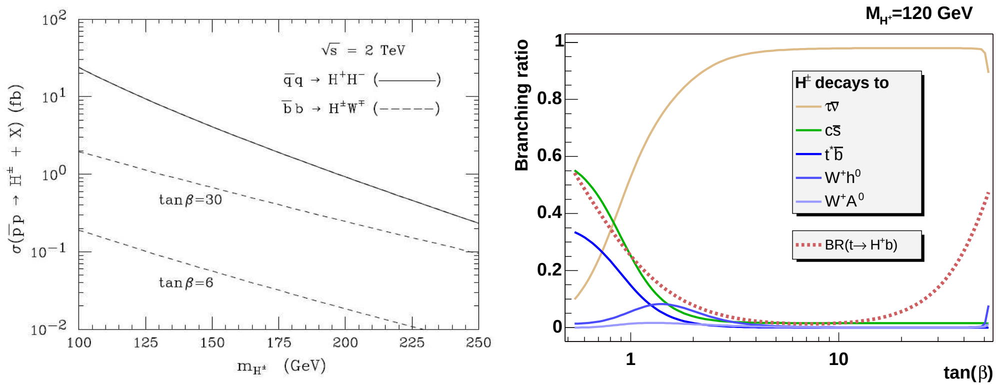

Figure 1.2: Direct charged Higgs production cross section at the Tevatron [4] (left) and $\mathcal{B}(t \rightarrow H^+b)$ with various H^+ decay branching ratios as a function of $\tan\beta$. In the right plot, the branching ratio of 120 GeV/c^2 H^+ is computed using CPsuperH program [5] [6].

In this dissertation we focus on a search for a charged Higgs boson that could originate from decays of top quarks.[2] At the Tevatron, the direct production cross section of the charged Higgs is smaller than other SM processes by a factor of a thousand. Therefore, it is easier to search for charged Higgs in decays of a SM particle. Figure 1.2 shows the predictions for the direct production cross section of H^+ at the Tevatron (left) and the top quark decay branching ratio to H^+b, $\mathcal{B}(t \rightarrow H^+b)$, (right). Within MSSM the branching ratio $\mathcal{B}(t \rightarrow H^+b)$ and various H^+ decay modes are determined from two parameters which are not known a priori: the mass of the charged Higgs (m_{H^+}) and $\tan\beta$. The parameter

---

[2] Top quark is the heaviest quark in the SM. The top quark mass has been measured to be 172.4 GeV/c^2, which is 180 times heavier than the mass of the proton.

$\tan\beta$ is the ratio of the vacuum expectation values of the two Higgs doublets. As described in the right plot of Fig. 1.2, the branching ratio $\mathcal{B}(t \to H^+b)$ is large for either low ($\lesssim 1$) or high ($\gtrsim 15$) values of $\tan\beta$ [4]. The prediction of H^+ decay modes also vary with m_{H^+} as shown in Fig. 1.3. Assuming $m_{H^+} < m_t - m_b$ in very low $\tan\beta$ region, H^+ predominantly decays into $c\bar{s}$ for low m_{H^+} ($\lesssim 130$ GeV/c^2) and $t^*\bar{b}$ ($\to W^+b\bar{b}$)[3] for high m_{H^+}. As $\tan\beta$ increases, the $H^+ \to \tau^+\nu$ decay mode becomes dominant. For $m_{H^+} > m_t$, $\mathcal{B}(H^+ \to tb)$ is dominant regardless of $\tan\beta$.

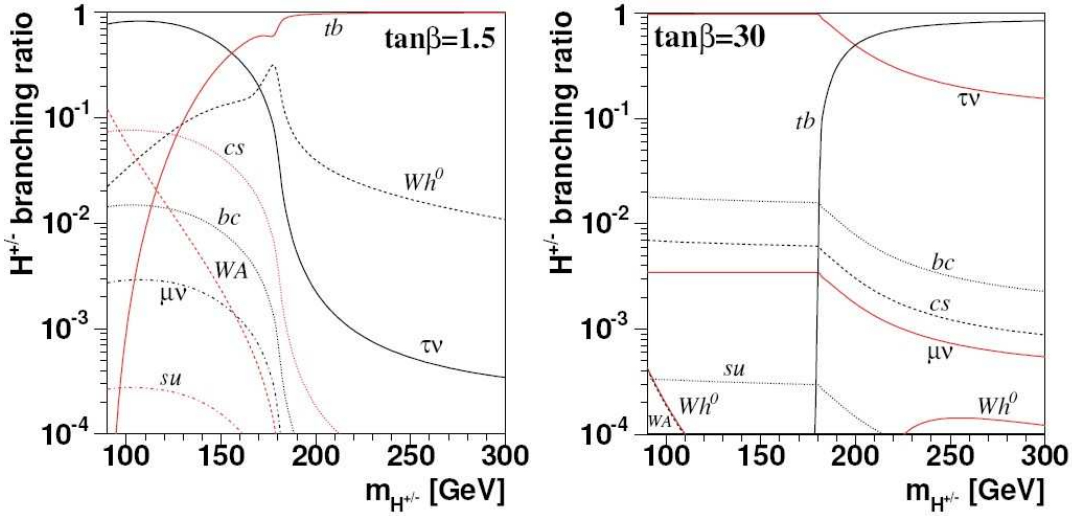

Figure 1.3: Decay branching ratios for the charged Higgs boson in MSSM in the maximal mixing scenario [7] as a function of m_{H^+}, assuming $\tan\beta = 1.5$ (left) and $\tan\beta = 30$ (right) [8].

This dissertation reports on the first direct search for $H^+ \to c\bar{s}$ in top quark decays using a fully reconstructed charged Higgs mass. In this analysis, we use lepton+jets $t\bar{t}$ candidates in $p\bar{p}$ collisions at a center of mass energy of 1.96 TeV. The data sample was collected by the CDF II detector at Fermilab from March 2002 to August 2007, corresponding to an integrated luminosity of 2.2 fb^{-1}. The theoretical background and current experimental limits for charged Higgs searches are introduced in chapter 2. Chapter 3 describes the Tevatron accelerator and the

---

[3] t^* is a virtual top quark with an off-shall mass.

CDF II detectors at the Fermi National Accelerator Laboratory. Details of the $t\bar{t}$ event selection criteria and investigations of the selected events using simulation samples are discussed in chapter 4. In chapter 5, the method for the charged Higgs search is demonstrated with $t\bar{t}$ Monte Carlo simulation samples ($t \to H^+b$ and $t \to Wb$). The results of the charged Higgs search using 2.2 fb^{-1} CDF II data and the prospect for future H^+ analyses are discussed in chapter 6.

Chapter 2

Theory and Previously Published Limits

This chapter introduces the theoretical background of the SM and its minimal supersymmetric extension which includes a charged Higgs boson. In addition, current published limits on the charged Higgs are summarized.

2.1 The Standard Model

The standard model is a gauge theory which describes the fundamental particles and their interactions. The standard model was initially formulated by Glashow, Weinberg, and Salam in late 1960s. The model unifies the electromagnetic (EM) and weak forces, resulting in a single electroweak interaction [1]. In the 1970s, the unification has been extended to include the theory of Quantum Chromo Dynamics (QCD), which describes the strong interaction between the quarks. The three interactions (strong, electromagnetic, and weak) are expected to be unified ($\mathrm{U}(1) \times \mathrm{SU}(2) \times \mathrm{SU}(3)$) at very high energies. To date, all predictions of the SM are in impressive agreement with experimental data.

In the SM, the fundamental constituents of matters are all fermions (half-integer spin particles) which include six quarks, six leptons, and their antiparticles. The quarks and leptons are grouped into three generations in order of increasing mass as shown in Fig. 2.1. Aside from the neutrinos, the heavy 2^{nd}

and 3rd generation fermions are unstable and quickly decay into lower mass quarks and leptons of the first generation: u, d, e, and neutrinos. One difference between quarks and leptons is the electrical charge. The $u(d)$-like quarks carry a charge of +2/3e ($-1/3e$). The $e(\nu_e)$-like leptons carry a charge of -1e (0). The other significant difference is that quarks also carry color charges (red/blue/green) and therefore participate in the strong interaction unlike leptons. All of the fundamental particles interact with each other via the exchange of gauge bosons (integer spin field particles).

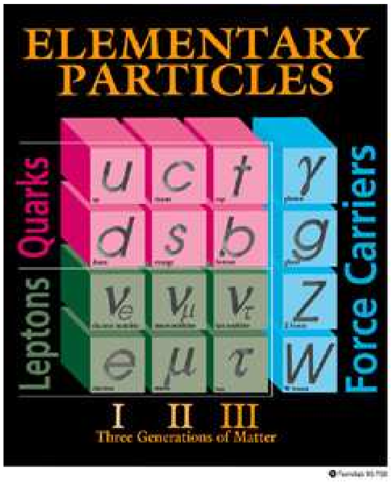

Figure 2.1: A summary of the fundamental fermions (leptons and quarks) which are the building blocks of particles, and of the gauge bosons which are the force carriers in the SM.

The three fundamental interactions form their own symmetry group: the one dimensional unitary group (U(1)) for the EM interaction, the 2-D special unitary group (SU(2)) for the weak interaction, and the 3-D special unitary group (SU(3)) for the strong interaction. The number of degrees of freedom in the n dimensional symmetry group is determined as $n^2 - 1$, which specifies the number of gauge bosons in each symmetry group. The photon (γ) mediates the EM interaction (i.e. n = 1), and two charged ($W^{\pm}$) and one neutral (Z^0) weak bosons mediate the weak interaction. The strong interaction is mediated by eight gauge fields, gluons (G^a_μ with a = 1,...,8). The gluons themselves also carry color charges and interact with each other in addition to their interactions with quarks. This structure results in the enriched dynamics of the strong interaction and is described by the theory of QCD.

The observable gauge bosons do not directly reveal the nature of the gauge field. In order to form the symmetry group of the weak interaction, a weak isotriplet of the weak currents (W_μ^i with i = 1, 2 for charged current, and i = 3 for neutral current) is constructed within the SU(2) structure. The weak interaction is known to couple only to left-handed fermions in the SM which explains the observation of parity violation in charged current reactions [9]. However, the weak neutral current is observed to also have a right-handed component. To preserve the SU(2) symmetry, the isosinglet EM current (B_μ) is included. The orthogonal combinations of weak neutral currents and the EM current satisfy SU(2) symmetry and agree with experimental observations. Thereby, the charged vector boson ($W^\pm$), the neutral vector boson (Z), and the photon (A) are described as:

$$W_\mu^\pm = \frac{1}{\sqrt{2}}(W_\mu^1 \mp iW_\mu^2), \tag{2.1}$$

$$A_\mu = B_\mu \cos\theta_W + W_\mu^3 \sin\theta_W \quad \text{(massless)}, \tag{2.2}$$

$$Z_\mu = -B_\mu \sin\theta_W + W_\mu^3 \cos\theta_W \quad \text{(massive)}, \tag{2.3}$$

where the W_μ^3 and B_μ are two neutral fields and θ_W is a weak mixing angle[1]. This is the mechanism by which the weak interaction is unified with the EM interaction (SU(2) × U(1)), and the unified interaction is called the *electroweak interaction*. Additional details can be found in reference [10].

The gauge bosons are required to be massless because a mass term violates the gauge invariance of the interaction; otherwise the gauge theory is mathematically inconsistent and the symmetry is broken. The massless photon and gluons satisfy this condition, but the weak vector bosons do not. The weak bosons are discovered to have masses of 80.4 GeV/c^2 for $W^\pm$ and 91.2 GeV/c^2 for Z^0. In order to keep the theory renormalizable and give masses to the weak gauge bosons naturally, a spontaneous electroweak symmetry breaking (EWSB) mechanism

---

[1] The mixing angle governs the relation between the EM coupling constant (g') and the weak coupling constant (g) as $g \sin\theta_W = g' \cos\theta_W = e$.

was proposed. Three independent papers describing the theoretical mechanism appeared in Volume 13 of Physical Review Letters in 1964 [2]. They were formulated by Gerald Guralnik, Carl Hagen, and Tom Kibble; by Peter Higgs; and by Francois Englert and Robert Brout. All three papers were written from different perspectives, and each made a distinct contribution. For short, EWSB is now commonly referred to as the Higgs mechanism.

2.2 The Higgs Mechanism

Here, we assume a complex scalar field ϕ and a massless vector field A^μ. The Lagrangian is assumed to be

$$\mathcal{L} = (D_\mu\phi)^*(D^\mu\phi) + \mu^2\phi^*\phi - \lambda(\phi^*\phi)^2 - \frac{1}{4}F^{\mu\nu}F_{\mu\nu}. \tag{2.4}$$

The parameters $\lambda > 0$ and $\mu^2 > 0$ are required for a bound potential. $F^{\mu\nu}$ is an antisymmetric tensor of the massless gauge boson field, $F^{\mu\nu} = \partial^\mu A^\nu - \partial^\nu A^\mu$. Under a local gauge transformation, the scalar and vector fields are transformed as:

$$\begin{aligned} &\phi \rightarrow \phi' = e^{ig\chi(x)}\phi \\ &A^\mu \rightarrow A'^\mu = A^\mu - \partial^\mu\chi(x), \end{aligned} \tag{2.5}$$

where the $D^\mu = \partial^\mu + igA^\mu$ in the Lagrangian, g is a coupling constant, and $\chi(x)$ is an arbitrary scalar function.

Focusing on the scalar field, the scalar potential has its minimum value at $\phi = \frac{v}{\sqrt{2}} = \sqrt{\frac{\mu^2}{2\lambda}}$. If we displace the potential around its minimum it can be rewritten as

$$\phi = \sqrt{\frac{1}{2}}[v + h(x)], \tag{2.6}$$

where $h(x)$ is a real field. Substituting these transformed fields (Eqn. 2.5 and 2.6) into the Eqn. 2.4, we have

$$\begin{aligned}\mathcal{L} &= \frac{1}{2}[(\partial_\mu - igA_\mu)(v+h(x))(\partial^\mu + igA^\mu)(v+h(x))] \\ &\quad +\frac{1}{2}\mu^2(v+h(x))^2 - \frac{1}{4}\lambda(v+h(x))^4 - \frac{1}{4}F^{\mu\nu}F_{\mu\nu}. \qquad (2.7)\end{aligned}$$

Expanding this Lagrangian, the mass terms are: $\frac{g^2v^2}{2}A_\mu A^\mu$ for the vector gauge boson and $-\lambda v^2h^2$ for the scalar boson. Other terms determine the production mechanisms and Higgs couplings to other particles. This implies that a complex scalar field and a massless vector field transform into a real scalar boson and a massive vector boson by a non-zero scalar potential at its minimum. This method of giving mass to the gauge boson is called the Higgs mechanism. EWSB is described its detail in references [11] and [12].

It is interesting that the complex scalar field actually turns into a real physical boson, h, the Higgs boson. The mass of the Higgs boson depends on λ and v. Here v can be determined from the masses of the gauge bosons. However, λ is completely unknown in the theory. Therefore the mass of the Higgs boson can only be determined experimentally.

It should be noted that the number of independent states remains the same before and after the gauge transformation. In this example, one complex scalar field ϕ has two real fields, and the massless vector boson has two polarization states. These states are reinterpreted as the physical scalar Higgs boson and three polarization states of a massive spin-1 boson. In both cases the total number of degrees of freedom (DOF) is four. This can be applied to more complicated cases. In the SU(2) theory, the three massless weak gauge bosons provide six independent states. Introducing a scalar complex Higgs doublet field (it already has four DOF), the total number of DOF would be ten. After the gauge transformation, we end up with three spin-1 gauge bosons and one remaining particle which is the real scalar Higgs boson. If we consider two scalar complex doublet fields, we have eight independent states, thus having fourteen DOF including six from the massless weak gauge bosons. This can be reinterpreted as nine independent states for three massive spin-1 bosons and five real scalar Higgs bosons.

The SM Higgs boson

As previously mentioned, for the local SU(2) gauge invariance, an SU(2) doublet of complex scalar fields is assumed to be

$$\phi = \begin{pmatrix} \phi_\alpha \\ \phi_\beta \end{pmatrix} = \sqrt{\frac{1}{2}} \begin{pmatrix} \phi_1 + i\phi_2 \\ \phi_3 + i\phi_4 \end{pmatrix}. \tag{2.8}$$

To make things simple, $\phi_1,\ \phi_2,\ \phi_4$ are chosen to be zero and $\phi_3^2 = \frac{\mu^2}{\lambda} \equiv v^2$. Substituting the scalar field

$$\phi = \sqrt{\frac{1}{2}} \begin{pmatrix} 0 \\ v + h(x) \end{pmatrix}$$

and isotriplet gauge bosons W_μ^a into Eqn. 2.4 in place of ϕ and A_μ, respectively, the Higgs boson mass (m_H) is determined as $\sqrt{\frac{\lambda}{2}}v$. Here λ is the Higgs self-coupling parameter, which is unknown, and v is the vacuum expectation value (VEV) of the Higgs field. The parameter v is determined to be 246 GeV (=$(\sqrt{2}G_F)^2$, where G_F is the Fermi coupling constant), which is derived from the observed W boson mass via the relation, $m_W = \frac{gv}{2}$. As mentioned earlier the Higgs boson mass (m_H) can only be determined experimentally.

A strong limit on m_H is obtained from direct searches at the four experiments at the large electron-positron (LEP) collider at CERN [13]. The combined data from the four LEP experiments yields a lower limit on m_H of 114.4 GeV/c^2 at 95% C.L. This limit is extracted within the framework of the Standard Model, and is therefore commonly referred to as the LEP limit on the mass of the SM Higgs boson. In addition, current Tevatron experiments (CDF and DØ) exclude a SM Higgs boson around $m_H \sim 170$ GeV/c^2 as summarized in reference [14].

The SM Higgs boson mass can also be deduced indirectly from a combination of all precision measurements of the SM parameters. The overall SM global fit yields a most probable value for m_H of 87^{+36}_{-27}GeV/c^2. If this result is combined with the direct limits from LEP we obtain an upper limit on m_H of 190 GeV/c^2 at 95% C.L. [15].

2.3 The Minimal Supersymmetric Extension of the SM

The SM uses a minimal Higgs structure by incorporating only one Higgs doublet. However, the SM Higgs boson has not been discovered to date. The Higgs sector can be formulated in several ways, and the next simplest way is to extend it with another Higgs doublet. With the extended Higgs framework we also employ a supersymmetry (SUSY) theory with parameters that remain in agreement with the SM values as currently measured in experiments. By introducing a symmetry between bosons and fermions, the theory of SUSY provides elegant solutions to some of the issues which are unresolved in the SM, including the hierarchy problem in the corrections to the particle masses and the absence of a dark matter candidate. In order to develop a theory beyond the SM, two major constraints must be satisfied: the first is that $\rho = \frac{m_W^2}{m_Z^2 \cos^2\theta_W}$ must be very close to 1; the second is that flavor changing neutral currents (FCNC) are very suppressed. Both of these constraints are strongly supported by experimental data.

Beyond the SM, many diverse hypotheses with extended Higgs sectors have been proposed to explain EWSB. The simplest extension is a two Higgs-doublet model (2HDM). The minimal supersymmetric standard model (MSSM) employs the type-II 2HDM, where at leading order one doublet couples to the up-type fermions and the other couples to the down-type fermions The two Higgs doublets result in two charged Higgs bosons ($H^{\pm}$) and three neutral Higgs bosons (h^0, H^0, A^0).

We now describe in more detail the minimal supersymmetric extension of the SM (MSSM) which incorporates the simplest Higgs extension with two Higgs doublets. Note that MSSM not only satisfies the two experimental constraints described above, but also provides a mechanism for EWSB. Here soft SUSY-breaking[2] in the Higgs potential results in spontaneous breaking of the SU(2) × U(1)

---

[2] The exact symmetry between bosons and fermions requires that superpartners have the same masses as the known particles. Since there have been no observation of any superpartners with exact masses of known particles, SUSY symmetry must be broken. However, the SUSY-breaking scale should not be too larger than 1 TeV in order to maintain naturalness of the theory.

gauge invariance [11] [16] [17] [18]. The MSSM introduces a minimal number of additional supersymmetric parameters into the theory. However, this minimal number is over one hundred, as compared to the only one unknown parameter (m_H) in the SM. The SUSY parameters generally require tuning and strongly depend on additional assumptions. However, among the parameters, only a few play an important role in SUSY phenomenology.

2.3.1 Higgs Bosons in MSSM

The MSSM framework includes two Higgs doublets with opposite hypercharges: Y = -1 doublet H_d and Y=+1 doublet H_u, thus having

$$H_d = \begin{pmatrix} H_d^1 \\ H_d^2 \end{pmatrix} = \begin{pmatrix} \Phi_1^{0*} \\ -\Phi_1^- \end{pmatrix}, \quad H_u = \begin{pmatrix} H_u^1 \\ H_u^2 \end{pmatrix} = \begin{pmatrix} \Phi_2^+ \\ \Phi_2^0 \end{pmatrix}. \tag{2.9}$$

The H_d exclusively couples to down-type fermions and the H_u couples to up-type fermions in order to satisfy the no FCNC constraint at tree-level. This is referred to as the Type-II two Higgs doublets model (2HDM) [11].

The Higgs potential is:

$$\begin{aligned} V &= (m_d^2 + |\mu|^2) H_d^{i*} H_d^i + (m_u^2 + |\mu|^2) H_u^{i*} H_u^i - m_{ud}^2 (\epsilon^{ij} H_d^i H_u^j + h.c) \\ &\quad + \frac{1}{8}(g^2 + g'^2)[H_d^{i*} H_d^i - H_u^{j*} H_u^j]^2 + \frac{1}{2} g^2 |H_d^{i*} H_u^i|^2, \end{aligned} \tag{2.10}$$

where μ is the supersymmetric Higgsino mass, m_d^2, m_u^2, m_{ud}^2 are soft-SUSY-breaking masses, and $\epsilon^{12} = \epsilon^{21} = 1$, $\epsilon^{11} = \epsilon^{22} = 0$. Minimizing this potential, the Higgs fields requires VEV to be :

$$\langle H_d \rangle = \sqrt{\frac{1}{2}} \begin{pmatrix} v_d \\ 0 \end{pmatrix}, \quad \langle H_u \rangle = \sqrt{\frac{1}{2}} \begin{pmatrix} 0 \\ v_u \end{pmatrix}, \tag{2.11}$$

where ${v_d}^2 + {v_u}^2 = v^2$. Here v is the same VEV (=246 GeV), which is determined by the m_W measurement. A key parameter of MSSM is the ratio of the two VEVs,

$$\tan\beta = \frac{v_u}{v_d}. \tag{2.12}$$

As briefly mentioned in the Sec. 2.2, the two Higgs doublets give rise to five scalar Higgs bosons: two neutral scalars h^0 and H^0, one pseudo-scalar A^0, and a pair of charged Higgs bosons $H^\pm$ (we use H^+ for both H^+ and H^-). The physical states of the Higgs bosons are described using the Higgs doublets :

$$\begin{aligned} H^\pm &= \Phi_2^\pm \cos\beta - \Phi_1^\pm \sin\beta, & (2.13)\\ A^0 &= \sqrt{2}(\mathrm{Im}\Phi_2^0 \cos\beta - \mathrm{Im}\Phi_1^0 \sin\beta), & (2.14)\\ h^0 &= -(\sqrt{2}\mathrm{Re}\Phi_1^0 - v_d)\sin\alpha + (\sqrt{2}\mathrm{Re}\Phi_2^0 - v_u)\cos\alpha, & (2.15)\\ H^0 &= (\sqrt{2}\mathrm{Re}\Phi_1^0 - v_d)\cos\alpha + (\sqrt{2}\mathrm{Re}\Phi_2^0 - v_u)\sin\alpha. & (2.16) \end{aligned}$$

In those equations, α is a CP-even Higgs mixing angle. The six most important parameters in MSSM are the four Higgs masses (m_{H^+}, m_{A^0}, m_{h^0}, and m_{H^0}, conventionally $m_{h^0} < m_{H^0}$), α, and $\tan\beta$. At tree-level, all the MSSM Higgs masses and couplings can be expressed in terms of only two parameters, usually $\tan\beta$ and m_{A^0}.

The Higgs bosons are closely connected with the weak vector bosons ($W^\pm$ and Z^0). At tree-level, the masses are expected to be:

$$m_{H^+}^2 = m_{A^0}^2 + m_W^2 \quad (2.17)$$

$$m_{H^0,h^0}^2 = \sqrt{\frac{1}{2}}\left[m_{A^0}^2 + m_{Z^0}^2 \pm \sqrt{(m_{A^0}^2 + m_{Z^0}^2)^2 - 4m_{Z^0}^2 m_{A^0}^2 \cos^2 2\beta}\right] \quad (2.18)$$

The diagonalization of the CP-even Higgs mass matrix comes with the equation,

$$m_{h^0} \leq m_{Z^0}|\cos 2\beta| \leq m_{Z^0}. \quad (2.19)$$

The lightest CP-even Higgs boson in MSSM is expected to behave like the SM Higgs boson. Therefore, if h^0 is lighter than the Z^0 boson, it should have been observed by LEP experiments (they exclude $m_H \leq 114$ GeV/c^2 at 95% C.L.). To solve this problem, a large radiative correction from the top quark loop in combination with a stop[3] loop is applied to the Higgs masses, as discussed in reference [19].

---

[3] Bosonic superpartner of the top quark.

It would be difficult to experimentally distinguish any one of these MSSM neutral Higgs bosons from the SM Higgs boson. However, the charged Higgs boson has no analogous particle in the SM. Therefore, the observation of charged Higgs boson would be evidence for new physics beyond the SM. As mentioned earlier in the introduction, the charged Higgs is closely tied to the top quark. For the case of $m_{H^+} > m_t + m_b$, the coupling $H^+ \to tb$ is expected to be predominant, and for $m_{H^+} < m_t - m_b$ the couplings $H^+ \to \tau\bar{\nu}$ and $H^+ \to c\bar{s}$ are dominant depending on the value of $\tan\beta$. The theoretical branching ratio $\mathcal{B}(t \to H^+ b)$ and the decay branching ratios of the H^+ in the context of MSSM are shown in Fig. 1.3. The tree-level couplings of these decay channels are:

$$\begin{aligned}
H^+\bar{t}b &: \frac{g}{\sqrt{2}M_W}(m_t \cot\beta + m_b \tan\beta), \\
H^+\tau\bar{\nu} &: \frac{g}{\sqrt{2}M_W} m_\tau \tan\beta, \\
H^+\bar{c}s &: \frac{g}{\sqrt{2}M_W}(m_t \cot\beta + m_s \tan\beta). \qquad (2.20)
\end{aligned}$$

2.4 Experimental Limits from Charged Higgs Searches

2.4.1 Direct Limits

Direct searches for a charged Higgs boson have been performed in high energy colliding beam experiments. The LEP experiments study electron-positron collisions at center of mass energies ranging from 189 GeV to 209 GeV. The four LEP experiments (ALEPH, DELPHI, L3, and OPAL) have searched for the direct production of SM Higgs boson as well as for the production of a charged Higgs boson beyond the SM. Direct searches at the Tevatron, which is a proton-antiproton collider operating at ×10 higher center of mass energy than the LEP collider, are much more difficult due to very large QCD backgrounds. Therefore, at the Tevatron, the charged Higgs has been searched in decays of top quarks, where the background levels are much smaller. However, this kind of search is only sensitive to a charged Higgs with a mass smaller than the mass of the top quark.

Search for H^+H^- at LEP

At LEP energies, charged Higgs bosons, which are predicted in the 2HDM and in the MSSM, are expected to be produced mainly through the process $e^+e^- \rightarrow H^+H^-$. In this search, each charged Higgs is assumed to decay only to $c\bar{s}$ and $\tau\bar{\nu_\tau}$, resulting in only three possible final states ($c\bar{s}c\bar{s}$, $c\bar{s}\tau\bar{\nu_\tau}$, $\tau\bar{\nu_\tau}\tau\bar{\nu_\tau}$) for the H^+H^- pair. The combined search result from the four LEP experiments is shown in Fig. 2.2 as a function of the branching ratio $\mathcal{B}(H^+ \rightarrow \tau^+\nu_\tau)$. The sensitivity in the hadronic channel (e.g. if $\mathcal{B}(H^+ \rightarrow \tau^+\nu_\tau) \sim 0$) is suppressed by the large $e^+e^- \rightarrow W^+W^-$ background if m_{H^+} is close to m_W. The sensitivity is regained at higher masses. The LEP Higgs Working Group quotes a lower limit on the charged Higgs mass as

$$m_{H^\pm} > 78.6 \text{ GeV}/c^2 \text{ at } 95\% \text{ C.L.} \tag{2.21}$$

Since the limit was obtained from direct H^+ reconstruction mass scan, it is valid regardless of the H^+ decay branching ratios [20] or of other SUSY parameters such as $\tan\beta$.

Search for Charged Higgs Boson production in association with a Top Quark at the Tevatron

At Tevatron energy ($\sqrt{s} = 1.96$ TeV), the production cross section of charged Higgs bosons is predicted to be a factor of 1000 smaller than the production cross section for $t\bar{t}$ pairs. The detection of a H^+ signal in the presence of a huge background from SM processes is extremely challenging. Therefore, experimental searches have focused on a different production mode, namely charged Higgs boson production in association with top quarks.

Previously a charged Higgs search was carried out using CDF II data with 193 pb^{-1} [21]. The analysis looked for a deficit or an excess of $t\bar{t}$ production in the final states of lepton+jets ($l\nu_l bbjj$), di-lepton ($ll\nu_l\nu_l bb$), lepton+τ_h ($l\tau_h\nu_l\nu_\tau bb$),

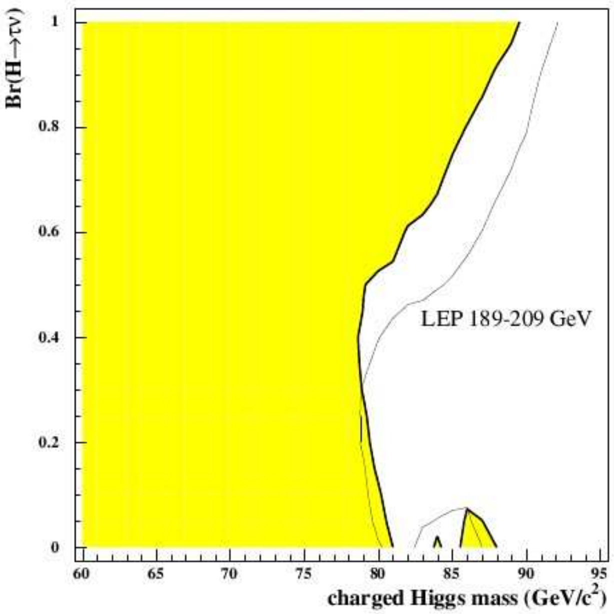

Figure 2.2: The LEP 95% C.L. bounds on m_{H^+} as a function of the branching ratio $\mathcal{B}(H^+ \rightarrow \tau^+\nu_\tau)$. This limit is determined from combining the data collected by the four LEP experiments at energies from 189 to 209 GeV. The expected exclusion limits for this level of integrated luminosity are shown by a thin solid line. The actual observed limits from the data are shown by a thick solid line. The shaded area is excluded at the 95% C.L.

assuming H^+ final states: $c\bar{s}$, $\tau^+\nu$, $t^*\bar{b}$, and W^+h^0. The top quark is assumed to decay into either Wb or H^+b. Considering the decay branching ratios of H^+ for each $\tan\beta$, an exclusion limit is placed in the MSSM parameter plane (m_{H^+}, $\tan\beta$) as shown in Fig. 2.3.

The DØ experiment reports on a search for $q\bar{q}' \rightarrow H^+ \rightarrow t\bar{b}$ in the 180 $\leq m_{H^+} \leq$ 300 GeV mass range using 0.9 fb^{-1} DØ data [22]. The analysis investigated the s-channel $W^+ \rightarrow t\bar{b}$ process. The observed limits on the production cross section times the branching fraction ($\sigma(q\bar{q}' \rightarrow H^+) \times \mathcal{B}(H^+ \rightarrow t\bar{b})$) range from 14 pb for m_{H^+} of 180 GeV/c^2 to 5 pb for m_{H^+} of 300 GeV/c^2. These limits are valid in the Type-I and Type-III 2HDMs depending on the width Γ_{H^+} of the charged Higgs boson. The exclusion limit in the (m_{H^+}, $\tan\beta$) is shown in Fig. 2.4.

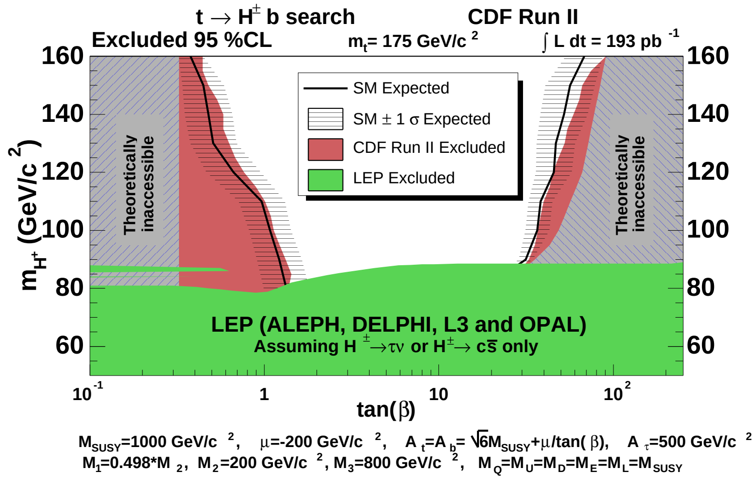

Figure 2.3: Combined LEP and CDF II experimental limits on MSSM in the $\tan\beta$ and m_{H^+} plane. Typical benchmark scenario developed for the search of h^0 at LEP experiments [7]. The value of A_t is computed as a function of $\tan\beta$, allowing for the maximum mass of the h^0 for each value of $\tan\beta$.

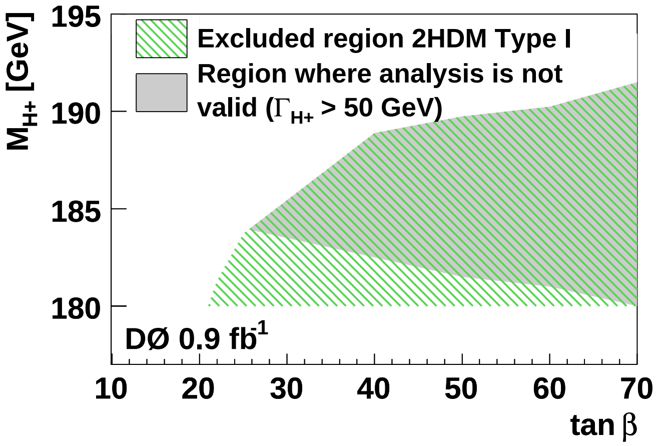

Figure 2.4: The DØ 95% C.L. excluded region in the m_{H^+} vs. $\tan\beta$ space for Type-I 2HDM. The region for which $\Gamma_{H^+} > 50$ GeV indicates the approximate area where the charged Higgs width is significantly larger than the detector resolution and hence the analysis is not valid.

2.4.2 Indirect Limits

The PEP-II (SLAC), the KEKB (KEK), and the CESR (Cornell) accelerators are electron-position colliders which produce a large number of $B\bar{B}$ pairs through the production of the $\Upsilon(4S)$ resonance. In particular, the first two are designed to generate asymmetric e^+e^- collisions. Exploiting the clean environment of e^+e^- collisions and the enormous statistical samples of $B\bar{B}$ events, the BaBar (SLAC), Belle (KEK), and CLEO (Cornell) experiments have performed precision studies of B-decays. These include the observation of CP violation and measurements of the branching ratios of rare B decays. These can also be used to constrain new physics beyond the SM.

$B^- \to \tau^- \bar{\nu}_\tau$ Decays at KEKB and PEP-II

In the SM the leptonic decay of the B meson is given by

$$\mathcal{B}(B^- \to l\bar{\nu}_l)_{\rm SM} = \frac{G_F^2 m_B m_l^2}{8\pi}(1 - \frac{m_l^2}{m_B^2})^2 f_B^2 |V_{ub}|^2 l_B, \qquad (2.22)$$

where G_F is the Fermi coupling constant, m_l and m_B are the masses of a lepton $(e/\mu/\tau)$ and B meson, respectively, f_B is the B meson decay constant, V_{ub} is a CKM matrix element [23], and τ_B is the B^- lifetime. Because of the mass term, $B^+ \to \tau^+\nu_\tau$ has the largest branching ratio other than $e^+\nu_e$, $\mu^+\nu_\mu$ decays. As described in the Fig. 2.5, the $B^+(u\bar{b})$ meson decays into $\tau^+\nu_\tau$ through the virtual charged weak boson (W^-). And the $B^+ \to \tau^+\nu$ decay mode can be enhanced by several times if there is a charged Higgs contribution beyond the SM, as given by

$$\mathcal{B}(B^+ \to \tau^+\nu) = \mathcal{B}(B^+ \to \tau^+\nu)_{\rm SM} \times (1 - \frac{m_B^2}{m_{H^+}^2}\tan^2\beta)^2. \qquad (2.23)$$

The Belle [24] and BaBar [25] collaboration have measured the branching ratio $\mathcal{B}(B \to \tau\nu)$ to be:

$$\begin{aligned} \mathcal{B}(B \to \tau\nu) &= (1.65^{+0.38}_{-0.37}(\text{stat})^{+0.35}_{-0.37}(\text{syst})) \times 10^{-4}\ (Belle) \text{ and} \\ \mathcal{B}(B \to \tau\nu) &= (1.20^{+0.4}_{-0.38}(\text{stat})^{+0.29}_{-0.30}(\text{syst})) \times 10^{-4}\ (BaBar), \qquad (2.24) \end{aligned}$$

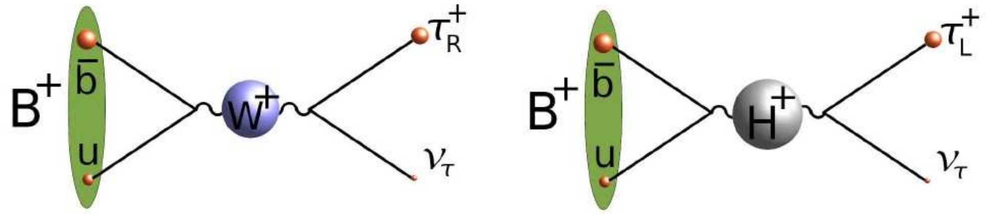

Figure 2.5: Feynman diagram describing the $B^+ \to \tau^+\nu_\tau$ decay in the SM (left), and with a charged Higgs contribution beyond the SM (right).

in samples of 657 $\times 10^6$ $B\bar{B}$ events and 383 $\times 10^6$ $B\bar{B}$ events, respectively. By comparing the measured values with the SM expectation of the leptonic branching ratio [26], $\mathcal{B}(B^- \to \tau\bar{\nu_\tau}) = (0.78^{+0.09}_{-0.13}) \times 10^{-4}$, they set constraints in the (m_{H^+}, $\tan\beta$) plane. Figure 2.6 shows the latest limits from the Belle experiment.

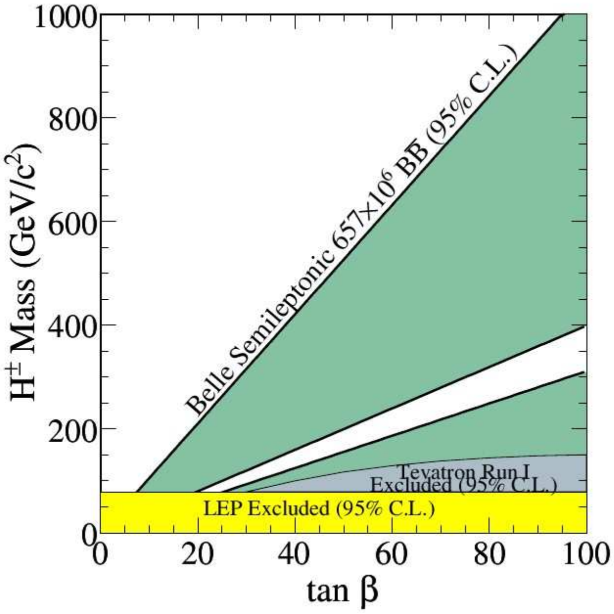

Figure 2.6: Constraints on the MSSM charged Higgs in the (m_{H^+}, $\tan\beta$) plane from B quark decays. The shaded area is the region excluded with 95% C.L.

FCNC: $b \rightarrow s\gamma$ study at CESR

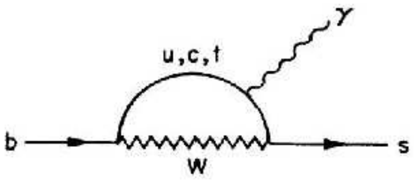

Figure 2.7: The $b \rightarrow s\gamma$ penguin diagram.

In the SM the flavor changing neutral current (FCNC) process in b decays, $b \rightarrow s\gamma$, can be described with a penguin diagram, in which a virtual W is exchanged in a loop with an up-type quark in conjunction with the emission of a photon, as shown in Fig. 2.7. This process is enhanced by the existence of a charged Higgs boson as predicted theoretically within Type-II 2HDM. The CLEO experiment has measured a branching ratio for the inclusive process $b \rightarrow s\gamma$ as $\mathcal{B}(b \rightarrow s\gamma) = (2.32 \pm 0.57(stat) \pm 0.35(syst)) \times 10^{-4}$ [27]. This results in a limit on the charged Higgs mass of

$$m_{H^+} > (244 + \frac{63}{\tan^{1.3}\beta})\mathrm{GeV}/c^2. \tag{2.25}$$

However, this limit is highly dependent on various SUSY parameters and corrections [28].

Chapter 3

The Tevatron

This chapter describes the Fermi National Accelerator Laboratory, the leading high energy experimental facility, and the accelerators and detectors used to produce and collect $p\bar{p}$ collisions for this analysis.

3.1 Overview of Fermilab

The Fermi National Accelerator Laboratory (Fermilab) is located 30 miles west of Chicago, Illinois. Fermilab, originally named the National Accelerator Laboratory, was proposed in 1952 by the Midwestern Universities Research Association as a large accelerator facility. It was commissioned by the U.S. Atomic Energy Commission, under a bill signed by President Lyndon B. Johnson on November 21, 1967. On May 11, 1974, the laboratory was renamed in honor of 1938 Nobel Prize winner Enrico Fermi, one of the preeminent physicists of the atomic age. Dr. Robert R. Wilson was selected as the first director of the new laboratory. Wilson directed the construction and commissioning of the new accelerator facility. The Universities Research Association (URA), a consortium including about 90 universities, has been providing the oversight Fermilab's operation since its completion [29] [30].

Fermilab experiments discovered the last two (and heaviest) fundamental quarks in the Standard Model. The bottom quark was discovered in June of 1977 [31], and the top quark was discovered in February of 1995 [32]. The first

Figure 3.1: Fermilab overview

direct evidence for the existence of the tau neutrino was found at Fermilab in July of 2000 [33]. In addition to the discovery of these three elementary particles, Fermilab experiments have confirmed many predictions of the Standard Model including the recent observation of single top quark production [34], the discovery of Σ_b baryons [35], and precision measurements of the mass and productions cross sections of the $W^{\pm}$ and Z^0 bosons.

Currently a variety of experimental physics programs are active at Fermilab. These include neutrino experiments (e.g. MiniBooNE, SciBooNE, MINOS, MINERνA, and NOνA), dark matter searches (e.g. CDMS, COUPP), Astrophysics experiments (e.g. Pierre Auger Observatory, Sloan Digital Sky Survey), and the two large Tevatron collider experiments, CDF and DZero (DØ) [36].

3.2 Accelerators

Fermilab is home to the world's most powerful particle accelerator, the Tevatron, which is four miles in circumference. The 1 TeV proton and antiproton beams cannot be produced with Tevatron alone but require additional subsystems consisting of the Pre-accelerator, the Linac, the Booster, and the Main Injector. The subsystems include the Recycler, Debuncher and Accumulator. The Booster is collectively known as the Proton Source, and the Debuncher and Accumulator are referred to as the Antiproton Source. A brief description of each subsystem follows below. An schematic overview of these subsystems is shown in Fig. 3.2 [37].

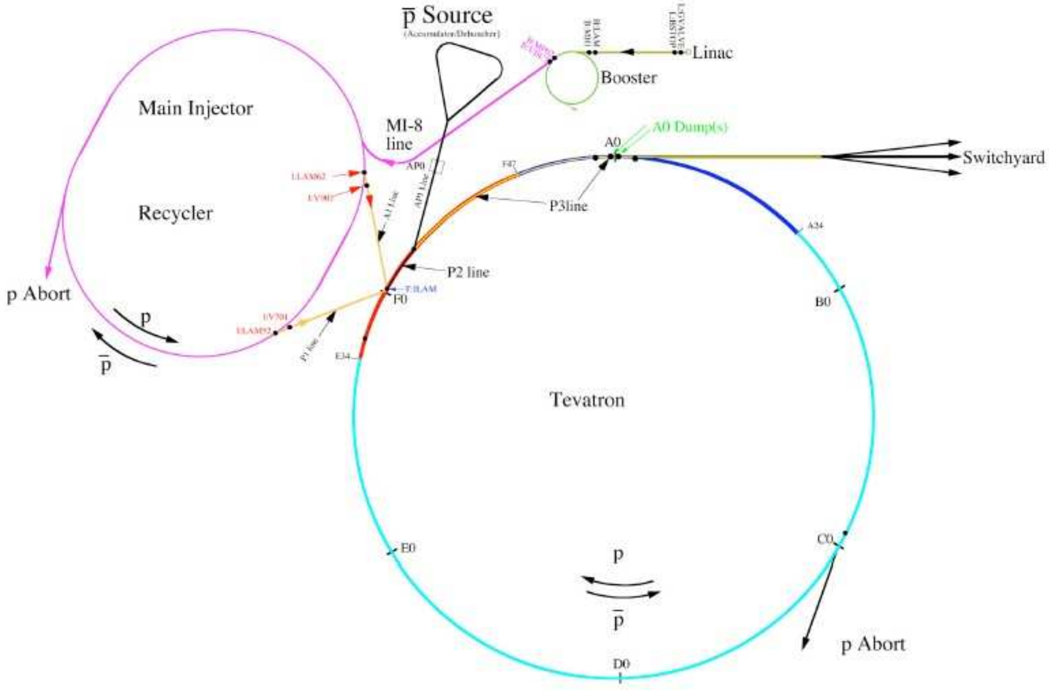

Figure 3.2: Overview of the Fermilab accelerator facility.

3.2.1 The Pre-accelerator

The process of particle acceleration begins with a small bottle of hydrogen located in the electrostatic Pre-accelerator (Preacc) system. Fermilab's Preacc is based on a Cockcroft-Walton generator [38]. Hydrogen atoms are first converted to negatively charged hydrogen ion (H^-) in the location of the dome of the Preacc. The dome is charged to an electric potential of -750 kV. Here H^- ions are allowed to accelerate (to an energy of 750 keV) by traversing a column leading from the negatively charged dome to the grounded wall. The Preacc accelerates bunches of ions every 66 ms (about 15 Hz). After the beam exits the accelerating column, it travels through a transfer line and enters the Linac. An overview of the Preacc is shown in Fig. 3.3 (a).

Figure 3.3: (a) An overview of the Pre-accelerator (Preacc) which is based on a Cockcroft-Walton generator design (left) and (b) Linac (right)

3.2.2 The Linac

The Linear Accelerator (Linac) [39], shown in Fig. 3.3 (b), guides the H^- ions with an energy of 750 keV, and accelerates them to 400 MeV. The Linac consists of two main sections, the low energy drift tube Linac (DTL) and the high energy side coupled cavity Linac (SCL). The DTL uses a tube amplifier to generate a radio frequency (RF) signal at 201 MHz for accelerating the H^- beam. The SCL uses Klystron amplifiers, which are capable of RF amplification at a rate which is four times faster than the tube amplifier. However, only every fourth cycle is used to accelerate beams in the SCL. The Linac accelerates the beam once every 66 ms (15 Hz) (at the same frequency as the Preacc). After the beam is accelerated in the Linac, the 400 MeV H^- ions are sent to one of two locations depending on the need (either to the Booster or to a beam dump when accelerator studies are performed).

3.2.3 The Booster

The Booster [40] is an intermediate accelerator that increase the beam energy from the Linac prior to injection into the Main Injector. The Booster is the first circular accelerator, or synchrotron, in the chain of accelerators as shown in Fig. 3.4 (a). It consists of a series of magnets arranged around a 75 m radius circle. Seventeen RF cavities are interspersed between the magnets. Once the 400 MeV H^- ions are injected into the Booster, the electrons are stripped off by passing through a thin layer of carbon. Then, the resulting beam of protons is accelerated to an energy of 8000 MeV (8 GeV). The 8 GeV proton beam can be directed towards two different locations depending on need (either to the Main Injector or to a beam dump). The MiniBooNE experiment (a Booster neutrino experiment) [41] uses 8 GeV protons from the Booster to produce a neutrino beam in the direction of the MiniBooNE detector. The proton beam is transferred to MiniBooNE through the same line that is used for the Main Injector, but is deflected towards to MiniBooNE beam line right before reaching the Main Injector.

Figure 3.4: (a) The Booster (left) and (b) The Main Injector (right)

3.2.4 The Main Injector

The Main Injector (MI) [42] is a circular synchrotron with seven times the circumference of the Booster. Its circumference is slightly more than a half of the circumference of the Tevatron. The MI plays a central role in linking various machines. The MI can accelerate (or decelerate) particles between an energy of 8 GeV and 150 GeV. The sources of the particles and their final destinations vary and depend on the "mode of operation", that is, what the MI is being used for at the moment. The Main Injector ring is shown in Fig. 3.4 (b).

The main functions of MI are listed below:

- Take a part of the 8 GeV proton beam from Booster, accelerate it to 150 GeV and coalesce the beam into a superbunch. The coalesced beam is injected into to the Tevatron. This process is repeated until there are 36 coalesced proton bunches in the Tevatron.

- The MI is used to accelerate a small part of the initial 8 GeV proton beam to 120 GeV. That beam is extracted and directed to the antiproton production target.

- The 8-GeV antiprotons are collected and circulated in the Antiproton Source (Sec. 3.2.5) and in the Recycler (Sec. 3.2.6). Then, they are sent back to the MI as a group of four pre-bunches. While accelerating to 150 GeV in the MI, the four pre-bunches of antiprotons are coalesced. When they reach an energy of 150 GeV, the antiprotons are directed into the Tevatron. In the Tevatron ring, the antiprotons travel in the counterclockwise direction which is opposite to the direction of the proton bunches. This processes is repeated until there are 36 coalesced antiproton bunches in the Tevatron.

- The MI accelerates part of the 8 GeV proton beam to 120 GeV for use by fixed target experiments. Currently there are no fixed target experiments in operation.

- The MI directs the 120 GeV proton beam to a target to produce neutrinos for neutrino experiments (NuMI [43]). These neutrinos are used for near detector experiments such as MINERνA and the MINOS near detector, and also travel through the earth and reach the Soudan underground mine in Minnesota, where the MINOS far neutrino oscillation detector is located. In the future, neutrinos which are off-axis from the direction of the beam will be used for the NOνA neutrino oscillations experiment (which is currently being prototyped).

3.2.5 The Antiproton Source

The Antiproton Source [44] consists of the Debuncher and the Accumulator. As mentioned in the previous section, antiprotons are generated by 120 GeV protons from the Main Injector which are incident on a nickel target. These collisions produce a spray of lower energy secondary particles including antiprotons. The antiprotons are extracted and filtered through a series of magnets and are directed into the Debuncher which is commonly referred to as the Pbar Source. It takes about 50,000 incident protons to produce one selected and filtered antiproton.

The Debuncher is a rounded triangular-shaped synchrotron. It has a mean radius of 90 m and is located in the outer side of tunnel as shown in Fig. 3.5. Its primary purpose is to efficiently capture a fraction of the wide momentum spread antiproton beam originating from the production target. There are also beam-cooling systems which are used to reduce the energy spread in the antiproton beam. The Debuncher does not accelerate the antiprotons, but maintains the beam at a constant energy of 8 GeV. The cooled antiproton beam is transferred to the Accumulator ring.

The Accumulator is the second synchrotron in the antiproton source. It is housed in the same tunnel as the Debuncher and has a radius of 75 m. It is used as a storage ring for the antiprotons. All of antiprotons are stored and cooled in the Accumulator at an energy of 8 GeV, and then sent to the Main Injector or Recycler.

3.2.6 The Recycler

The Recycler [45] is a permanent-magnet antiproton storage ring located 47 inches above the Main Injector in the same tunnel. Beams of 8 GeV antiprotons from

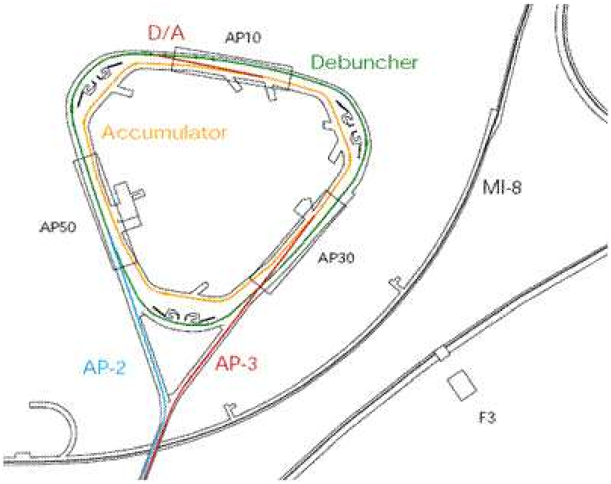

Figure 3.5: The Fermilab Debuncher ring (green, outer triangle) and Accumulator ring (yellow, inner triangle) of the Antiproton Source.

the Accumulator are directed into the Recycler and are stored for many hours. When the antiprotons are sufficiently cooled in the Recycler, the Recycler accepts more antiprotons from the Accumulator. This process is repeated and the Recycler keeps on stacking antiprotons until the Tevatron is ready for the collider operation. Through this process the Recycler is able to provide high intensity and low emittance antiprotons bunches to the Tevatron for use in the collider physics program.

3.2.7 The Tevatron Collider

The Tevatron [46] is the largest of the Fermilab accelerators. It is a circular synchrotron accelerator with a circumference of approximately 4 miles and includes eight accelerating RF cavities. It consists of a ring of superconducting magnets constructed with a niobium/titanium alloy superconducting cable. The superconductor needs to be kept at an extremely low temperature ($\sim$4 K). The need for a very low operating temperature is responsible for the Tevatron's extensive cryogenic "plumbing" and unique magnet protection systems.

The Tevatron ring is divided into six sectors labeled A through F as shown in Fig. 3.6. The A0 straight section is where the Tevatron tunnel connects to the

Switchyard and is also the location of one of the two beam abort systems for the Tevatron. The CDF collision hall is located in the B0 straight section, and the DØ collider experiment (named after the location it occupies in the tunnel) is located in the D0 straight section. At present, the C0 and E0 straight sections are not used. The F0 straight section is a crossroad of the laboratory. Here, the Tevatron RF cavities are located, as well as the connection points of both proton and antiproton transfer lines from Main Injector.

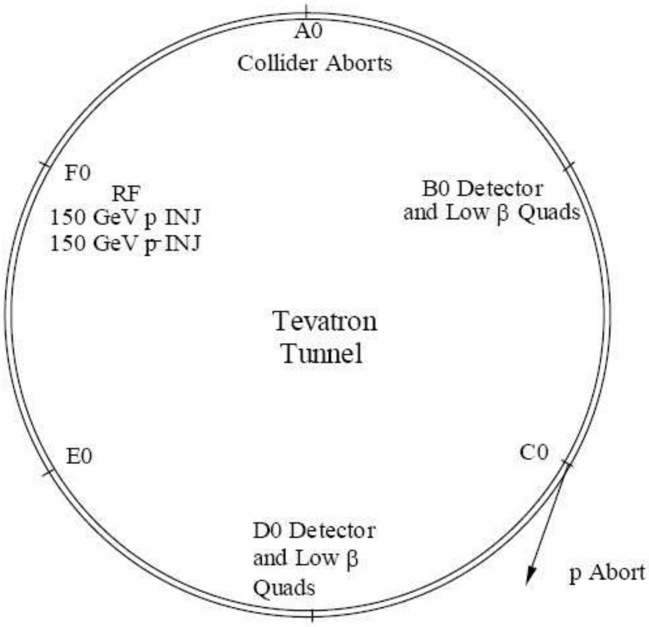

Figure 3.6: The Tevatron Tunnel

When the Fermilab accelerators are operating in the Collider mode, protons and antiprotons are injected into the Tevatron ring with initial energies of 150 GeV, and then accelerated to the final energies of 980 GeV. When the final energy is reached, the two counter-rotating particle beams pass through each other at two collision points, B0 and D0. These collisions continue on for hours unless some component failure causes the beam to be lost. This stable period of 980 GeV proton and antiproton collisions is called a store. When the number of collisions per second drops too low to be useful for experimenters, the store is ended, and the Tevatron prepares for a new store.

In the past, the Switchyard [47] was used to deliver the 800 GeV beam from the Tevatron to Fixed Target experiments in the Meson, Proton, and Neutrino areas (until 1999). Nowadays, no beam is directed to the Switchyard from Tevatron. Instead, a 120 GeV proton beam is delivered by Main Injector into the Meson area, which was part of the original Switchyard.

3.2.8 The Beam Structure

In the Run II collider period the Tevatron has been operated with 36 bunches of protons and 36 bunches of antiprotons as configured in Fig. 3.7 [48]. Each proton (antiproton) bunch carries roughly 9×10^{12} (2×10^{12}) protons (antiprotons). The 36 bunches are distributed in three trains of 12 bunches. The bunches in a train are separated by 396 ns, and the trains are separated by a 2617 ns gap, called the abort gap. A complete revolution in the Tevatron takes 21 μs.

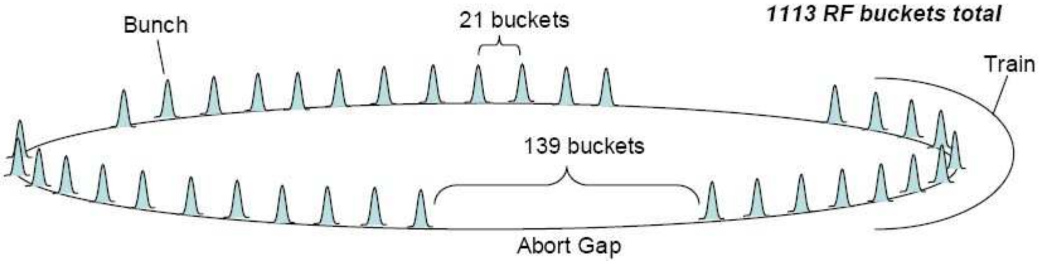

Figure 3.7: The proton and antiproton (36 × 36) bunches in three trains.

To avoid an inefficiency from unwanted collisions far from a detector, electrostatic separators are used to create non-intersecting helical closed orbits. First protons are injected into one strand, then antiprotons are injected in the other strand of the helix. Once both beams are injected into the Tevatron, the particles are accelerated to a final energy of 980 GeV. In order for collisions to occur, the polarity of the beam separators near the interactions points is reversed. The beams are made to collide at B0 and D0 for the CDF and DØ collider experiments, respectively. The detector used in this analysis is the Collider Detector at Fermilab (CDF) which is located at B0.

3.3 Collider Detector at Fermilab

The Collider Detector at Fermilab (CDF) is a general purpose solenoidal detector to study $p\bar{p}$ collisions at the Tevatron. In 1995 CDF started collecting data with $p\bar{p}$ collisions at the center of mass energy ($\sqrt{s}$) of 1.8 TeV. The CDF detector has since been upgraded for use at higher luminosity. In Run II the Tevatron has been operating at higher energy ($\sqrt{s} = 1.96$ TeV). The CDF detector for Run II (CDF II) has been taking data since 2001 [49]. The CDF II detector [50] is a cylindrical, forward-backward symmetric apparatus as shown in Fig. 3.8.

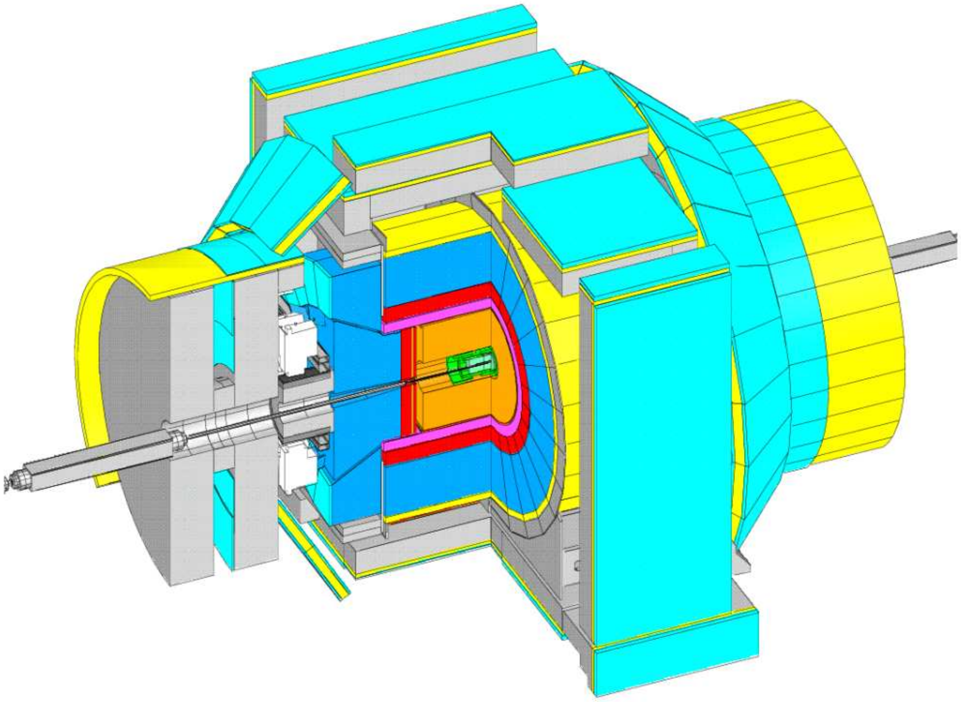

Figure 3.8: The CDF II detector includes silicon vertex detectors (green) and a central outer tracker tracking system (orange) located inside a magnetic field generated by a solenoid (magenta) magnet. Also shown are the calorimeters for detection of electromagnetic (red) and hadronic (blue) particles, and the muon detectors (cyan) which are located on the outside.

We begin with an overview of the CDF II coordinate systems and descriptions of the detector hardware (Section 3.3.1). The main subsystems of the CDF II detector are organized in three categories: the precision charged particle tracking systems (Sec. 3.3.2), the fast projective calorimeters (Sec. 3.3.3), and the muon detectors (Sec. 3.3.4). The luminosity monitoring system is described in Sec. 3.3.5. The time of flight counters and the forward detectors are briefly described in Sec. 3.3.6 and in Sec. 3.3.7, respectively. The trigger and data acquisition system are described in Sec. 3.3.8.

3.3.1 Overview of Coordinate Systems and Coordinate Variables

The CDF II detector uses a cylindrical coordinate system where the origin of the coordinate system is at the geometrical center of the detector and the positive z-axis is oriented along the direction of the proton beam; θ is the polar angle with respect to the proton beam and ϕ is the azimuthal angle. The direction of a particle in the detector is expressed in terms of the pseudorapidity (η) which is defined as $\eta = -\ln\tan(\frac{\theta}{2})$.

In the relativistic limit and for massless particles, the variable η is equal to the rapidity of the particle $y = \frac{1}{2}\ln(\frac{E+p_z}{E-p_z})$, where p_z is the momentum along the beam axis. When a proton collides with an antiproton in the B0 interaction point, an imbalance in the longitudinal momentum results in boosting the final state particles in the direction of the z-axis. However, the rapidity y transforms linearly with respect to a boost in the z direction, and Δy is invariant under such a boost. For this reason, some of the CDF II detectors are segmented into regions of constant Δy as shown in Fig. 3.9. In addition, most of the components of the CDF II detector are segmented into 15° wedges in ϕ.

3.3.2 Tracking and Vertexing Systems

Charged particles bend in the presence of a magnetic field. Therefore, a measurement of the curvature of the track yields the momentum of the particle and its

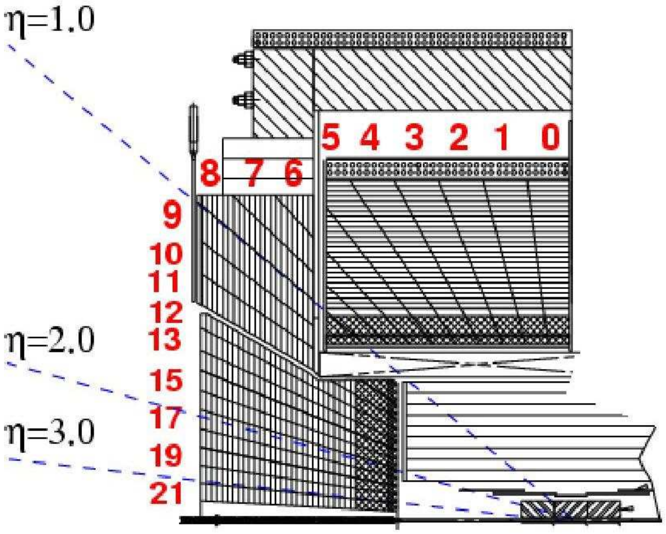

Figure 3.9: Side view of the CDF II segmented calorimeters showing the detector segmentation versus η in the y-z plane.

electric charge. Tracks for particles with low velocity or high mass have a larger curvature. The process of reconstructing the particle trajectory in a magnetic field is referred to as *tracking*, and the process of tracing to the production vertex of the particles is referred to as *vertexing*. At CDF II, the tracking and vertexing systems are located inside the magnetic field of a superconducting solenoid as shown in Fig. 3.10. This section describes the integrated tracking system of CDF II which consists of the Solenoid magnet, the Silicon Vertex Detectors (L00, SVX II, ISL) and the Central Outer Tracker (COT).

The Solenoid Magnet

The superconducting solenoidal coil is 4.8 m long and has a radius of 1.5 m radius. It is constructed from an aluminum-stabilized NbTi conductor. Charged particles are bent by the (very homogeneous) axial magnetic field which points along the -z direction. Under normal operation the magnet is operated with a current of 4650 A yielding a magnetic field of 1.4 T. The solenoid is contained within a cryostat which is cooled with liquid helium.

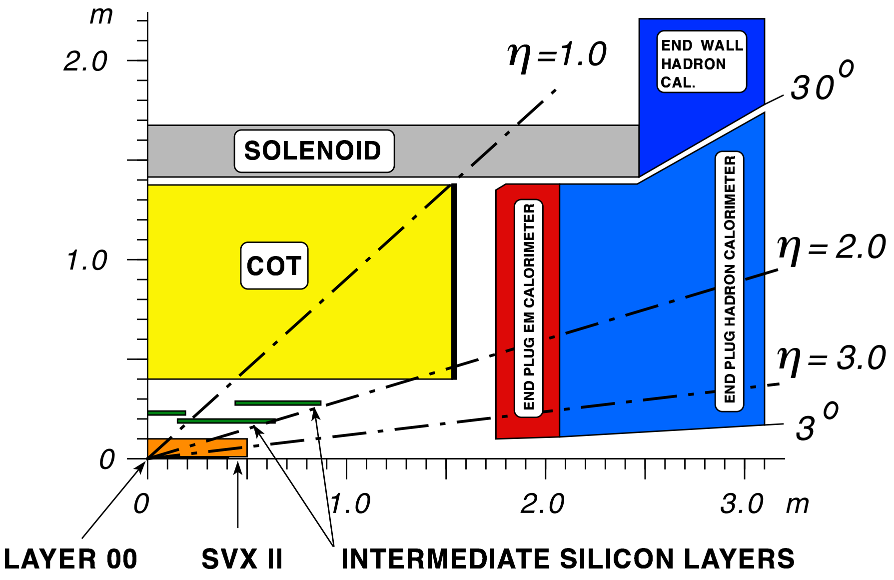

Figure 3.10: Side view of the CDF II tracking System.

The Silicon Vertex Detectors

The silicon vertex system consists of eight layers of silicon micro-strip detectors. The layer closest to the beam pipe is a radiation-hard, single sided silicon micro-strip detector (called L00), which employs an LHC sensor design allowing for high-bias voltage [51]. The next five layers comprise the SVX II system [52], and the two outer layers comprise the ISL system [53]. Both the SVX II and ISL layers are radiation-hard double sided silicon detectors. The silicon detectors in conjunction with the COT are used to measure the position of vertices with much improved resolution than from the COT alone.

Layer 00 (L00) is supported by a carbon-fiber structure. It consists of twelve ladders, six of which are located at a radius of 1.35 cm and the other six at a radius of 1.62 cm, as shown in Fig. 3.11. Each ladder is constructed from six sets of two wire-bonded modules which cover the full detector region in η (up to ~ 4). Layer L00 is used for improving the precision in the measurement of the track and for improving tagging efficiency for bottom quarks. It also compensates for the loss of efficiency from radiation damage to the innermost layer of SVX II.

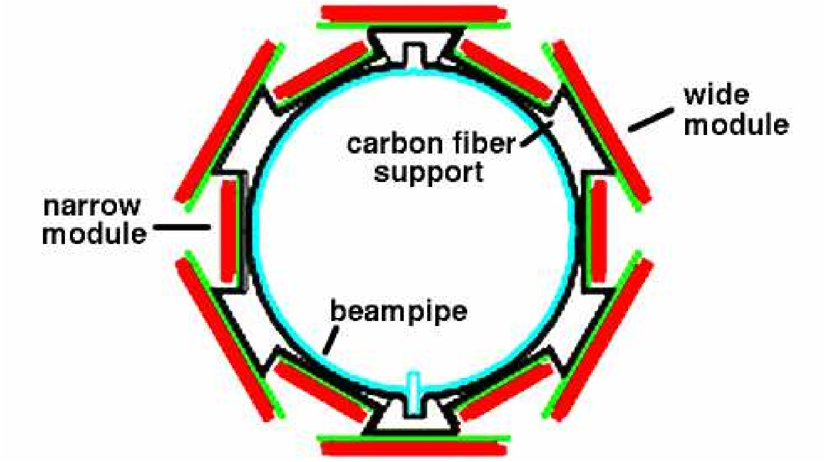

Figure 3.11: End view of the L00 silicon detector.

The New Silicon Vertex Detector (SVX II) was designed and constructed for the Run II collider program. It consists of five layers of silicon micro-strip detectors between an inner radius of 2.1 cm and an outer radius of 17.3 cm. The SVX II is constructed from three barrels positioned along the beam-pipe and covers η up to ± 2.0. All together the barrels extend to ± 45 cm along the z direction, covering 2.5 standard deviations (σ) of the luminous region in z. Each barrel supports five layers of double sided silicon microstrip detectors as shown in Fig. 3.12. The double sided design provides information on $\rho - \phi$ and z positions of hits. Layers 0, 1, and 3 are constructed with axial detectors on one side and 90° stereo detectors on the other side. Layers 2 and 4 combine axial detectors on one side and small angle (1.2°) stereo detectors on the other side. The z position information extracted from the stereo micro-strip detectors allows for the reconstruction of a three dimensional (3D) helix track for a charged particle. The single hit position resolution of SVX II is about 12 μm.

The silicon modules are supported by low mass substrates in assemblies called “ladders”. A layer consists of twelve ladders of approximately equal width. The 60 ladders in each barrel are mounted between two precision-machined beryllium bulkheads, which also carry the water cooling channels for the readout electronics. The large number of channels require that much of the electronics be mounted close to the modules. This yields a better signal-to-noise ratio for hit signals, but also results in additional multiple scattering due to the extra material in the tracking volume.

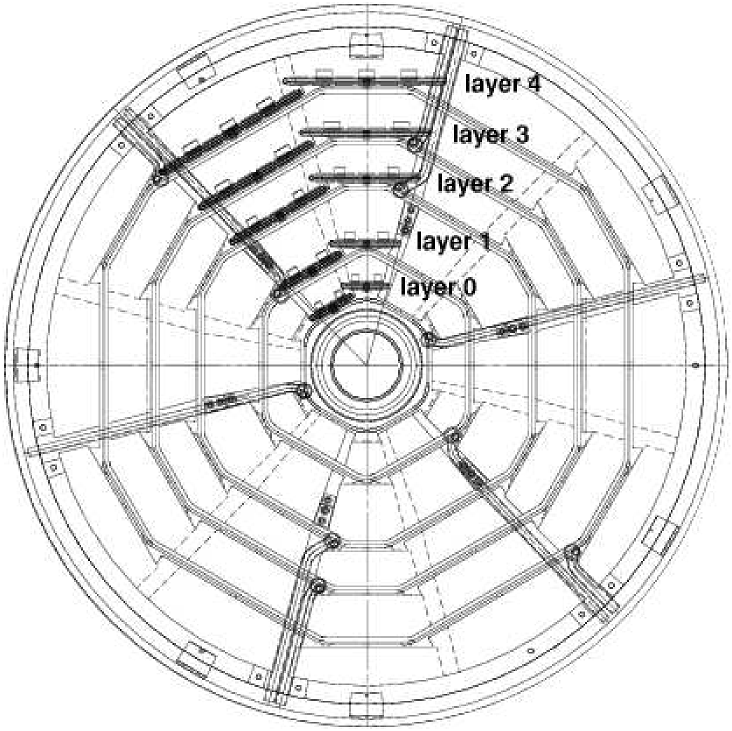

Figure 3.12: End view of the SVX II silicon bulkhead. The placement of ladders is shown for two adjacent wedges.

The Intermediate Silicon Layer (ISL) consists of a central layer at a radius of 22 cm and forward/backward layers at a radii of 20 cm and 28 cm as shown in Fig. 3.13. The central layer covers $|\eta| < 1.0$ and the forward/backward layers cover $1.0 < |\eta| < 2.0$ (where the efficiency of the COT falls off). The ISL helps link of tracks between the SVX II and COT in the central region. It also improves the silicon only tracking capabilities in the high η region. The layers are double sided with axial detectors on one side and small angle stereo modules on the other side. The ISL single hit resolution is about 20 μm.

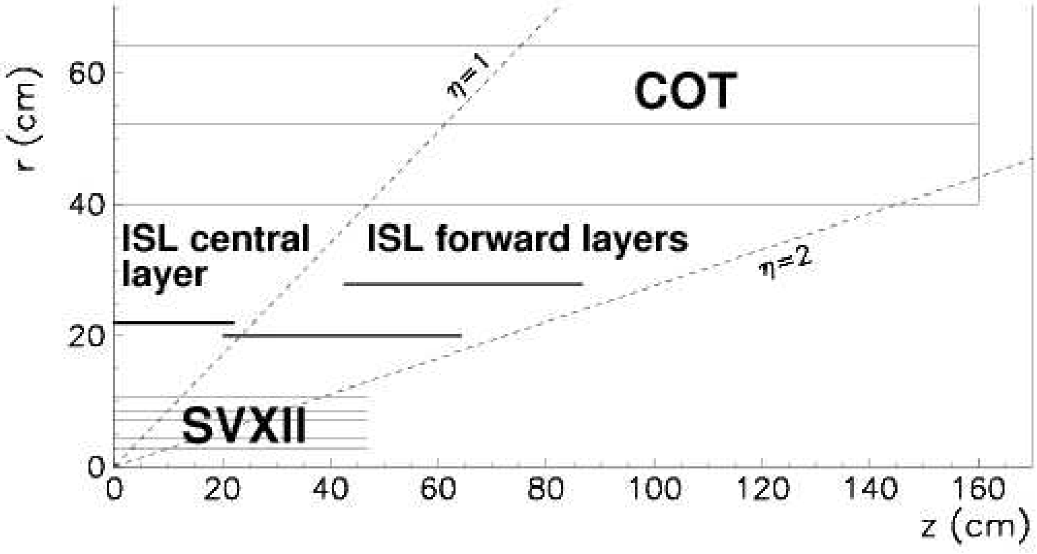

Figure 3.13: Location of the ISL.

The silicon detectors require low temperature cooling of the sensors and readout electronics. The cooling also reduces radiation damage. Temperature control is provided by a water/ethylene glycol coolant mixture flowing in aluminum tubes attached to the beryllium ledges mounted on the frame as shown in Fig. 3.14. The coolant flows within internal channels that are machined into the beryllium bulkheads at each SVX II barrel end. Under normal operation, the SVX II is cooled to -10° C, and the L00 and the ISL are cooled to 6° C.

The Central Outer Tracker (COT)

Charged particle tracking is done with a large open cell, cylindrical drift chamber [54]. The COT is located inside the solenoid in the region $|z| < 155$ cm (corresponding to $|\eta| < 1$). Its inner and outer radii are 40 and 137 cm, respectively. The COT consists of eight superlayers, each of which is constructed from a large number of cells as shown in Fig. 3.15. The odd numbered COT superlayers are "stereo" cells, and the even numbered superlayers are "axial" cells, which are positioned parallel to the z direction. The stereo cells with a small stereo angle ($\sim 2^\circ$) are used to obtain the z position of track segments.

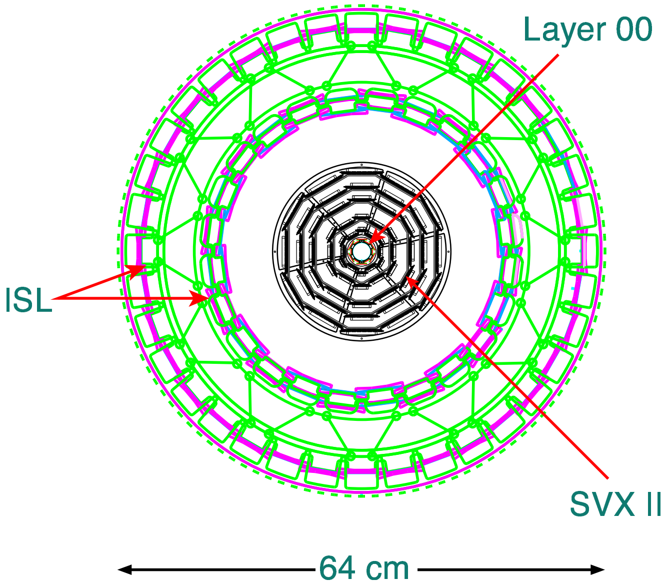

Figure 3.14: End view of the CDF II silicon system including the SVX II cooling bulkheads and ISL support structure.

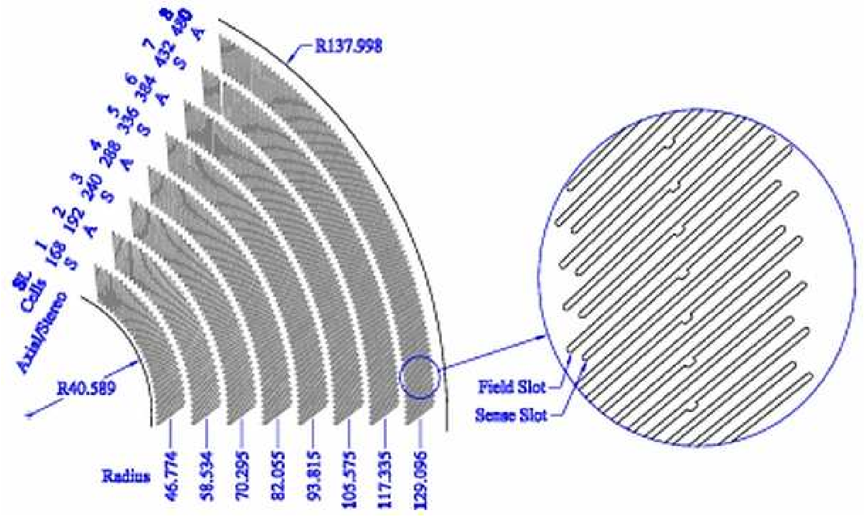

Figure 3.15: Schematic diagram of the eight superlayers in a quadrant of the COT. The number of cells, the radius from the center to the beam pipe, and the type (**S**tereo or **A**xial) are shown for each superlayer.

Each COT cell has an approximate size of 2 cm by 10 cm and a length of 310 cm spanning the whole longitudinal direction of the COT. A cell includes a longitudinal wire plane which contains twelve sense wires, thirteen potential (field) wires, and two additional shaper wires at either end. Wire planes are separated by cathode planes made of gold plated mylar (field sheet) as shown in Fig. 3.16. The wires and cathode planes are strung between two milled end plates.

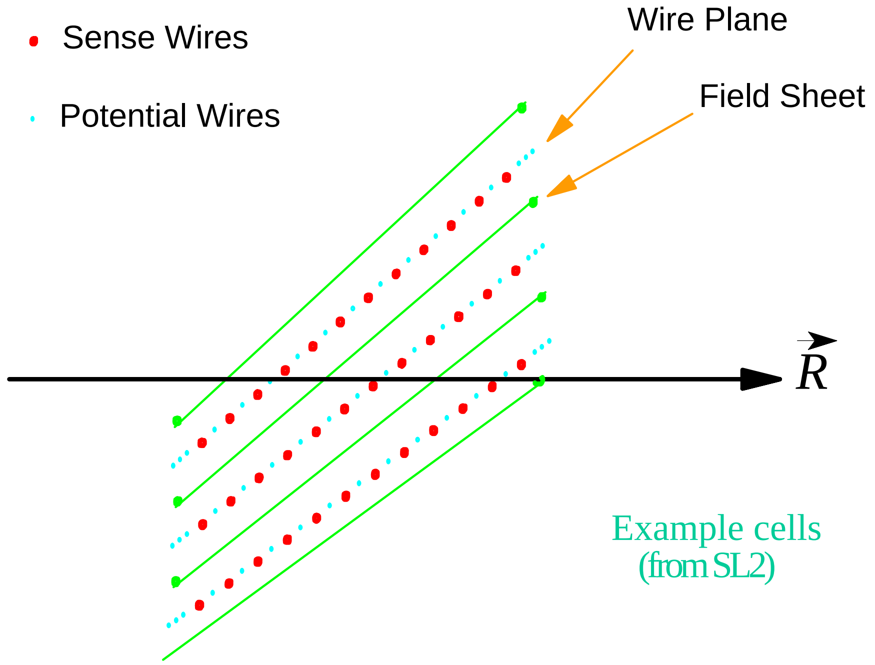

Figure 3.16: Schematic diagram of three COT cells in the Superlayer 2.

The drift chamber is filled with 50:50 mixture of Argonne-Ethane gas which serves as the active medium. The open cell configuration means that all the cells share the active gas in the COT volume. Inside each cell, potential wires shape the electric field with a larger negative voltage than the sense wires. When a charged particle passes through the gas, it leaves a trail of ionized electrons and positive ions. Negatively charged electrons drift towards the nearest positively charged sense wire, and positive ions drift to the negative potential wires. The charge pulse collected from a sense wire is referred to as a “hit”. Hits from different superlayers are used to infer the particle's trajectory. The single hit resolution of the COT has been measured to be 140 μm, resulting in a measurement of a particle's transverse momentum with a resolution of $\frac{\Delta p_T}{p_T} = 0.15\% \frac{p_T}{[\mathrm{GeV}/c]}$.

3.3.3 Calorimetry

The CDF II calorimetry system surrounds the tracking volume and the solenoid. The calorimetry system is composed of three subsystems: "Central", "Wall", and "Plug" calorimeters as shown in Fig. 3.17. The calorimeters provide energy measurement of particles for $|\eta| \leq 3.6$.

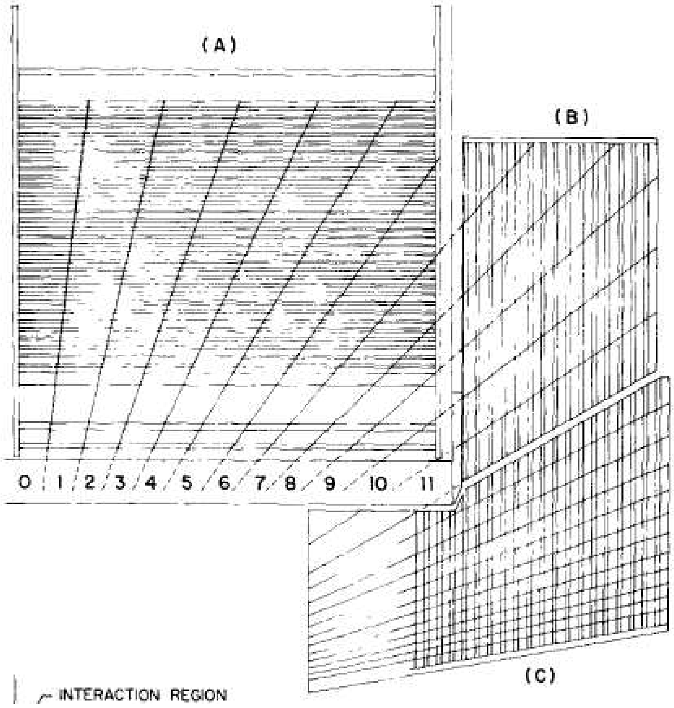

Figure 3.17: Elevation view of the CDF II Calorimeters: (A) Central, (B) Wall, and (C) Plug calorimeter.

The CDF II calorimeters are sampling calorimeters. Each calorimeter module is composed of an electromagnetic section followed by a hadronic section. The calorimeter modules are constructed from stacks of many layers. Each layer consists of an active scintillator and passive absorber material. As particles pass through the calorimeters, they interact with the material and develop characteristic "showers". Whereas electrons and photons shower quickly and deposit most of their energy in the electromagnetic section, hadrons (e.g. mesons, protons and neutrons) deposit most of their energy in the hadronic part. The scintillators sample the energy in the showers. The energy of electrons and photons is absorbed by the high Z material (lead) in the electromagnetic calorimeter. Most of the energy from hadrons is deposited in the iron plates of the hadronic calorimeters. Additional details are listed in Table. 3.1[1]. The mechanical and geometrical design parameters of the CDF II calorimeters are described below.

Sub Detector	CEM	CHA	WHA	PEM	PHA
Coverage	$\|\eta\| < 1.1$	$\|\eta\| < 0.9$	$0.7< \|\eta\| <1.3$	$1.1< \|\eta\| < 3.6$	$1.2< \|\eta\| <3.6$
Layers	31	32	15	23	23
Towers in η	10	8	6	12	11
Wedges in ϕ	24	24	24	24/48	24/48
Absorber	Lead	Iron	Iron	Lead	Iron
Depth	$18\chi_0$	$4.7\Lambda_0$	$4.5\Lambda_0$	$21\chi_0$	$7\Lambda_0$
Resolution	$1.7\% + \frac{13.5\%}{\sqrt{E}}$	$\frac{80\%}{\sqrt{E}}$	$\frac{80\%}{\sqrt{E}}$	$1\% + \frac{16\%}{\sqrt{E}}$	$4\% + \frac{74\%}{\sqrt{E}}$

Table 3.1: Parameters of the CDF II calorimeters.

The Central Calorimeters

The two halves of the central calorimeter are cylindrical and surround the Solenoid around the z axis. One half is placed on the east (plus η) side and the other half is placed on the west side (minus η). The two halves are joined at $z = 0$, each covering up to $\eta = \pm 1.1$. Each half is segmented into twenty-four ϕ wedges. The typical geometry of a wedge is shown in Fig. 3.18. The length of a wedge along the z direction is 249 cm. It spans radially from an inner radius of 172 cm to an outer

---

[1] High-energy electrons predominantly lose energy in matter by Bremsstrahlung, and high-energy photons by e^+e^- pair production. The characteristic amount of matter traversed for these related interactions is called the radiation length χ_0. For a high energy electron it is the mean distance over which the electron energy is reduced by a factor $1/e$ (or 0.368) by Bremsstrahlung. For a high energy photon χ_0 is equal to 7/9 of the mean free path for the pair production process. Therefore, χ_0 is the appropriate scale length for describing high-energy electromagnetic cascades. The absorption length (Λ_0) is the mean distance traveled by a hadron before it undergoes an inelastic interaction in the material.

radius of 345 cm. Each wedge is divided into ten towers with constant $\Delta\eta$ coverage, thus having different sizes in Δz as shown in Fig. 3.17. In each wedge the inner 35 cm comprise the Central Electromagnetic Calorimeter (CEM) [55], and the remaining outer part comprise the Central Hadron Calorimeter (CHA) [56].

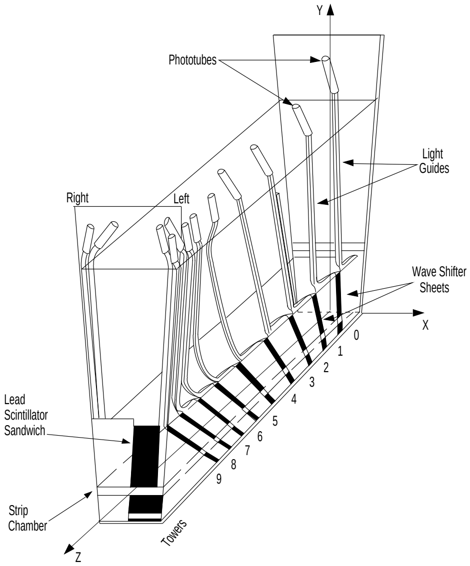

Figure 3.18: A schematic diagram of one central wedge.

The thirty one layers in the CEM add up to a total of 18 χ_0 (radiation length). Each CEM layer consists of 3.175 mm of lead as the passive absorber followed by 5 mm of polystyrene scintillator (SCSN-38) as the active medium. Panels constructed from green wavelength shifting Polymethylmethacrylate doped with Y7 dye (Y7 PMMA) are located at both ends of the scintillators to measure the sampled energy of particles by collecting and absorbing the blue light produced in the scintillator and shifting it to green light. The panels guide the green light along the edge of each tower on to photomultiplier tubes (PMT). This is done at both ends of each tower. The CEM energy resolution ($\frac{\sigma(E)}{E}$) is measured to be $1.7\% + \frac{13.5\%}{\sqrt{E}}$.

The capabilities of the CEM are enhanced by implementation of two extra detection systems: The Central Pre-Radiate chamber (CPR) and the Central EM ShowerMax Chamber (CES). The CPR is a set of proportional chambers placed between the CEM and the magnet coil. It is designed to improve the discrimination between electrons, photons and pions by identifying energy at the very beginning of the shower. The CES is located at the expected location of the maximum of the electromagnetic shower ($\approx 6\chi_0$). It is constructed with wires running along the z direction and perpendicular cathode strips. The CES measures the position of the centroid of the electromagnetic shower with high-precision (which is used to match and link electromagnetic showers and COT tracks. In addition, the CES measures the transverse shower profile which is used for improved identification of electrons, pions and photons.

The CHA is constructed from thirty-two layers with a total absorption length of $4.7\Lambda_0$. Each layer consists of a 2.54 cm thick iron plate followed by a 1 cm thick scintillator active sampling plane. The deposited energy produces blue light in the scintillator which is collected with light guides to photomultiplier tubes. Two PMTs collect the information for each CHA tower. The energy resolution of the CHA is measured to be $\frac{\sigma(E)}{E} = \frac{80\%}{\sqrt{E}}$. Unlike the CEM, the CHA segmentation is only eight towers (due to space limitation at large radius). The coverage for hadrons is completed by the End Wall Hadronic Calorimeter.

Endwall Hadronic Calorimeter

The Endwall Hadronic Calorimeter (WHA) extends the CHA coverage to $0.7 < |\eta| < 1.3$. It is located along the endwall, outside of the plug, and continues the tower structure of the CHA with reduced sampling (5 cm iron and 1 cm scintillator). It is organized into twenty four wedges in ϕ and six tower groups in η on each side. Each tower is read out by two PMTs. The details of the WHA geometry and physical characteristics are different from the CHA. The WHA towers are made of fifteen layers that are perpendicular to the beamline as shown in Fig. 3.17.

End Plug Calorimeters

The End Plug Calorimeters surround the beam pipe and are located at $|z| = 172$ cm from the interaction point as shown in Fig. 3.19. These calorimeters cover the region $1.1 \leq |\eta| \leq 3.6$. As is the case for the central calorimeters, the Plug

Calorimetry system consists of the Plug Electromagnetic Calorimeter (PEM) [57] followed by the Plug Hadronic Calorimeter (PHA). The electromagnetic part is segmented into twelve sections in η and the hadronic part is segmented into eleven section in η. The innermost (closest to the beamline) four η sections are segmented into twenty-four 15° wedges in ϕ. The remaining η sections are segmented into forty-eight 7.5° wedges in ϕ. The PEM is constructed from stacked layers, and each layer consists of 4.5 mm lead absorber followed by 4 mm of active scintillator. The PHA is constructed from stacked layers of 5.08 cm iron plate followed by 6 mm of active scintillator.

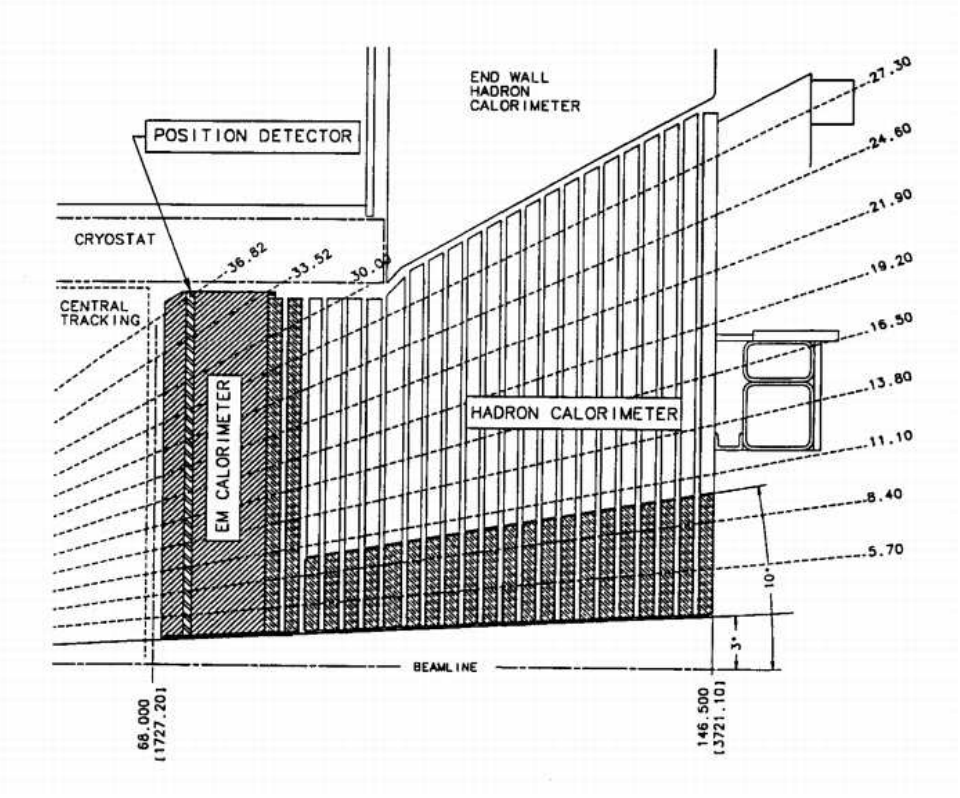

Figure 3.19: The End Plug Calorimeters (PEM, PHA). This figure shows the tower segmentation and the locations of the electromagnetic and hadronic calorimeters, and shower maximum detector.

The PEM is also implemented with a Plug Electromagnetic ShowerMax detector (PES) which is located at $\approx 6\chi_0$. The PES is constructed from two layers of 3.175 mm thick scintillator strips which are oriented at 45° to each other. The PES provides precision measurements of the position of electromagnetic showers and the transverse profile of the showers, which improves the identification of electrons, pions and photons. The first plane of scintillators in the PEM is constructed of thicker (10 mm rather than 4 mm) BC408 scintillator. BC408 yields 1.6 times more light than the polystyrene based SCSN38 scintillator which is used for all the other layers. This first scintillator is used as a Plug Pre-Radiate detector (PPR). As is the case for the CPR, the PPR is used to improve the identification of electrons, photons and pions. The plug calorimeters employ tile-fiber readout (the scintillators in the plug calorimeters are read out via green wavelength shifting optical fibers).

3.3.4 The Muon Identification System

The outermost detector in CDF II is the muon system [58]. A muon rarely interacts with matter due to the $\frac{1}{M^2}$ suppression of the electromagnetic Bremsstrahlung process. It passes through all the detector materials with high efficiency as it is a relativistically long-lived charged lepton. A high p_T muon generally leaves a track in the tracking volume but deposits only a small amount of energy in the calorimeters. Therefore, the muon detectors are located as the last detectors, detecting charged tracks behind the hadron calorimeters.

The CDF muon system consists of a large amount of absorber material followed by a few layers of drift chambers and scintillators. The drift chambers reconstruct the muon track position. The scintillation counters measure the time of flight of a muon. The muon crossing time is used in the trigger system.

A signal in the muon chambers may not be associated with a real muons from a proton-antiproton collision. There are a number of processes that can fake a muon signal. These include hadrons which are not fully absorbed by the calorimeter and steel absorbers (punch-through). The muon may originate from non-prompt background (i.e. result from the decays of long-lived hadrons such as pions, kaons and hyperons). The muon could originate from cosmic rays or from beam halo interactions in the beam pipe. To help reject background muons, the tracks detected in the muon chambers are required to match to a corresponding

COT track. Also, if the time of flight of a muon is out of synch with the time of the collision by 30 to 40 ns[2], the muon signal is treated as a fake that originates from one of the above background sources.

The CDF II muon detection system consists of four subsystems. These subsystems are named the Central Muon Detector, the Central Muon Upgrade, the Central Muon Extension and the Intermediate Muon Detectors. Each subsystem is constructed from chambers and counters as shown in Fig. 3.20. The geometrical coverage of the muon system is shown in Fig. 3.21. Additional details on each of the four muon subsystems are given below.

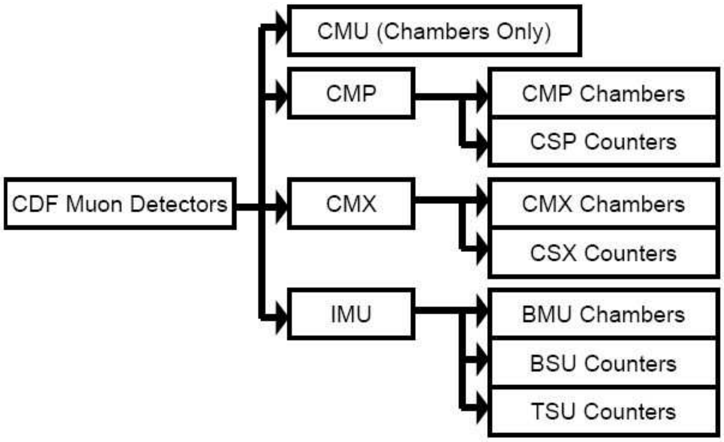

Figure 3.20: Hierarchy of the muon detector system.

Central Muon Chambers

The Central Muon Chambers (CMU) cover $|\eta| < 0.6$ and are embedded in the central calorimeter wedges at the location of the outer radius as shown in Fig. 3.22. The CMU chambers are mounted in a cylindrical geometry and are located at a radius of 347 cm. Because of the central calorimeter arch support structure and the HV fan out mounted on the end of the muon chambers, there is a 18 cm gap (at η =0) between the east and west CMU chambers. The CMU drift chambers are operated with a 50-50 Argonne-Ethane gas mixture. There are four

---

[2] nano second, ns = 10^{-9}s

stacked layers of 16 cells (4 wide by 4 high) in each CHA wedge. The cells in the CMU chambers run along the z direction (no η segmentation). The CMU cells are made of aluminum walls which are at -2500 V, and the sense wires are held at +2325 V. The charge collected from each end of the sense wire is used to determine the z position of the pulse in offline.

The most significant limitation in the performance of the CMU system is that it is located right after a small amount of absorber (i.e. only the calorimeters). With only $4.7\Lambda_0$ in the CHA, hadron showers generated in the CHA often leak into the CMU system (called punch-through) and result in fake muon signal in the CMU. Another limitation of the CMU is the large gap between the east and west wedges due to geometrical and mechanical constraints. The total gap between the east and west wedges add up to 16% of the total coverage. This implies that muons that end up in the gaps cannot be detected in the CMU. To complement the flaws of the CMU, we use the CMP muon detector which is located completely outside of the detector.

Central Muon Upgrade

The Central Muon Upgrade Detector (CMP) provides confirmation of muons with CMU tracks but with higher signal-to-background ratio. It consists of four layers of single wire drift cells. Each cell has a dimension of $2.5 \times 15 \times 640$ cm^3. The CMP is installed outside an additional 2 feet of steel that add $2.3\Lambda_0$ to the total absorber. This additional steel absorber reduces the hadronic punch-through background. Only information in the transverse plane is provided by the CMP. Unlike the other detectors in CDF, the stacks are arranged in a rectangular geometry around the beamline as shown in Fig. 3.23. This design provides full coverage in ϕ, but the η coverage ($|\eta| \leq 0.6$) depends on the corresponding ϕ as shown in Fig 3.21. A scintillator system (named Central Scintillator Upgrade, CSP) is installed on the outer surface of the CMP and provides additional timing information.

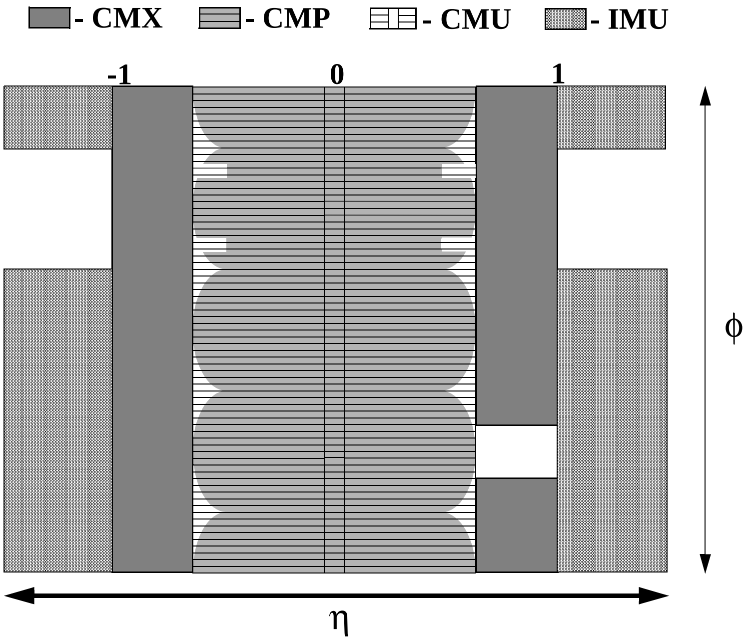

Figure 3.21: Segmentation of the muon chambers in ϕ and η.

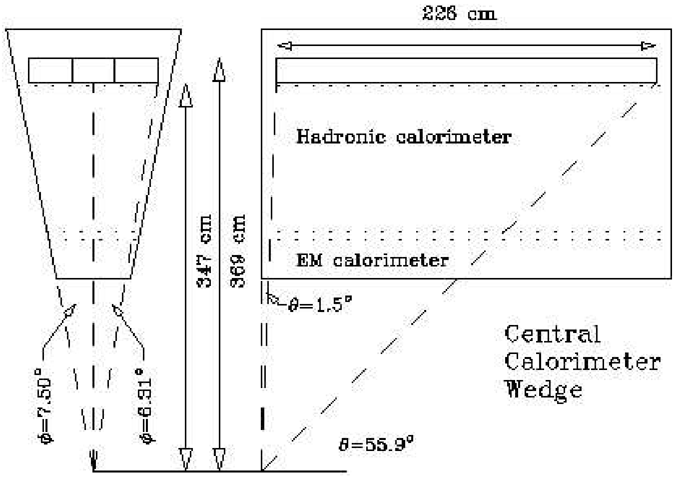

Figure 3.22: A CMU chamber embedded in a CHA wedge. End view on the left and side view on the right.

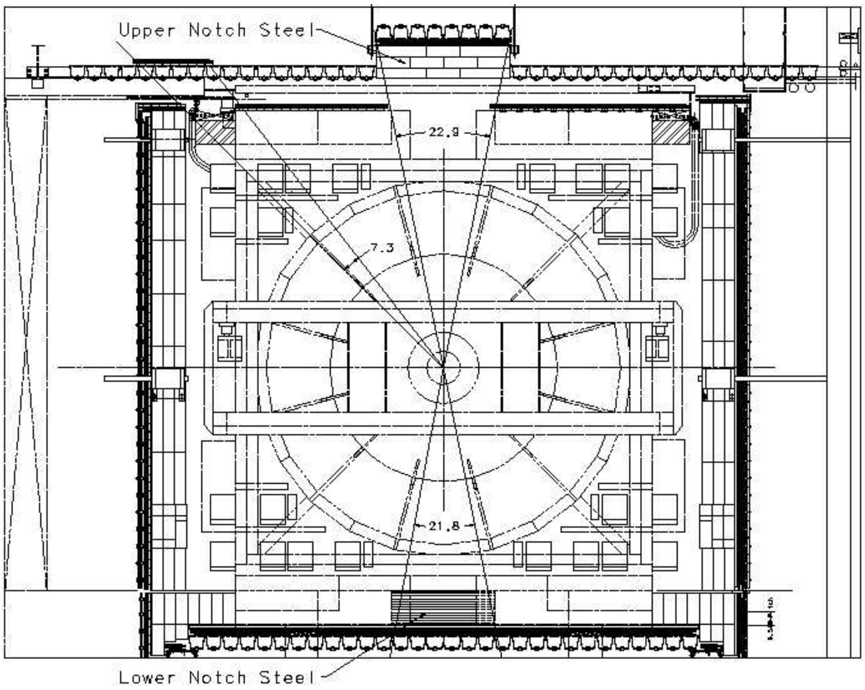

Figure 3.23: Location of the outer CMP muon system in the CDF detector hall.

Figure 3.24: CMX chambers (Arches) with yellow Toroid in the center.

Central Muon Extension

The Central Muon Extension (CMX) extends the geometrical coverage of the muon system up to $\eta \leq 1$. It is arranged in a cone as shown in Fig. 3.24. The CMX chambers consist of 24 wedges on each side as shown in Fig. 3.25. Each wedge covers 15° in ϕ. The CMX is divided into two parts. The upper conical section covers the upper 270° including the top 30°. The top 30° on the west side is called the "Keystone". On the east side, the coverage does not extend as much as on the west side because of interference with the cryogenic utilities that serve the solenoid. The upper conical sections except for the Keystone are called the "Arch". The lower 90° in ϕ has slightly different geometry due to the floor; this section is called the "Miniskirt".

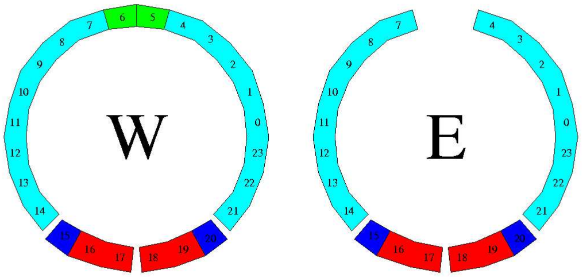

Figure 3.25: CMX ϕ coverage at the West and East sides of the detector.

There are eight layers of chambers per ϕ wedge. The drift cells used for the CMX are of the same construction as the chambers used for the CMP. However, the CMX chambers are shorter (180 cm long). The chambers in different layers of the CMX overlap with one another, thus eliminating any gaps in ϕ as shown in Fig. 3.26. Each chamber stack is sandwiched between two counters called the Central Scintillator Extension (CSX), which are used to provide fast timing for muons in the CMX. The CSX counters are installed for the chambers in the arch and keystone. In the miniskirt region, there is only one layer of scintillator. The

CMX Miniskirt scintillators (MSX) are located at the inner surface of the CMX miniskirt chambers.

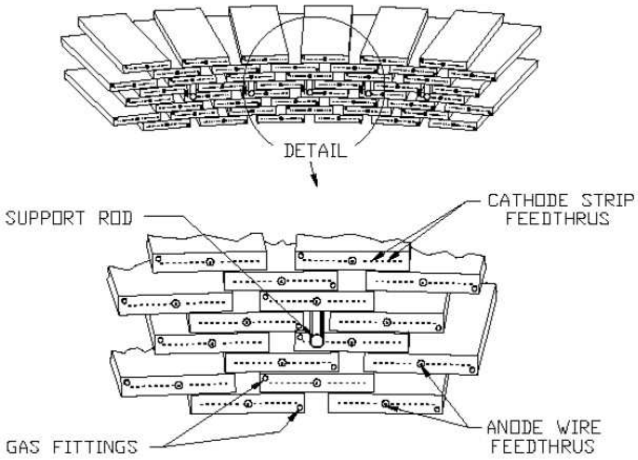

Figure 3.26: Overlap structure of eight layers of the CMX drift cells.

Intermediate Muon Detectors

The Intermediate Muon Detector (IMU) covers the forward region, $1.0 < |\eta| < 1.5$. It surrounds the forward iron Toroid as shown in Fig. 3.27. The IMU consists of the Barrel Muon Chamber (BMU), the Barrel Scintillator Upgrade (BSU) and the Toroid Scintillator Upgrade (TSU). The iron Toroid was magnetized in CDF Run 1. In CDF II, it only serves as additional absorber material in front of the IMU detectors.

The BMU covers the region $1.0 < |\eta| < 1.5$, but only three quarters of the circle in ϕ. The bottom 90° are not covered due to the support structures for the toroids. Each chamber has dimensions of 11.9 ft × 1 in × 3.3 in, covering 1.25 degrees in ϕ. Figure 3.28 shows the structures of the BMU and the BSU. The BSU is made of rectangular scintillators mounted on the outside of the BMU chambers. The TSU is made of trapezoidal scintillators located on the inner face of the toroid, perpendicular to the beamline. The timing information from the scintillation counters is used for the forward muon trigger.

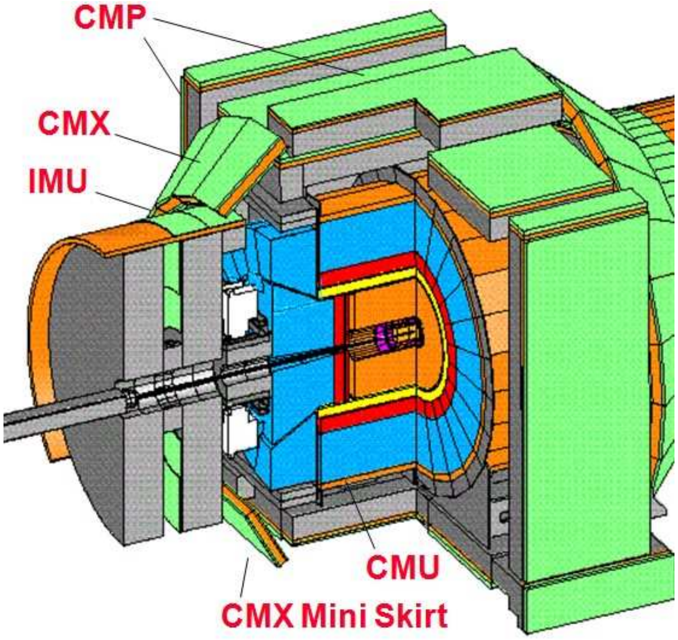

Figure 3.27: CDF Muon Systems. IMU is the forward muon detector surrounding the iron Toroid (forward disk). The drift chambers are colored in orange, the scintillators in green and the absorbers in gray.

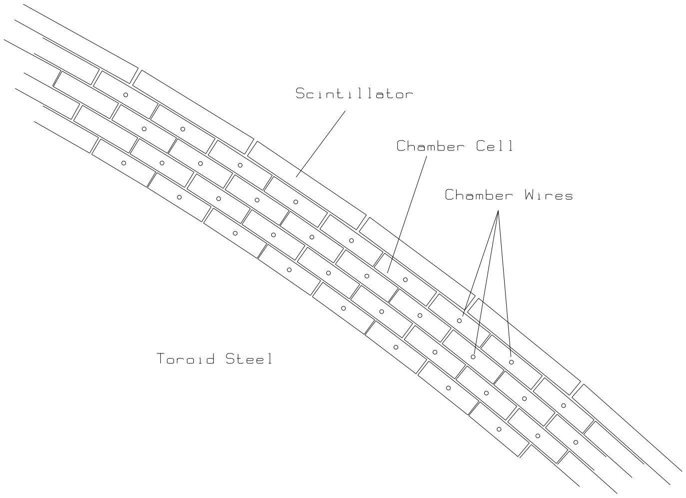

Figure 3.28: A detailed section of the IMU Barrel, showing several chamber cells and corresponding scintillator.

3.3.5 Luminosity Monitoring

The Cerenkov Luminosity Counter (CLC) is positioned at each side of the detector inside a 3° gap between the plug calorimeter and the beam pipe as shown in Fig. 3.29. The CLC detector is composed of two modules each containing 48 counters (3 layers of 16 counters), covering $3.7 < |\eta| < 4.7$. Each counter consists of a cone, 2 meter long and a few centimeters in diameter, made of aluminized mylar. The cones are oriented with their small end pointing towards the interaction point. The Cherenkov light produced by charged particles in the isobutane gas inside a cone is collected by a special light collector at the large end of the cone and directed to a PMT with a quartz window.

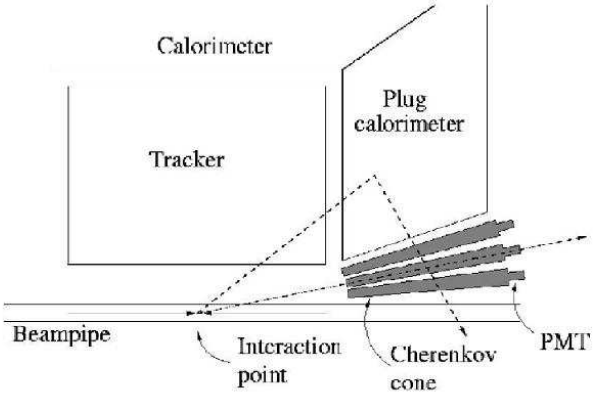

Figure 3.29: Side view of the CDF detector. The CLC is positioned inside a 3° forward gap between the beam pipe and the plug calorimeter.

The CLC monitors the average number of interactions per bunch crossing (μ). The information for the CLC is used for the computation of the instantaneous luminosity $\mathcal{L}$, which is given by $\mu f_{bc} = \sigma_{p\bar{p}}\mathcal{L}$, where f_{bc} is the frequency of bunch crossing in the Tevatron and $\sigma_{p\bar{p}}$ is the total $p\bar{p}$ cross section (about 100 mb at $\sqrt{s} = 1.96$ TeV). To measure μ, the CLC takes advantage of Cherenkov radiation produced by particles which move faster than the light speed in the isobutane gas. The Cerenkov light is radiated at a fixed angle (δ) with respect to particle's direction. The angle δ depends on the refractive index of the medium (n) and particle's velocity and is given by the equation $\cos\delta = \frac{1}{n\beta}$, where $\beta = v/c$. The uncertainty in the acceptance of the CLC is 4%. The CLC acceptance error in combination with the of 4% uncertainty in the value of the measured inelastic $p\bar{p}$ cross section yields an overall error of 6% for the integrated luminosity in CDF Run II [59].

3.3.6 The Time of Flight Counters

The Time of Flight (TOF) counters are composed of plastic scintillator bars read by fine mesh photomultipliers. The scintillators are installed in a barrel geometry between the COT and the cryostat of the solenoid. The approximate radius of the TOF detector is 140 cm from the beam pipe. The scintillator bars have dimensions of 4×4 cm^2 in cross-sectional area and 279 cm in length. There are a total of 216 bars, each covering 1.7° in ϕ and a pseudorapidity range $|\eta| < 1$. A photomultiplier tube (PMT) with a diameter of 1.5 inches is attached to the end of each bar. Since the PMTs are installed inside a magnetic field of 1.4 T, the gain of the PMTs is a factor of 500 lower than the nominal gain of 10^6 at zero magnetic field.

The TOF measures the time (t) that a particle traverses the TOF bars relative to the time of the beam crossing (the interaction time). The measured time in conjunction with the length of the track from the interaction point provides a direct measurement of a particle's velocity. The mass of a particle is calculated from the expression $m = \frac{p}{c}\sqrt{\frac{c^2t^2}{L^2} - 1}$, where p is the momentum of the particle and L is the total length of the particle's path. The TOF resolution of ≈ 100 ps provides at least a two standard deviation (2σ) separation between protons, $K^\pm$ mesons, and $\pi^\pm$ mesons for momenta $p < 1.6$ GeV/c as shown in Fig. 3.30. The TOF information complements the particle information from the specific ionization energy loss, dE/dx, which is measured in the COT, and allows for better pion and kaon identification. Additional details about the TOF system can be found in reference [60].

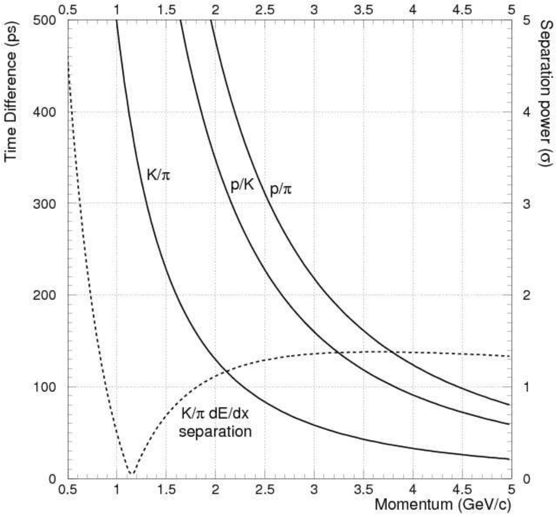

Figure 3.30: $K/\pi, p/\pi$ and K/p time difference as a function of momentum for a path length of 140 cm, expressed in ps and TOF separation power, assuming a resolution of 100 ps. The dashed line shows the K/π separation power from the $\frac{dE}{dx}$ measurement in the COT.

3.3.7 The Forward detectors

The CDF forward detectors include the MiniPlug Calorimeters (MP), the Beam Shower Counters (BSC), and the Roman Pot Spectrometer (RP) as shown in Fig. 3.31. The detectors are designed for the study of soft and hard diffraction processes. The forward detectors are also used to monitor the Tevatron beam losses.

Two MP detectors [61] are placed at each end of the CDF II detector, covering the range $3.6 < |\eta| < 5.1$. The MP detectors measure the energy and the η position of both charged and neutral particles. Each MP is constructed from alternating layers of lead plates and liquid scintillators. The liquid scintillators are read by optical fibers which transport the light to the PMTs. The MP (which does not have tower geometry) is housed in a cylindrical steel vessel which is 26" in diameter and has a 5" concentric hole for the beam pipe.

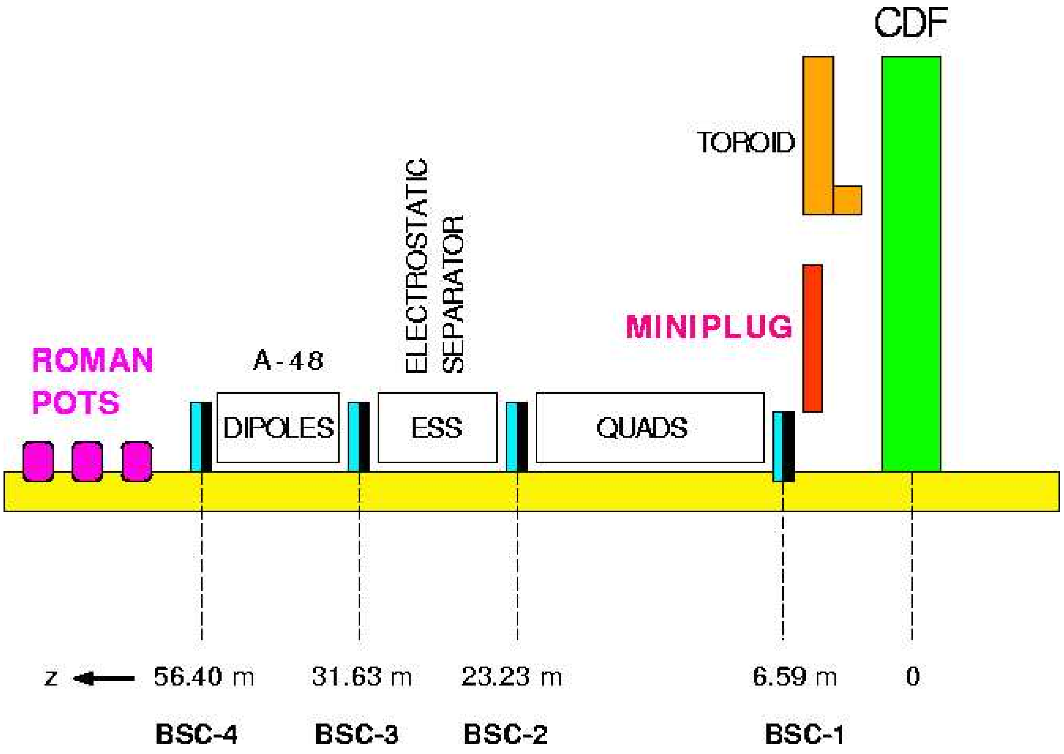

Figure 3.31: CDF forward detectors: Beam Shower Counters, Roman Pot Spectrometer, MiniPlug calorimeters.

The BSC are designed to detect particles traveling in either direction from the Interaction Point (IP). They are used to detect particles at high pseudorapidity ($5.4 < |\eta| < 7.5$), which corresponds to very small angles relative to the beam pipe. The BSC also provides information on beam losses in the Tevatron. The BSC detector is composed of four stations in the west side and three in the east side. Each station utilizes two scintillation counters housed in two sub-stations separately. The closest station to the IP (BSC-1) has four counters. The counters are placed around the beam pipe.

The Roman Pot Spectrometer is composed of three Roman Pot stations located about 57 m from the IP. The three Roman Pots are placed one meter apart from each other. Each Pot consists of 80 scintillator fiber channels and a scintillator counter. It measures the diffracted angle of antiprotons after passing the B0 collision point which is followed by a dipole magnet.

3.3.8 Triggers and Data Acquisition System

The Triggers and Data Acquisition systems are designed to accommodate the high rates and large data size in Tevatron Run II. The Tevatron provides $p\bar{p}$ collisions every 396 ns, which corresponds to about 10 millions collisions per second at peak luminosity of $\approx 3 \times 10^{32}\text{cm}^{-2}\text{s}^{-1}$. However, the dominant collisions are protons and antiprotons passing through each other and exchanging only small amount of momentum. Such low momentum transfer collisions are not of interest to the CDF physics program. In addition, recording such a large number of events requires enormous resources to collect 1.8 TB (tera bytes) of data per second.

CDF employs a trigger system to select the events of scientific interest. An overview of the trigger system is shown in Fig. 3.32. The trigger system consists of three levels: Level 1 - a hardware trigger, Level 2 - a combination of hardware and software triggers, and Level 3 - a pure software trigger. Through the three-level trigger system, CDF selects only about 110 events every second (out of the 10 millions collisions per second). The selected events are recorded by the CDF data logger system (CSL) in files, and are stored in the Fermilab Feynman Computing Centers (FCC). Further description of the data flow, from detectors to tape, follows below. Technical details about the trigger system and the Data Acquisition (DAQ) system are given in reference [62] and [63].

Level 1 Trigger

The Level 1 trigger (L1) is a synchronous system with 132 ns clock. Every 132 ns, the L1 trigger reads out the event information from the detector, stores it in a data pipeline, and makes a decision (accept or reject) for each event. This decision is made at the end of the 14-crossing deep data pipeline (5.5 μs). The L1 trigger uses fast initial data (primitives) from single tower energy measurements in the calorimeters, information from the online fast track processors in the COT, and hit towers in the muon systems. CDF employs sixty-four Level 1 trigger components. Each L1 trigger component uses a particular logical combination process on the primitives. Out of 10 M collisions per second, L1 accepts 20 k events per second and transfers the information to the Level 2 trigger.

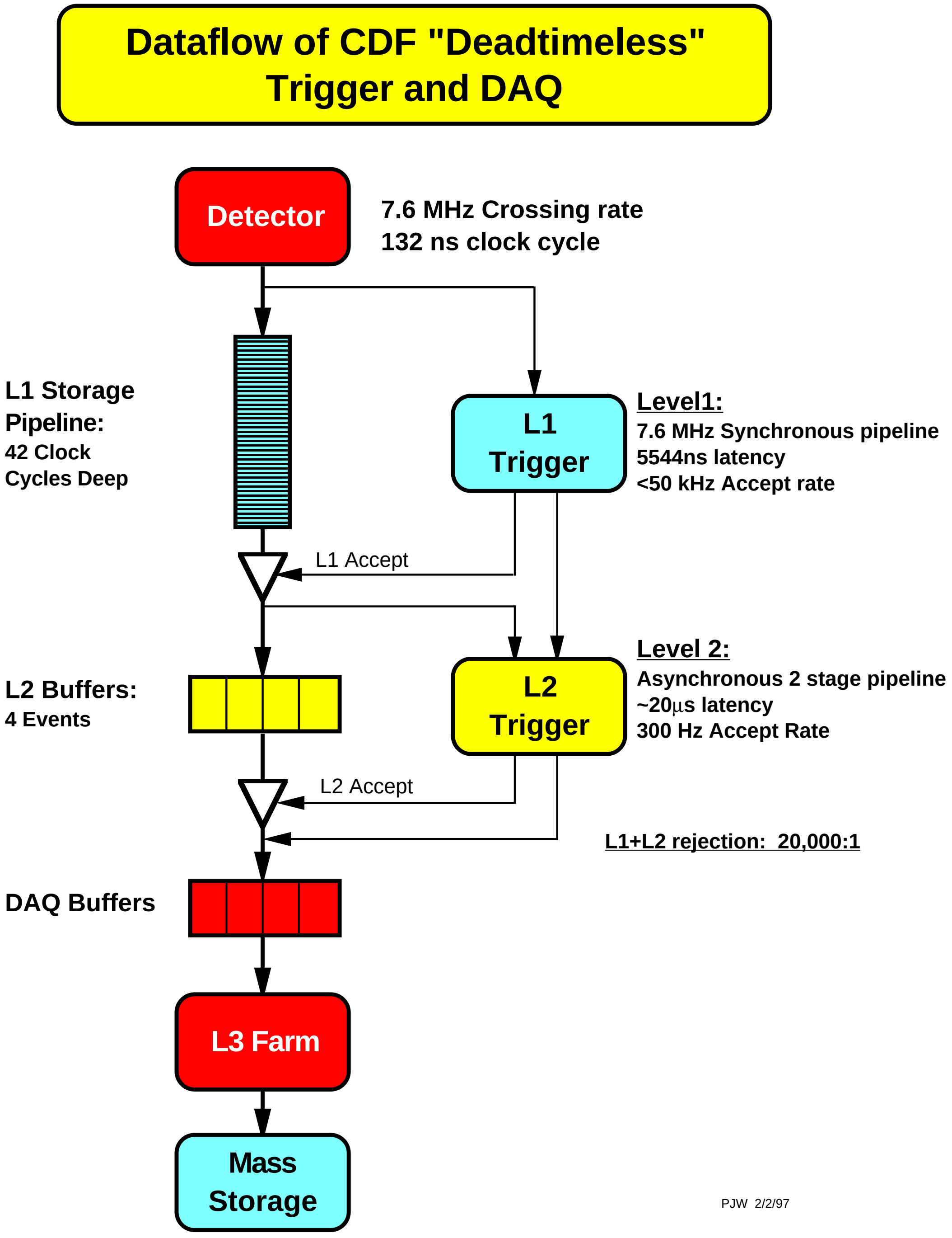

Figure 3.32: Functional block diagram of the CDF II data flow.

Level 2 Trigger

The Level 2 trigger (L2) processes the events transferred from L1 asynchronously. The L2 decision is based on more refined data and additional tracking information from the silicon detector. Therefore, a longer time ($\approx 30\mu$s) per event is required to make a L2 decision than is needed by L1.

The L2 system employs a two-stage pipeline. The first stage gathers information from the Central EM ShowerMax Chamber (CES), axial strips of the Silicon vertex detector (SVX), and corrected calorimeter energy that sums the energy from neighboring towers to that of the seed tower. This information is stored in memory together with the L1 primitives. The second stage uses the online programs to match the measured calorimeter energy with tracks (CES+tracker) and programs to find tracks with a displaced vertex (SVX+tracker). The second stage of L2 provides additional filters to select signal events for many low rate physics processes and reduce backgrounds from other higher rate processes which are not of interest.

With a total of ~ 130 individual triggers, L2 accepts about 400 events per second. The events selected by L2 are sent to the Event Builder (together with the L1 primitive information).

Event Builder and Level 3 Trigger

The Event Builder consists of custom built hardware used to assemble and package data fragments from the sub-detectors. Software converters receive events from the Event Builder and send all the data for an event to a Level 3 processor node. The Level 3 trigger system (L3) is a Personal Computer (PC) farm of parallel processors. In the processor, the data are first rearranged in a "reformatter" and then the "filter" fully reconstructs the event. The L3 trigger decision is made based on more accurate processed information from detailed trigger requests from individual L3 trigger components. Currently ~ 190 L3 trigger components are used. The selected events are tagged and each event is sorted into one or two of a total of eight data streams according to its property. For example, events which include a high p_T electron are fed into stream B, and events with jets are fed into stream G. If an event satisfy both conditions, including a high p_T electron and many jets, the event has both tags of stream B and G. In current operation, we have about 10% overlaps between streams. Finally, the events are transferred to the data Logger (CSL) through the L3 output nodes at a rate of 110 Hz.

Data Logger and Data Quality Checks

The Consumer Server Logger (CSL) is the last part of the CDF II data acquisition system. It takes fully reconstructed events from the L3 output nodes and writes them into files according to the L3 stream tags. On average about 20 MB of data are recorded every second. At the end of 2006, the CSL was upgraded for high luminosity stores. The new CSL uses off-the-shelf hardwares and is comprised of nine parallel nodes connected to one another via a private network with broad bandwidth [64]. With the new design, the CSL has the capability of taking input data at a rate of 100 MB/s. As an aside we note that this rate is close to the expected input rate to the data logger in the future CMS experiment at the Large Hadron Collider at the CERN accelerator complex in Geneva, Switzerland. The CSL employs a large storage buffer to keep three full days of data taking with input events at a rate of 80 MB/s.

Some of the data is copied to the Consumer systems for real time checks of data quality and detector performance. This allows for immediate response to any problem that is found while taking data. A block diagram of the data acquisition system is shown in Fig. 3.33. Part of the physics data sample is also copied to a lookup area for detector calibrations and for quick preliminary analyses as desired.

Once the physics events are written into files by the CSL, the files are delivered to the FCC and stored on tape. The stored data in the FCC are reprocessed using corrections from the detector calibrations. This re-calibration yields the final production data for use in various Physics analyses.

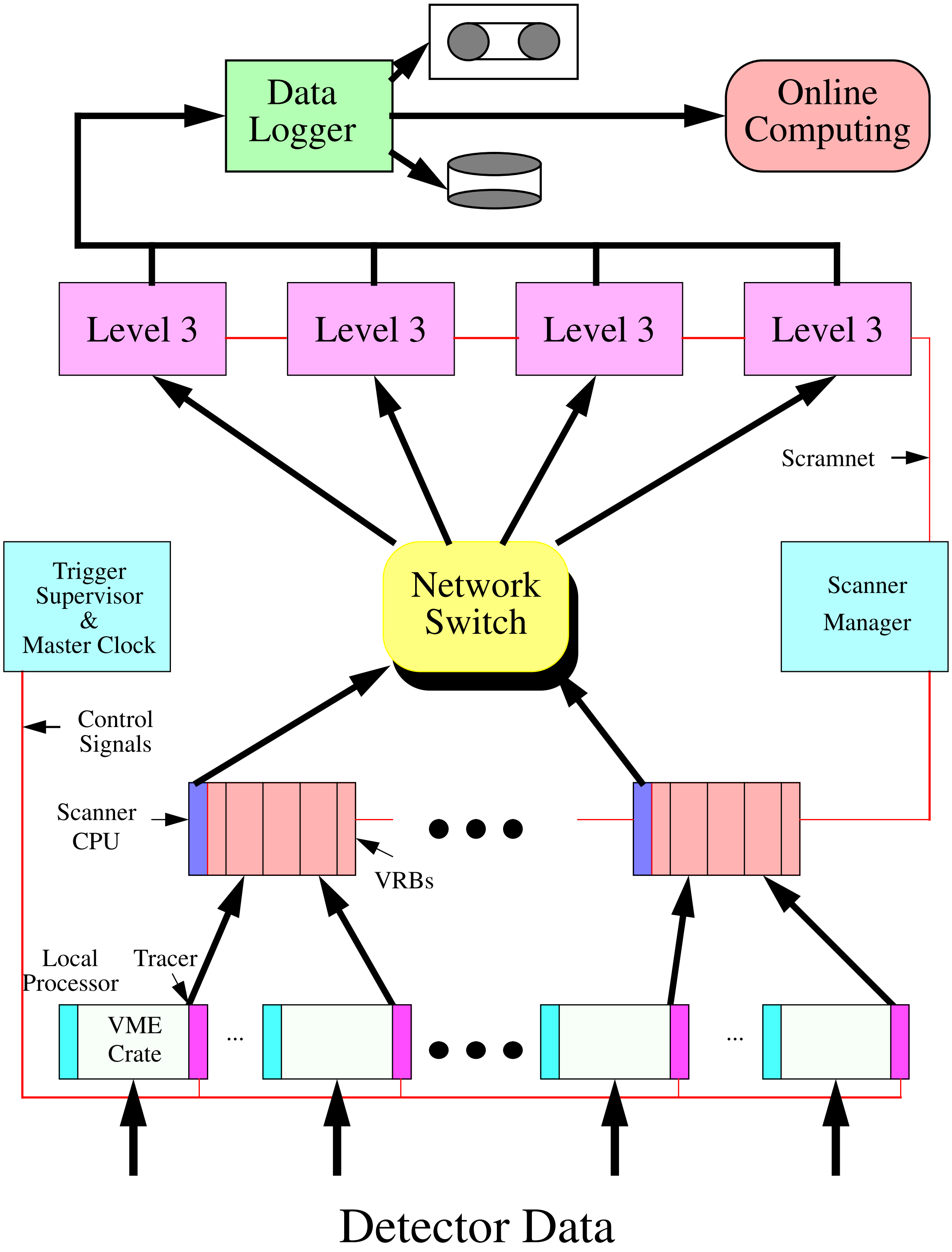

Figure 3.33: A schematic of the CDF II Data Acquisition system, showing data flow from the front-end and trigger VME crates to the Online Computing system.

Chapter 4

Event Selection

Topics discussed in this chapter include the selection criteria for the lepton+jets $t\bar{t}$ events; the determination of the acceptance for W and Higgs in $t\bar{t}$ events from MC simulation samples; and the estimation of various backgrounds in the selected $t\bar{t}$ events.

4.1 $t\bar{t}$ Samples

4.1.1 Strategy for Event Selection

In the Standard Model top quarks are mostly produced in pairs, and each top quark exclusively decays to a W boson[1] and a bottom quark. The $t\bar{t}$ events are categorized by the various decay modes of the W bosons in the final state. The W boson decays into a charged lepton and a neutrino in 11% of the time for each lepton type. The terms *leptonic* and *tauonic* W are used to describe the $e\bar{\nu}_e/\mu\bar{\nu}_\mu$ and $\tau\bar{\nu}_\tau$ final states, respectively. The rest W bosons decay to hadrons $(q\bar{q}')$, where $q = (u,\ c)$ and $q' = (d,\ s,\ b)$, or the other way around, depending on the charge of the W boson. These W boson decays are called *hadronic* W final states. If both W bosons decay hadronically (leptonically), the $t\bar{t}$ event is categorized into an all-hadronic (dilepton) channel. If either of the W bosons decays into $\tau\bar{\nu}$, the event is categorized as a $t\bar{t}$ event in the tauonic channel. A

---

[1] W boson generally means both charged bosons, $W^{\pm}$.

$t\bar{t}$ event for which the final state includes one leptonic W and one hadronic W is categorized as a $t\bar{t}$ event in the lepton+jets channel. The production rates for $t\bar{t}$ events in various decay channels are compared to one another in Fig. 4.1.

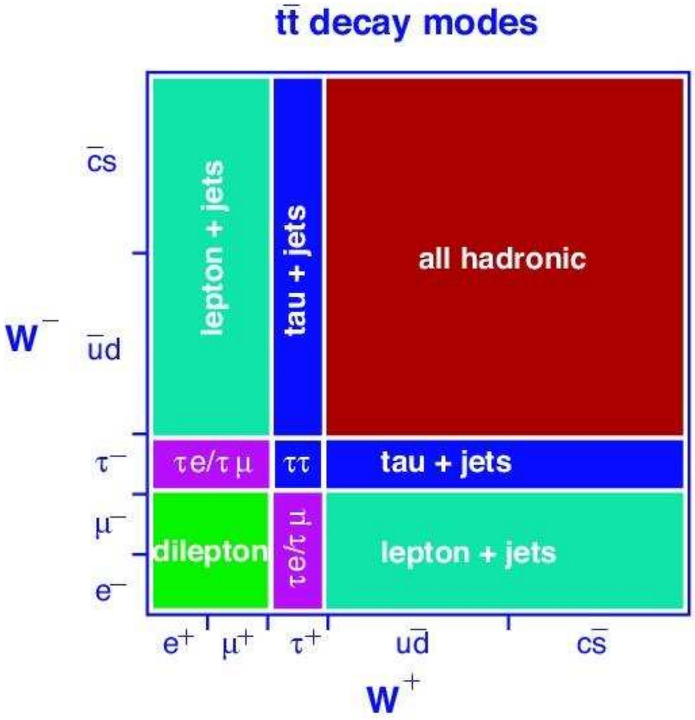

Figure 4.1: Production rates for $t\bar{t}$ events in each category.

In this analysis, we use the $t\bar{t}$ events in the lepton+jets channel. This channel is characterized by a high p_T lepton, multiple jets, and a large imbalance of the sum of measured energy in the transverse plane (from the final state neutrino). This combination of several high p_T objects distinguishes $t\bar{t}$ events from other SM processes, and has the best signal-to-background ratio when compared to the other $t\bar{t}$ decay channels. Here we search for the top quark events in which the top quark decays to a charged Higgs boson[2] (H^+) followed by a Higgs decay to $c\bar{s}$ (dijet). The lepton+jets channel is ideal for finding the charged Higgs signal in the invariant mass spectrum of dijets in the final state.

---

[2] H^+ implies both charged Higgs bosons, $H^{\pm}$.

4.1.2 H^+ Monte Carlo Samples

The H^+ bosons with a $c\bar{s}$ decay in a $t\bar{t}$ event is described in Fig. 4.2. The $c\bar{s}$ decay gives the same dijet final state as for the hadronic W boson in the SM $t\bar{t}$ event sample. Therefore, the only difference between H^+ and W bosons is the invariant mass of dijet. Both H^+ and W bosons in $t\bar{t}$ events are simulated using the PYTHIA Monte Carlo (MC) program [65], assuming a top quark mass of 175 GeV/c^2. The simulation parameters of the hadronic decays of H^+ and W bosons are described in Table 4.1. The MC samples are simulated realistically to reflect the actual run (time) dependence of the performance of the CDF II detector.

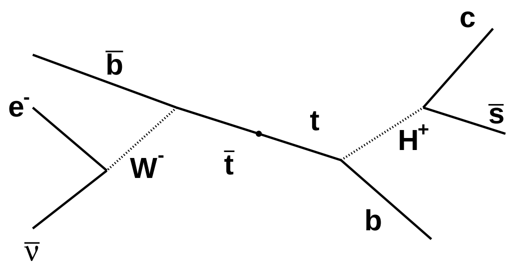

Figure 4.2: Tree level diagram of charged Higgs (H^+) production in decays of $t\bar{t}$ events in the lepton+jets channel.

Simulation parameter	H^+	W
Mass	60∼150 GeV/c^2	80.4 GeV/c^2
Width	0	2.12 GeV/c^2
Spin	0	1
Decay mode	$c\bar{s}$	$q\bar{q}'$ (q, q' = u, d, s, c, b)

Table 4.1: Simulation parameters for H^+ and hadronic W in top quark decays.

The charged Higgs MC sample is generated by forcing the top quark decaying into a H^+ boson and a bottom quark, and by forcing the antitop quark decaying to an antibottom quark and a $W^-(\rightarrow e/\mu/\tau + \bar{\nu})$, exclusively. Then, the H^+ is forced to decay into $c\bar{s}$ with zero width. The H^+ samples are generated with various H^+ masses ranging from 60 to 150 GeV/c^2. In order to check for a possible charge related bias in the simulation, an additional 120 GeV/c^2 Higgs sample is generated with a negative charged Higgs in the final state (which is the charge conjugate process). Details on the check for a possible charge bias in the H^+ simulation sample are given in Sec. 4.3.

4.2 $t\bar{t}$ Selection Criteria

In $p\bar{p}$ collisions in the Tevatron, a large fraction of the initial state energy is used to produce massive top quark pairs. Thus $t\bar{t}$ events are hardly boosted in the beam direction. Particles in the final state such as leptons, the four quarks (i.e. hadronic jets), and neutrinos (i.e. missing E_T) originating from the decays of high mass top quarks are produced with large transverse energy. The lepton+jets $t\bar{t}$ candidates are selected by following requirements:

- Events are selected through a high p_T electron or a high p_T muon triggered data stream.
- Events are only selected during a time period for which all detectors including the Silicon Vertex detectors were in operation.
- A central isolated electron with $E_T > 20$ GeV in the CEM, or a muon with $p_T > 20$ GeV/c, as detected in the CMU(P)/CMX [Sec. 4.2.1] [Sec. 4.2.2] is required.
- At least four hadronic jets in the final state. The most energetic four jets are designated as the leading jets [Sec. 4.2.3]. The four jets are required to have $E_T > 20$ GeV and $|\eta| \leq 2.0$. Here, the energies of jets are corrected up to Level 5 (corrected to yield particle jet energy, see Sec. 4.2.3).
- At least two jets out of the four leading jets must have a secondary vertex [Sec. 4.2.3].
- A missing transverse energy $\not{E}_T > 20$ GeV [Sec. 4.2.4] is required.

- Events which include more than one lepton or a Z^0 boson are removed. [Sec. 4.2.2]
- For CMX muon events, we exclude the early CDF II data (acquired up to August 2002) due to CMX malfunction during that period. We also exclude CMX muons which point at the Keystone or at the Miniskirt [Sec. 3.3.4].

Details of the selection criteria for each type of final state object, and various corrections are described in following subsections.

4.2.1 Electron Identification

During real time data taking, events with a high p_T electron are triggered by a high-p_T track in the COT and a large energy deposition in the CEM calorimeter. Later, the electron object is fully reconstructed in offline.

The electron energy (E) is clustered by merging the energy of the most energetic EM tower (seed tower) with the energy of the second energetic neighboring tower in η. Its transverse component (E_T) is calculated by $E \cdot \sin\theta$, where θ is the polar angle of the COT track pointing to the seed tower of the cluster with respect to the proton direction. The energy E is corrected to account for non-linear effects and the known differences in the calibration between the calorimeter towers. A larger electron cluster (3-tower E) is reconstructed by adding another azimuthal neighboring tower to the nominal electron cluster, and is used in a few electron selection criteria. The electron momentum is measured from the COT track which is matched with the electron signal in the calorimeter. The track momentum (p) is extracted from its curvature in the COT. As is done for E_T, the transverse momentum (p_T) is equal to $p \cdot \sin\theta$, where the θ is the polar angle of the track.

Table 4.2 summarizes the details of the electron selection criteria. The fiducial requirement (selection criterion i) ensures that only well instrumented CEM towers are used for the electron energy measurement. We require an energetic electron with high p_T in selection criteria ii and iii.

Although a photon does not have a track in the tracker, it is possible that a track accidentally points at a photon energy cluster faking an electron. In this

(i)	Fiducial
(ii)	$E_T \geq 20$ GeV
(iii)	$p_T \geq 10$ GeV/c
(iv)	$E/p \leq 2$ unless track $p_T \geq 50$ GeV/c
(v)	E_{HAD}/ 3-tower $E_{\mathrm{EM}} \leq 0.055 + 0.00045 \times E$
(vi)	No conversion electron
(vii)	$L_{shr} \leq 0.2$
(viii)	Isolation: Iso E_T (R=0.4)/$E_T \leq 0.1$
(ix)	$\lvert$Track $z_0\rvert \leq 60$ cm & $\lvert$vertex-track $z_0\rvert < 5.0$ cm
(x)	COT: ≥ 3 Axial & ≥ 2 Stereo SLs with 5 hits each
(xi)	$\lvert\Delta z\rvert < 3$ cm & -3 cm $\leq$ Q $\cdot\Delta x \leq 1.5$ cm
(xii)	$\chi^2_{strip} \leq 10$

Table 4.2: High-p_T electron selection criteria in the central region ($|\eta| \leq 1.0$).

case, the p_T of the track is generally much lower than the energy of the photon in the CEM. The cut on the ratio of the electromagnetic (EM) calorimeter energy to the momentum of the track (selection criterion iv) reduces the number of such faked electron signal.

Charged hadrons are rejected by a cut on the ratio of energy deposited in the hadronic calorimeter (E_{HAD}) to the energy in the EM calorimeter (E_{EM}) (selection criterion v). The small energy leakage into the hadron calorimeter for a very energetic electron is accounted for by using an energy dependent $E_{\mathrm{HAD}}/E_{\mathrm{EM}}$ cut.

Electrons interact in the EM calorimeter (see Sec. 3.3.3) and radiate photons. Each photon interacts in the calorimeter and produces secondary e^+e^- pair. The production of lower energy photons and e^+e^- pairs continues until all the electron's energy is absorbed in the EM calorimeter. The electron can interact with other materials before reaching calorimeters. An electron or positron which originates from a photon decay in the silicon or COT tracker is called a "conversion" electron, and is removed from the electron listings (selection criterion vi). In the calorimeter, the electromagnetic shower of the conversion electron is wider than the electromagnetic shower of a real electron. Selection criterion vii is a cut on the variable L_{shr}[3] which is a measure of the electron's lateral shower profile. The variable L_{shr} is typically a two-tower sum. A large L_{shr} implies the presence of additional particles in the EM calorimeter near the location of the electron object. Therefore an electron candidate with broad shower is rejected in (vii).

Finally we cut on the isolation ratio variable (selection criterion viii) to reject electrons in jets: electrons originating from charm or bottom quark decays, or neutral pions. The isolation ratio is the transverse energy (EM+HAD) deposited within a cone size ΔR $(=\sqrt{(\Delta\eta)^2 + (\Delta\phi)^2})$ of 0.4 surrounding the electron track divided by the transverse energy of the electron. Selection criterion viii discriminates the isolated signal electrons against the electrons in jets by requiring an electron which is well isolated from other nearby particles.

The vertex (z_0) of a reconstructed COT track is required (selection criterion ix) to be within ± 60 cm with respect to the center of the detector (± 60 cm is the reliable luminous region for proton-antiproton collisions at CDF). The quality of the electron track is determined by the number of hits in the COT super-layers (selection criterion x). In order to identify the electron track, the distance between the point where the track is extrapolated at the surface of the CES and the centroid of the electromagnetic shower in the CES is required to satisfy a matching condition (selection criterion xi). The effect of the track charge (Q) is accounted for in this requirement. Finally, shape of the shower profile in the CES is required to be consistent with test beam results (selection criterion xii).

The efficiency of the central electron selection is determined using the high statistics $Z \to e^+e^-$ data sample. We select good electron candidates by requiring the invariant mass of the e^+e^- to be within Z boson mass window (76.2 GeV/c^2 $<$ m(e^+e^-) $<$ 106.2 GeV/c^2). Then, one electron is required to pass all the selection cuts, and the other electron is used to determine the efficiency of the

---

[3]
$$L_{shr} = 0.14 \sum_i \frac{E_i^{\text{measured}} - E_i^{\text{expected}}}{\sqrt{(0.14\sqrt{E})^2 + \sigma^2_{E_i^{\text{expected}}}}},$$

where the index i runs over towers, E_i^{measured} is the energy measured in tower i, and E_i^{expected} is the energy expected in the tower as determined from test beam data. The error in the energy measurement is represented by $0.14\sqrt{E}$ and $\sigma^2_{E_i^{\text{expected}}}$ is the uncertainty in the energy estimate.

cuts. The electron efficiency is measured to be $\epsilon_{\mathrm{data}} = 0.799 \pm 0.002$ from data, and to be 0.814 ± 0.001 from a $Z \rightarrow e^+e^-$ MC sample. To compensate for the disagreement between data and the MC, a global scale factor of 0.981 ± 0.004 is applied to the MC simulation sample.

4.2.2 Muon Identification

A muon is two hundred times heavier than an electron, and penetrates the calorimeters with little energy loss. Therefore, the muon detectors are placed behind a significant amount of material. CDF has three central muon systems: CMU, CMP, and CMX. The CMP is located behind the CMU, and both CMU and CMP cover the detector η region of -0.6 to 0.6. The CMP has a lower background rate than the CMU because of the additional absorber between the CMU and CMP. Muons which are reconstructed in both the CMU and CMP are called CMUP muons. The CMX extends the muon coverage up to $|\eta| = 1.0$. However, the ϕ coverage of the CMX is incomplete due to the space limitations. We use the muons which direct to the CMX Arches only (see Fig. 3.24 in Sec. 3.3.4).

During data taking, events with a high p_T muon are selected by triggers which require a high p_T track in conjunction with timing information from the muon scintillators. Then, the muon signal is identified using additional information in the offline reconstruction. A muon signal that is present in a pair of adjacent stacks comprise a tower, and is called a stub. There are muon candidates which fail the muon selection requirements or direct to the non-fiducial region. These are called stubless muons [66]. Stubless muons are not included in the high-p_T muon candidates for leptonic W bosons. However, the presence of a stubless muon is counted as an additional lepton, and events with two or more leptons are removed.

The muon selection criteria are listed in the Table 4.3. Selected muons must be identified in the well instrumented region of the detector in i, and must have high p_T in ii. Selection criteria iii and iv require that the muon deposits only a small amount of energy in the EM and HAD calorimeters, respectively. Selection criterion v requires an isolated muon by the ratio of the total energy within ΔR of 0.4 surrounding the muon track to the p_T of the muon track to be than 0.1.

(i)	Fiducial
(ii)	$p_T \geq 20$ GeV/c
(iii)	$E_{\text{EM}} < 2$ GeV + max(0,0.0115*(p-100))
(iv)	$E_{\text{HAD}} < 6$ GeV + max(0,0.028*(p-100))
(v)	Isolation: Iso E_T (R=0.4)/p_T < 0.1
(vi)	No cosmic muon
(vii)	$\lvert d_0\rvert$ <0.02 cm with silicon hits or $\lvert d_0\rvert$ <0.2 cm
(viii)	|Track z_0| $\leq$ 60 cm & |vertex-track z_0| < 5.0 cm
(ix)	COT: $\geq$ 3 Axial & $\geq$ 2 Stereo SLs with 5 hits each
(x)	$\chi^2_{track} \leq 2.3$
(xi)	for CMUP: $\lvert\Delta x(\text{CMU})\rvert < 7$ cm, $\lvert\Delta x(\text{CMP})\rvert < 5$ cm
(xii)	for CMX: $\lvert\Delta x\rvert < 6$ cm, $\rho_{\text{COT}} > 140$ cm

Table 4.3: High-p_T muon selection criteria in the central region (CMUP: $|\eta| \leq 0.6$, CMX: $0.6 \leq |\eta| \leq 1.0$)

There are several sources of muon backgrounds. The backgrounds include real muons that originate from cosmic rays or in decays of hadrons including bottom, charm, or strange quark. Other backgrounds originate from hadrons which penetrate through the calorimeters (punch-through), from particles produced in the interactions of protons with the beam pipe, and from proton-antiproton interactions which occur outside the fiducially defined luminous region. Selection criteria vi and vii on the muon impact parameter[4] are used to reject the listed backgrounds above.

The muon track selection criteria viii and ix are the same as the corresponding selection criteria for electron tracks. Selection criterion x imposes a cut on the quality of the track reconstruction.

Selection criterion xi requires a match between the COT track and the muon stub. Here, the distance ($|\Delta x|$) between the position of the COT track extrapolated to the location of the muon chambers and the position of the muon stub in each muon chamber is required to be small.

Selection criterion xii imposes fiducial requirement on the CMX muon candidates. In addition to the matching between a COT track $\rightarrow e^+e^-$ and a muon stub, the muon track is required to pass a cut on the COT exit radius (ρ_{COT}).

---

[4] Impact parameter (d_0) is the shortest distance between the vertex (z_0) and the COT track.

The central high p_T muon efficiency is estimated using $Z \rightarrow \mu^+\mu^-$ events which are selected to have an invariant mass between 81 GeV/c^2 to 101 GeV/c^2. As is done in the electron analysis, one muon is required to pass all the selection criteria, and the other muon is used to measure the efficiency. The global scale factor ($\frac{\epsilon_{DATA}}{\epsilon_{MC}}$) is determined to be 0.9242 ± 0.004 for the CMUP muons, and 0.9944 ± 0.006 for the CMX Arch muon.

4.2.3 Jets

Quarks and gluons carry color charges. Because of QCD confinement they cannot exist in a free quark or free gluon state, but fragment into hadrons. When quarks and gluons are created with high energy, they radiate gluons and create series of quark-antiquark pairs and gluons from vacuum. Then, the quarks and gluons form color neutral mesons ($q\bar{q}$) or baryons (qqq), which are collectively referred to as hadrons. This process is called *hadronization*.

In decays of top quarks, final state quarks are created with high energies, and each quark forms a cluster of hadrons through the hadronization process. The hadron cluster is called a jet. The four final state quarks in the lepton+jets $t\bar{t}$ events are found as four jets in the calorimeter. The jet reconstruction and jet energy corrections are described below.

Jet Reconstruction

In this analysis, jets are reconstructed using a cone algorithm [67] with a fixed cone size. The center of a jet is defined as (η^{jet}, ϕ^{jet}). The sum of the energy deposits in both EM and hadronic calorimeter is used to determine E_T for each calorimeter tower. The jet clustering begins with lining up the towers with $E_T > 1$ GeV in order of decreasing energy. Each tower is investigated as a possible seed tower. At first, we start with the most energetic tower on the line as a possible center of a jet. Then the towers within a radius of ΔR ($= \sqrt{(\eta^{tower} - \eta^{jet})^2 + (\phi^{tower} + \phi^{jet})^2}$) of 0.4 w.r.t the center of jet are merged to form a cluster. Then, the center of the jet is recalculated as towers are added:

$$E_T^{jet} = \sum_{i=0}^{N_{tow}} E_{Ti}, \tag{4.1}$$

$$\phi^{jet} = \sum_{i=0}^{N_{tow}} \frac{E_{Ti}\phi_i}{E_T^{Jet}}, \tag{4.2}$$

$$\eta^{jet} = \sum_{i=0}^{N_{tow}} \frac{E_{Ti}\eta_i}{E_T^{Jet}}, \tag{4.3}$$

where N_{tow} is the number of towers inside the cone. When the entire list of towers is checked for the first cluster, this algorithm clusters a second jet using remained towers in the list. This procedure is repeated until all the jets are reconstructed.

Each tower can belong to only one jet cluster, and double counting is not allowed. If two jets overlap by more than 75%, the jets are merged. Otherwise each tower in the overlap region is assigned to its nearest jet. Additional details on the jet clustering procedure are presented elsewhere [68].

Jet Energy Correction

In the offline data production, the measured calorimeter energies are first corrected for the calibration differences between towers (prior to jet reconstruction). Then, a series of corrections are applied to the jets in order to determine the initial energy of the parent parton. Corrections are applied to account for the non-linearity of detector response and for the systematic biases originating from the jet clustering algorithm. Here we describe the generic (*flavor independent*) corrections applied to each clustered jet with a fixed cone size of 0.4. In addition, there are flavor dependent corrections which are applied to jets produced in decays of top quarks. These flavor dependent corrections are described in a later section (Sec. 5.1).

In general, a parton hadronizes to form a calorimeter jet via three steps as shown in Fig. 4.3. Most of the corrections to the jet energies are obtained from dijet and γ+jets event samples. However, corrections in later steps to determine the initial parton energy must rely on MC simulation.

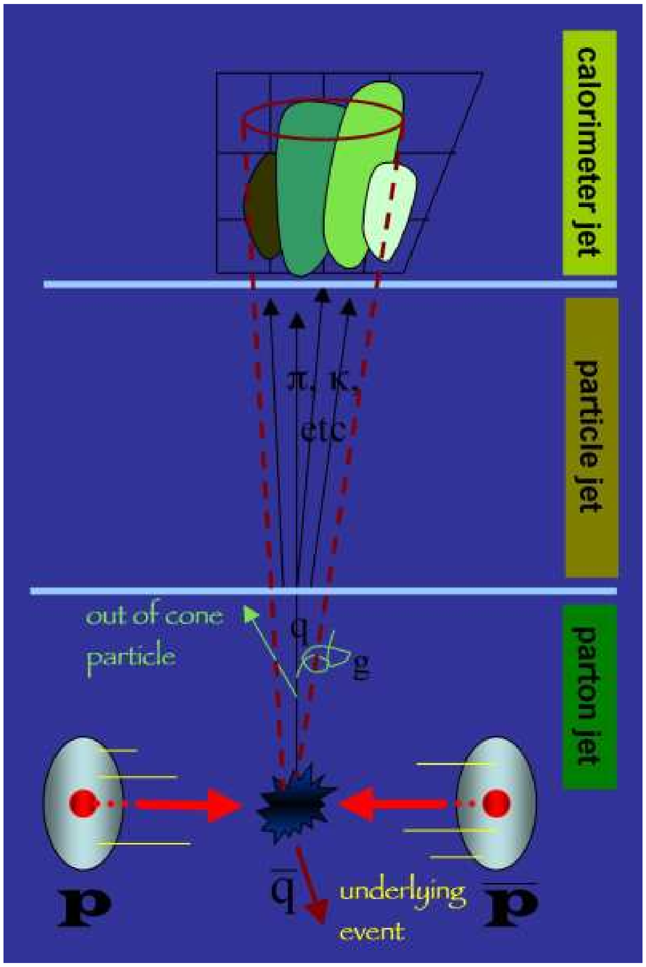

Figure 4.3: The process of jet formation starting with an initial parton and ending with a final hadron cluster in calorimeter.

A set of multiplicative and additive correction factors are given to the raw E_T of each calorimeter jet to determine the initial parton energy by following expression:

$$\begin{aligned} p_T{}^{parton} &= (p_T{}^{jet} \times C_{\mathrm{REL}} - C_{\mathrm{MI}}) \times C_{\mathrm{ABS}} - C_{\mathrm{UE}} + C_{\mathrm{OOC}} \\ &= p_T{}^{particle} - C_{\mathrm{UE}} + C_{\mathrm{OOC}}. \end{aligned} \tag{4.4}$$

By convention, each correction step is labeled numerically from 1 to 8, and the description of each step follows in this subsection. The Level 2 and 3 corrections are obsolete for the present CDF II jet energy analysis. There is no additional energy correction in Level 8, and only an additional systematic uncertainty is assigned.

- **L1 - Relative Scale (C_{REL}):** This correction is referred to as "eta-dependent energy correction" [69]. The forward calorimeters have cracks and non-instrumented regions which result in a non-linear and η dependent response. The correction is extracted by assuming transverse energy balance in the dijet sample as shown in Fig. 4.4. The correction scales the jet energy response for $|\eta| > 0.6$ to the jet energy response for $0.2 < |\eta| < 0.6$, where the calorimeter is well understood and calibrated. With this correction the jet energy response is uniform in η.

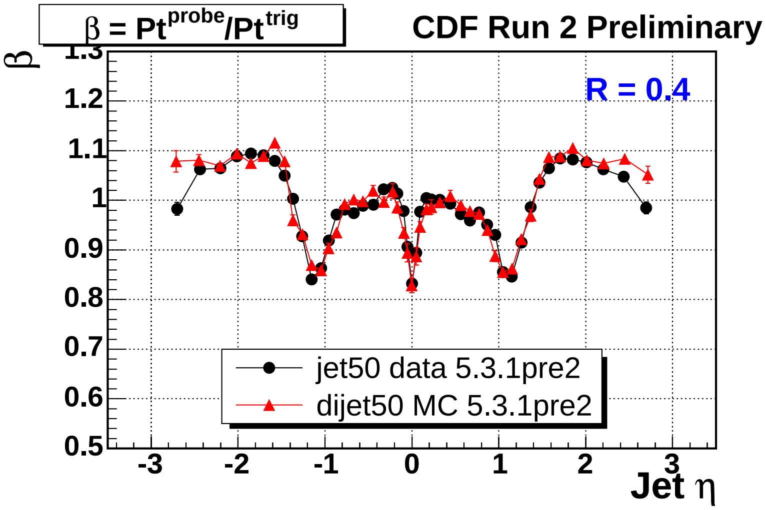

Figure 4.4: The correction factor (β) is shown as a function of the pseudorapidity, η, for a jet cone size of 0.4. Here β is a ratio of the calorimeter response for jets in the $|\eta| > 0.6$ (probe jet) region to the response for jets with $0.2 < |\eta| < 0.6$ (trigger jet). Corrections extracted from a simulated PYTHIA dijet MC sample agree with the corrections as extracted from a real dijet event sample.

- **L4 - Multiple Interactions (C_{MI}):** In a high luminosity data sample, multiple $p\bar{p}$ interactions occur in the same bunch crossing. In these events, the particles from different $p\bar{p}$ collisions can be sneaked into the same jet cluster (pile-up), resulting in a higher jet energy. The increase in the jet E_T is studied by measuring E_T of the random jets in minimum bias events. The pile up energy per jet is shown in the Fig. 4.5 as a function of the primary number of vertices in the event. The averaged additional energy is subtracted from the measured jet energy according to the primary number of vertices in the events.

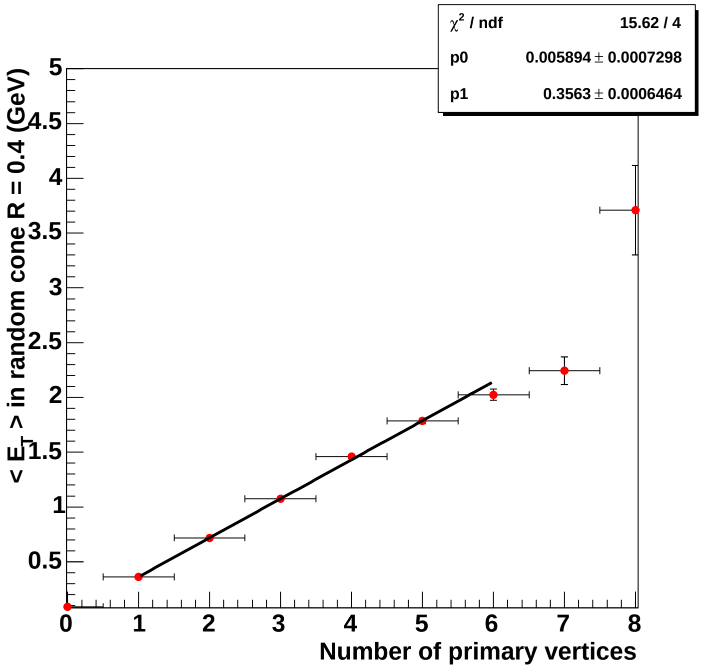

Figure 4.5: The average transverse energy of random jets (with a cone size of 0.4) in minimum bias events as a function of the number of primary vertices.

- **L5 - Absolute Energy Scale (C_{ABS}):** The absolute correction scales the calorimeter jet energy to the particle jet energy. These two jets energies are not equal because of the non-linear response of the calorimeter. The correction is obtained by mapping the total p_T of the particle jet to the p_T of the calorimeter jet using MC sample. This correction depends on the particle multiplicity and on the p_T spectrum of particles inside the jet. Therefore, reliable modeling of the fragmentation of partons to hadrons and of the detector's non-linear response to individual particles is crucial.

Figure. 4.6 shows the absolute energy scale correction, $\frac{p_T{}^{\text{particle jet}}}{p_T{}^{\text{calorimeter jet}}}$, as a function of jet p_T.

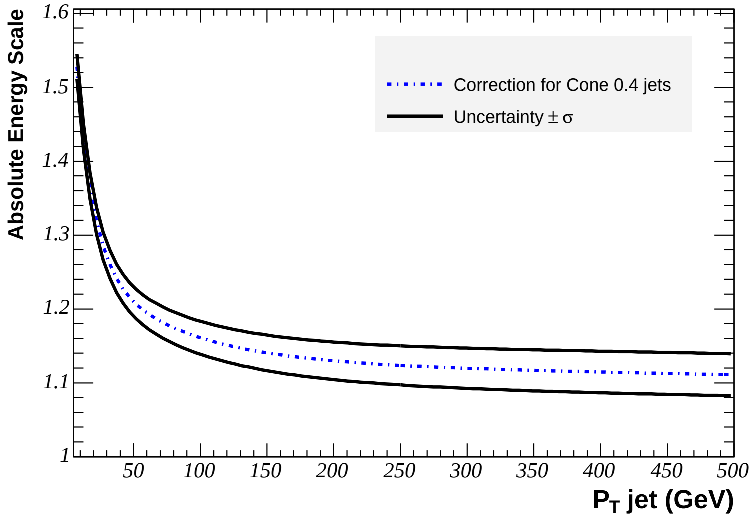

Figure 4.6: The absolute energy scale correction as a function of jet p_T.

- **L6 - Underlying Event Energy ($\mathbf{C_{UE}}$):** In $p\bar{p}$ collisions, the partons which are not involved in the hard collision (e.g. $t\bar{t}$ creation) are called spectator partons. These partons also recombine and form hadrons or jets which deposit energy in the calorimeter. This energy is called the underlying event energy. As is the case for events in the same bunch crossings with multiple interactions, the particle energy in the underlying event is sometimes included in the jet cluster energy and should be subtracted. The underlying event energy is extracted from a sample of minimum bias events including only one vertex. Figure 4.7 shows the fractional correction uncertainty resulting from the subtraction of the underlying event energy as a function of jet p_T.

- **L7 - Out of Cone Energy ($\mathbf{C_{OOC}}$):** The jet clustering cone cannot contain all the particles decayed from the initial parton due to the fixed cone size. We estimate the energy loss due to the particles out of the cone by investigating the energy flow from initial parent parton to particle

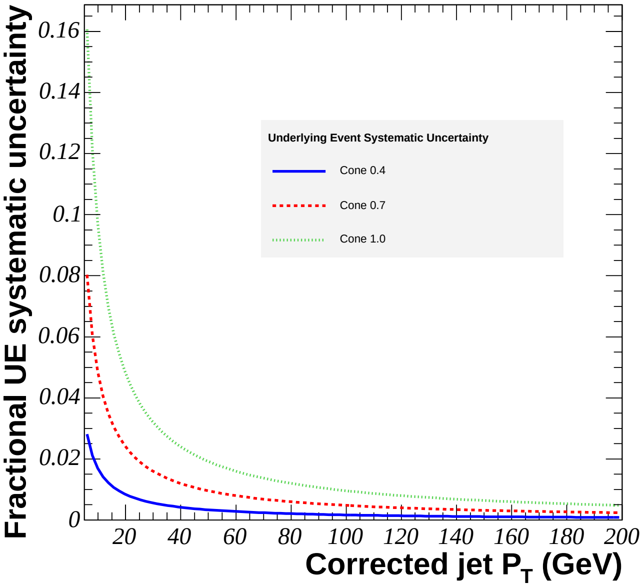

Figure 4.7: Fractional uncertainty from the underlying event as a function of the jet p_T.

jet in the PYTHIA MC dijet samples. Figure 4.8 shows the out of cone correction as a function of the particle jet p_T.

- **L8 - Splash-out Uncertainty:** The systematic uncertainty in the out of cone correction is measured by investigating jet energies for cone sizes varying from 0.4 to 1.3. The splash-out uncertainty accounts for the additional uncertainty in the energy leakage beyond a cone size of 1.3.

Additional details on jet energy corrections can be found in reference [67]. Each correction brings associated systematic uncertainty. The individual uncertainties are combined, and used for a total systematic uncertainty in the jet E_T correction. The total systematic uncertainty is shown as a function of the jet E_T in Fig. 4.9.

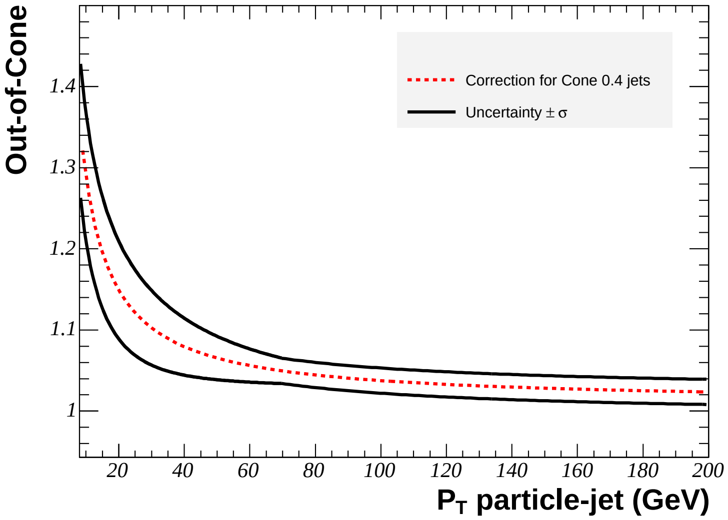

Figure 4.8: Out of cone correction as a function of particle jet p_T.

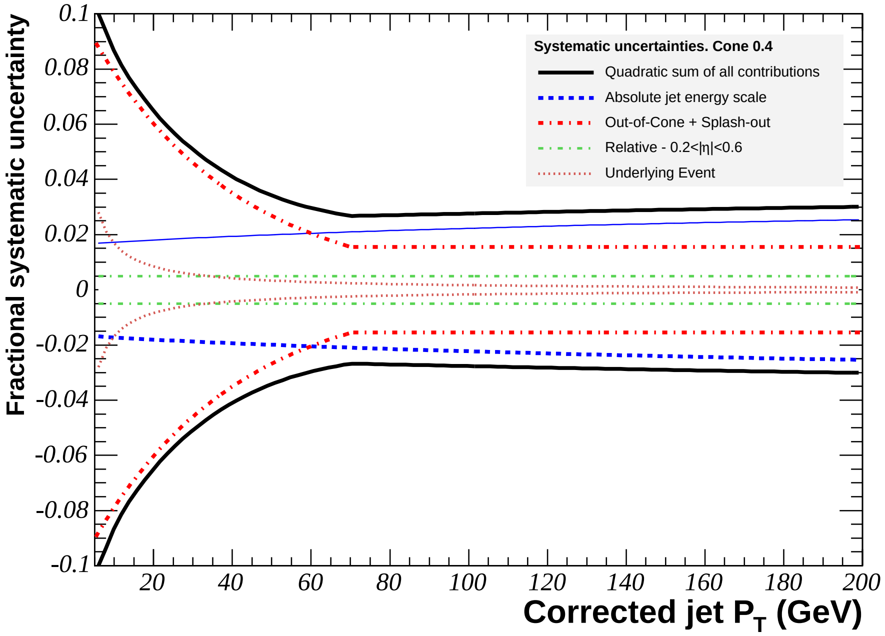

Figure 4.9: The total systematic uncertainty arising from all jet energy corrections.

Secondary Vertex Tagging Algorithm

Many of the hadronic jets in $t\bar{t}$ events include b-hadrons originating from a b-quark. The lifetime of b-hadrons is several ps[5]. Therefore b-hadrons travel hundreds of μm in the detector before decaying into charged and neutral daughter particles. A common origin of the decay daughter particles is referred to as a secondary vertex (SecVtx); the SecVtx is traced by reconstructing all the charged particle tracks in a jet. An algorithm to find a SecVtx is described below. More details about this algorithm can be found in reference [70].

1. First, a primary vertex is determined by the vertex which is nearest to the high p_T lepton. The spatial resolution of the vertex is of order 10-20 μm.

2. Each jet is examined whether it includes good silicon tracks which can reconstruct a SecVtx. Jets with at least two good silicon tracks are defined as "taggable" jets.

3. The secondary vertex is reconstructed using two paths: (1) at least three good silicon tracks with impact parameter significance of $d_0/\sigma_{d_0} > 2.5$, and all tracks carrying $p_T > 0.5$ GeV/c including at least one track with $p_T > 1.0$ GeV/c, or (2) a two-track vertex with $d_0/\sigma_{d_0} > 3.0$, and both tracks with $p_T > 1.0$ GeV/c including at least one of the tracks carrying $p_T > 1.5$ GeV/c.

4. The distance between the primary and secondary vertices in the transverse $(r-\phi)$ plane is defined as

$$L_{2D} = (\vec{r}_{SV} - \vec{r}_{PV}) \cdot \hat{p_{jet}}, \tag{4.5}$$

   where $\vec{r}_{PV}$ is the position of the primary vertex, $\vec{r}_{SV}$ is the position of the secondary vertex, and $\hat{p_{jet}}$ is the jet direction. Here L_{2D} is the two-dimensional decay length in the transverse plane. The secondary vertex with significance $|L_{2D}/\sigma_{L_{2D}}| > 3.0$ is considered "displaced", and the jet containing such a displaced vertex is considered to be SecVtx "tagged".

---

[5] pico seconds, ps $= 10^{-12}$ s.

The sign of $|L_{2D}|$ is determined by the jet direction relative to the vector pointing from the primary vertex to the secondary vertex. If they are aligned in same direction, the jet is *positively tagged*. If the decay length is negative (the secondary vertex is behind the primary vertex), the jet is called *negatively tagged*. The negative tags are caused by mismeasured tracks due to the tracking resolution.

The secondary vertex originating from a real heavy flavor quark (b or c) decays is positively tagged. However, due to the tracking resolution the light quark-jets can have false positive tags (*mistags*) as well as the negative tags. In order to estimate mistags, we reconstruct a mistag matrix exploiting the negative $L_{2D}/\sigma_{L_{2D}}$ distribution [71]. The mistag matrix provides a probability that a light quark-jet is positively tagged as a function of jet variables: the variables are jet E_T, the number of tracks in the jet, jet η, jet ϕ, and the total scalar sum of the E_T of all the jets.

The b-tagging efficiency is measured using both data and dijet PYTHIA MC simulation samples in which jets contain a low p_T soft electron or a muon. The requirement of a low p_T lepton enriches the heavy flavor quark component in the sample. A loose (or tight) b-tagging criterion requires loose (or tight) track quality requirements. The mistag rate depends on the jet E_T as shown in Fig. 4.10 [72].

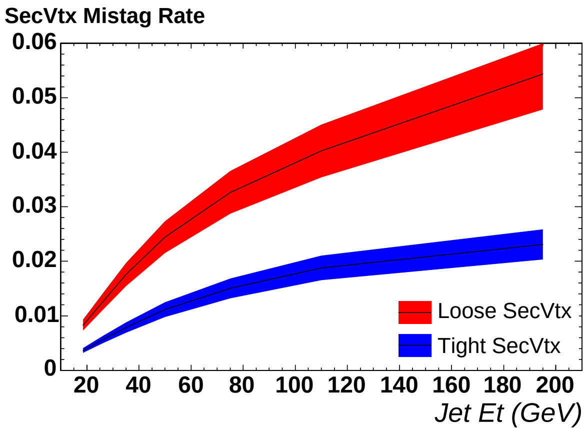

Figure 4.10: Mistag rate as a function of jet E_T for loose and tight SecVtx tags.

Figure 4.11 shows the SecVtx tagging efficiencies determined from MC samples. The difference in the b-tagging efficiencies between the MC sample and data is parametrized by a $scale\ factor = \frac{\epsilon_{\mathrm{DATA}}}{\epsilon_{\mathrm{MC}}}$, which is applied to the simulation samples as a correction. Combining the scale factors (SF) measured from the low p_T electron and muon samples, we use a global SF:

$$\begin{aligned} \mathrm{SF} &= 0.95 \pm 0.01(stat) \pm 0.05(syst)\ \text{(loose)} \\ \mathrm{SF} &= 0.95 \pm 0.01(stat) \pm 0.04(syst)\ \text{(tight)}. \end{aligned} \tag{4.6}$$

The uncertainty includes the p_T and η dependences of the SF. Additional details on the SecVtx b-tagging can be found in reference [71].

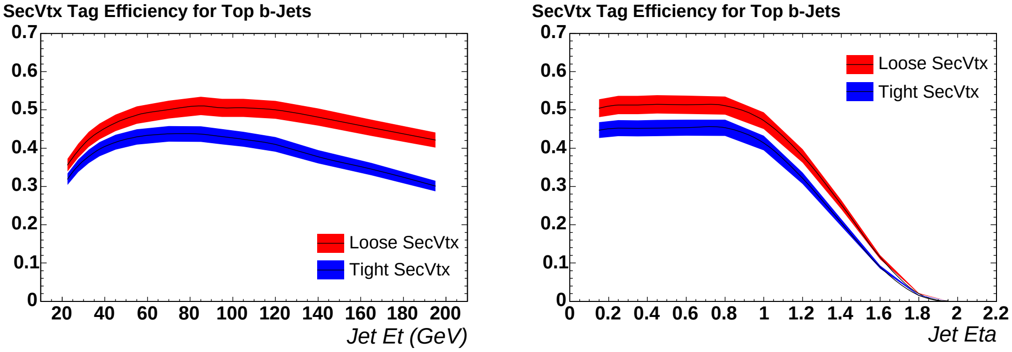

Figure 4.11: Secondary Vertex b-tagging efficiencies as a function of jet E_T (left) and pseudorapidity (right). The loose (tight) SecVtx tagging results in a higher (lower) efficiency for b-tagging.

As mentioned earlier in this chapter, we require two SecVtx b-tagged jets. This requirement of two b-jets is very useful to suppress the non-$t\bar{t}$ SM backgrounds as shown in Table 4.6. For more efficient event selection, we use the loose b-tagging criterion in this analysis.

4.2.4 Missing Transverse Energy

The lepton+jets $t\bar{t}$ final state includes one neutrino which penetrates the detector without interaction. The neutrino energy is deduced only from the energy-momentum conservation. In Tevatron, there is no net transverse energy in the initial head-on proton-antiproton collisions. Therefore, an imbalance in the sum of the measured energies in the transverse plane implies the transverse energy carried by neutrino as given by

$$\not{E}_T = -\sum_{i}^{n} \vec{E^i} \cdot \hat{\rho}_i, \tag{4.7}$$

where $\vec{E^i}$ is the energy deposit in the i^{th} calorimeter tower with the tower position, and $\hat{\rho}_i$ is a radial unit vector in the transverse plane. The longitudinal component of the neutrino energy is unknown because the initial longitudinal momentum fractions of the interacting partons in the proton and antiproton are not constrained.

The determination of the missing transverse energy ($\not{E}_T$) requires a couple of corrections to the initial estimate of $\not{E}_T$ from calorimeter energies. These corrections are applied on an event by event basis. The first correction is for the undetected energy from the final state muons. Muons deposit only a small fraction of their energy in the calorimeter. Therefore, the muon energy is accounted by using the muon track momentum. The second correction originates from jet energy corrections as described in the previous Sec. 4.2.3. The missing transverse energy is recalculated after all jet energies are corrected and the muon energies are properly accounted for.

4.3 Acceptances

The selection acceptances of SM $t\bar{t}$ and Higgs signal events are estimated using the PYTHIA MC samples. The acceptance ($\mathcal{A}$) is defined as

$$\mathcal{A} = \frac{N_{\text{selected}}}{\sigma_{t\bar{t}} \times \mathcal{L}_{\text{int}} \times \epsilon}, \tag{4.8}$$

where N_{selected} is the number of events which pass all selection criteria. The combined efficiency (ϵ) includes all the efficiencies and scale factors for the lepton identification, the lepton track reconstruction, and the primary vertex requirements as well as the b-tagging scale factor. We use CDF II data with an integrated luminosity ($\mathcal{L}_{\mathrm{int}}$) of 2.2 fb^{-1}. The $t\bar{t}$ cross section ($\sigma_{t\bar{t}}$) is assumed to be 6.7 pb for the top quark mass of 175 GeV/c^2. The fully corrected acceptances are summarized in Table 4.4. A possible bias from using positive charged Higgs MC samples is negligible as verified with a negatively charged Higgs sample (H^-) for m_{H^+} of 120 GeV/c^2.

m_{H^+} (GeV/c^2)	Acceptance (%)
standard $t\bar{t}$ (W$^\pm$)	2.319 ± 0.189(stat.) ± 0.198(syst.)
60 (H^+)	2.145 ± 0.272(stat.) ± 0.286(syst.)
70 (H^+)	2.250 ± 0.285(stat.) ± 0.283(syst.)
90 (H^+)	2.397 ± 0.302(stat.) ± 0.298(syst.)
100 (H^+)	2.424 ± 0.305(stat.) ± 0.297(syst.)
110 (H^+)	2.432 ± 0.306(stat.) ± 0.295(syst.)
120 (H^+)	2.358 ± 0.291(stat.)± 0.280(syst.)
120 (H^-)	2.363 ± 0.298(stat.)
130 (H^+)	2.163 ± 0.274(stat.)± 0.266(syst.)
140 (H^+)	1.767 ± 0.226(stat.)± 0.223(syst.)
150 (H^+)	1.262 ± 0.164(stat.)± 0.176(syst.)

Table 4.4: Acceptance after efficiency corrections per lepton type.

We use the inclusive SM $t\bar{t}$ MC sample with all W branching ratios turn on while the charged Higgs MC samples has only exclusive decays of $t\bar{t}$ as described in Sec. 4.1.2. The acceptance of the SM $t\bar{t}$ ($W^\pm$) in the Table. 4.4 is re-calculated for the exclusive case just to compare with the acceptances of the charged Higgs samples. In the inclusive $t\bar{t}$ sample, only 1.04% of events pass the lepton+jets selection criteria, and these events includes the events from other $t\bar{t}$ decay channels. A check on the generator level information indicates that a total 12% of the selected events originate from other $t\bar{t}$ channel: 10% from the tauonic channel, and 2% from either di-lepton or all-hadronic channels.

The acceptance of H^+ events decreases as m_{H^+} increases due to the truncated p_T spectrum of a b-jet decayed with the H^+ boson from a top quark. Since heavier charged Higgs carries more energy from the top quark, the accompanied b-quark is used to be softer. Figure 4.12 shows the generated p_T spectrum of b-quarks in $t\bar{t}$ events: (left) b-quark decayed with a leptonic W boson and (right) the other

b-quark decayed with a hadronic boson, W boson or charged Higgs boson with a mass ranging from 60 to 150 GeV/c^2. Unlike the leptonic side b-quark shows consistent p_T spectrum, a larger fraction of the hadronic side b-quark fails to pass the minimum jet E_T ($E_T > 20$ GeV), thus resulting in a lower acceptance.

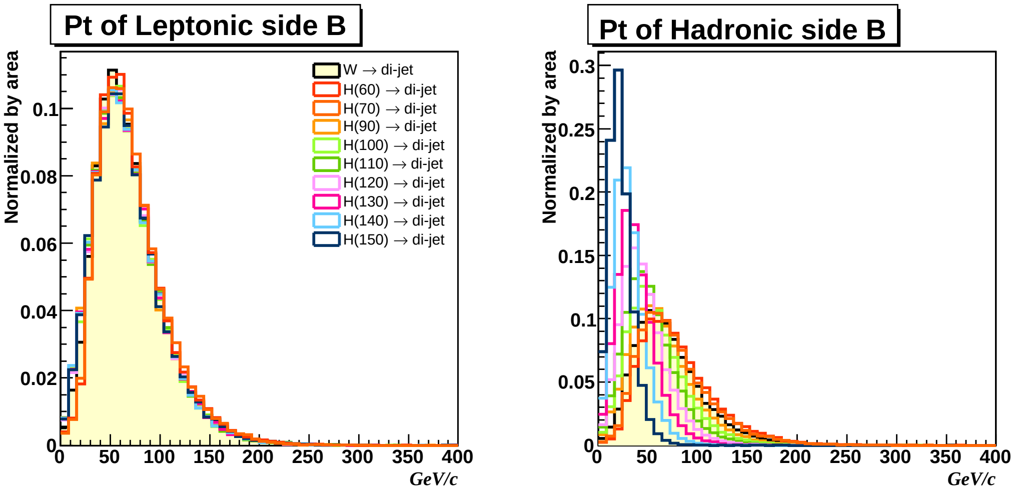

Figure 4.12: The generated p_T spectrum for b-quarks in $t\bar{t}$ events: p_T of b-quarks decays with a leptonic W boson (left) and p_T of b-quarks decays with hadronic boson (right). Higgs samples with m_{H^+} ranging from 60 to 150 GeV/c^2 shown in colored lines, and the SM $t\bar{t}$ sample shown in filled distribution.

4.4 Background

This section estimates the events from non-$t\bar{t}$ processes (non-$t\bar{t}$ backgrounds) in the selected lepton+jets $t\bar{t}$ candidates. The non-$t\bar{t}$ backgrounds originate from several sources including W+jets, non-W (QCD), $Z(\rightarrow \tau^+\tau^-)$+jets, dibosons, and single top production. We use a combination of data and MC samples to determine the composition and the level of the backgrounds.

The selected $t\bar{t}$ data sample before requiring two b-jets is called the *pretag* sample (N^{pretag}). The composition of the pretag sample is assumed to be

$$N^{pretag}_{W+jets} = N^{pretag} \cdot (1 - F^{pretag}_{non-W}) - N^{pretag}_{single\ top} - N^{pretag}_{diboson} - N^{pretag}_{Z+LF} - N^{pretag}_{t\bar{t}}, \quad (4.9)$$

where $F^{pretag}_{\text{non}-W}$ is the non-W fraction in the sample. The other terms refer to as various background sources. The numbers of SM $t\bar{t}$, diboson, Z+light flavor (LF) jets, and single top events are estimated from each MC sample with well predicted production cross sections. We assume that only W+jets events remain in the pretag sample after subtracting these expectations. Later, each number of non-$t\bar{t}$ background in the pretag sample is scaled to the two b-jets sample by applying the b-tagging (and mistag) efficiency. A detailed description of the estimate of the non-$t\bar{t}$ backgrounds is given in references [71] [73]. A short summary of the various components is given below.

Non-W (QCD) Background

The requirement of a high p_T lepton and large $\not{E}_T$ discriminates against events in which no W boson is produced. However, it is possible that the W signature is faked. Sources of fake W bosons include conversion electrons or secondary leptons in decays of heavy quark with a $\not{E}_T$ due to mismeasured jet energies. These events are categorized as "non-W" processes. Since these fake W backgrounds originate from multijet processes, they are also referred to as "QCD background".

The non-W (QCD) fraction ($F_{\text{non}-W}$) in Eqn. 4.9 is determined by fitting the $\not{E}_T$ distribution of data to a sum of templates from various sources as shown in Fig. 4.13. The $\not{E}_T$ templates are obtained from the MC samples, except for the non-W background. The non-W background template is extracted from the anti-electron data sample; the data sample is collected by requiring an electron-like object which fail to pass a few central electron identification cuts (Table 4.2). The expected number of non-W background events is given by

$$N^{pretag}_{non-W} = F^{pretag}_{non-W} \cdot N^{pretag}. \tag{4.10}$$

W+Multijet Background

The dominant non-$t\bar{t}$ background is W boson production associated with multijets. Since one real W boson is included in this process, W+multijet background events have the same final state with the genuine $t\bar{t}$ events. The W+jets contribution is more significant in the b-tagged sample because W+heavy flavor (HF) jets (from b-quark or c-quark) yield positive SecVtx tags as is the case for SM lepton+jets $t\bar{t}$ events. The W+light flavor (LF) jets (from u, d, and s quarks or gluons) can be remained in the two b-jets requirement if a light flavor jet has a positive SecVtx jet as discussed in Sec. 4.2.3. We refer to the contribution from W+LF jets as the mistag background. Since the acceptance of the W+jets background depends on the jet flavor, we estimate W+HF jets and W+LF jets backgrounds separately.

The W+jets events are modeled by ALPGEN [74] MC event generator, which incorporates exact leading-order matrix elements, and by PYTHIA for the simulation of parton showering and hadronization. However, the production rate for the W+jets process is not well known because of a large theoretical uncertainty; this uncertainty originates from the large next-to-leading order (NLO) corrections to the leading order (LO) calculation. Hence the normalization for these backgrounds is determined directly from the data, while the kinematic distribution of W+jets events is obtained from the MC simulation.

W+Heavy Flavor Jets include W bosons associated with at least one heavy quark, i.e. $Wb\bar{b}$, $Wc\bar{c}$, and Wc. Contributions from these backgrounds are calculated from following expression:

$$N^{tag}_{W+HF} = N^{pretag}_{W+jets} \cdot F_{HF} \cdot K \cdot \epsilon_{tag} \tag{4.11}$$

Here, F_{HF} is the fraction of HF jets in the inclusive W+jets data, which is derived from identifying the generator level information of the ALPGEN MC:

$$F_{HF} = \frac{N^{W+jets}_{b,MC}}{N^{W+jets}_{j,MC}}.$$

Then, K factor accounts for the data/MC difference of the F_{HF} [75] as given by:

$$K = \frac{F^{data}_{HF}}{F^{MC}_{HF}}.$$

The F_{HF}^{data} is estimated by using SecVtx tagging information in the jet data samples. The tagging efficiency (ϵ_{tag}) and F_{HF} are calculated for $Wb\bar{b}$, $Wc\bar{c}$, and Wc samples, separately. Then, those factors are applied for the each background estimate in the selected $t\bar{t}$ events.

W+Light Flavor Jets is the largest background in the pretag sample. However, the two b-jets requirement significantly reduces the level of the W+LF background. The number of W+LF (mistag) background is estimated by applying the mistag matrix (Sec. 4.2.3) as given by

$$N_{W+LF}^{tag} = N_{W+jets}^{pretag} \cdot \frac{N_{-}}{N_{jet}}. \tag{4.12}$$

The mistag rate of LF jets ($\frac{N_{-}}{N_{jet}}$) is driven by the large jet data sample (N_{jet}), which is dominated by the LF jets. Assuming a symmetry between negative and positive tags in the sample, the mistag rate is calculated by integrating the negative jet tagging probability in the entire jet data (N_{-}). The two b-jets requirement suppresses the W+LF background by a factor of 5×10^{-3}.

Other SM Processes

Additional minor sources of non-$t\bar{t}$ backgrounds include diboson production (WW, WZ, and ZZ), $Z(\rightarrow \tau^{+}\tau^{-})$+LF jets, and single top production. Here, diboson and Z bosons associated with jets can fake a $t\bar{t}$ signal when one boson or τ decays leptonically and the other one decays hadronically. The $t\bar{b}(\rightarrow Wb\bar{b})$ final state in the single top process can also fake a $t\bar{t}$ signal when additional jets are present.

These backgrounds are estimated directly from the MC samples, assuming that the theoretical cross sections for the processes are well known and the final state is properly simulated. Single top quark events are generated with the MadEvent [76] program, and the $Z(\rightarrow \tau^{+}\tau^{-})$+LF sample is generated using the ALPGEN program. The PYTHIA MC parton showering and the CDF II detector simulation are used for both samples. Diboson samples are fully simulated using the PYTHIA MC program. The acceptances and tagging efficiencies of these backgrounds are determined as is done for the SM $t\bar{t}$ event.

Total Backgrounds

The number of $t\bar{t}$ and non-$t\bar{t}$ processes in the *pretag* sample are listed in Table 4.5. The prediction of backgrounds are estimated for the first 2.0 fb^{-1} data, and then scaled to include last 0.2 fb^{-1}. The total SM prediction in the pretag events agrees with the observed number of events in the 2.2 fb^{-1} data.

Process	Entries
diboson ($WW/ZZ/WZ$) ($N^{pretag}_{diboson}$)	49.8 ± 3.8
single Top ($N^{pretag}_{singletop}$)	9.2 ± 0.8
$Z(\to \tau^+\tau^-$ + LF(N^{pretag}_{Z+LF})	45.8 ± 4.2
W + HF (N^{pretag}_{W+HF})	180.6 ± 60.8
W + LF (N^{pretag}_{W+LF})	546.6 ± 144.7
non-W (N^{pretag}_{non-W})	223.0 ± 85.9
non-$t\bar{t}$	1055.0 ± 300.2
$t\bar{t}$ (6.7 pb)	634.1 ± 81.4
Total Prediction	1689.1 ± 381.6
Selected pretag sample	1708

Table 4.5: Number of SM processes in the 2.2 fb^{-1} pretag sample.

The prediction of SM processes with two b-jets requirement is obtained by multiplying the b-tagging efficiency (or mistag rates) and scale factor to the pretag samples. Table 4.6 summarizes the estimates of SM $t\bar{t}$ events and the various backgrounds in the two b-jets data sample of 2.2 fb^{-1}. In the table, the observed number of events is larger than the total SM expectation. Since the non-$t\bar{t}$ backgrounds are very suppressed by the two b-jets requirement, the biggest source of the difference is expected to be from the uncertainty between the assumed $t\bar{t}$ production cross section ($\sigma_{t\bar{t}} = 6.7$ pb) and the true cross section. The number of non-$t\bar{t}$ background events is known to be nearly independent of the $t\bar{t}$ cross section as studied in the reference [77].

4.5 Data Validation

In order to validate modeling of the SM processes, we compare the kinematic distributions of the SM simulation samples with observed distributions in the pretag

Process	$\geq$ 4 tight jets	fraction
diboson (WW/ZZ/WZ)	0.71 ± 0.11	0.4%
single Top	1.84 ± 0.24	1.1%
$Z(\rightarrow \tau^+\tau^-)$+LF	0.48 ± 0.07	0.3%
$W + b\bar{b}$	5.58 ± 2.31	3.4%
$W + c\bar{c}/W + c$	1.87 ± 0.80	1.1%
W +LF(mistags)	1.86 ± 0.63	1.1%
non-W	1.58 ± 3.3	0.9%
non-$t\bar{t}$	13.92 ± 7.49	8.4%
$t\bar{t}$ (6.7pb)	152.59 ± 24.95	91.6%
Total Prediction	166.51 ± 32.44	100%
Observed	200	

Table 4.6: Expected and observed number of events in the 2.2 fb^{-1} data sample including two b-jets.

sample. Unlike other backgrounds use the kinematic distributions from the MC sample, the non-W background distribution is obtained from the anti-electron data sample. Each background distribution is normalized by the background estimate in Table 4.5.

Figures 4.13 - 4.15 show the validation plots of final state objects in the pretag sample: Sum E_T ($= \sum_i E_{Ti}$, scalar E_T sum of all final state jets including $\not\!\!E_T$) and $\not\!\!E_T$ in 4.13, E_T of the leading four jets in 4.14, and the distributions of lepton p_T and E_T of the fifth energetic jet in 4.15. The fifth energetic jet is specifically used later in Sec. 5.2.1.

Figures 4.16 and 4.17 validate the kinematic distributions in the selected $t\bar{t}$ sample after requiring two SecVtx tagged jets. These plots include the distributions of the E_T of leading four jets, $\not\!\!E_T$, and Sum E_T. The normalizations of the SM processes ($t\bar{t}$ and non-$t\bar{t}$ backgrounds) are obtained using a binned likelihood fit to the observed dijet mass distribution (Sec. 5.3.3), rather than using the background estimates in Table 4.6, due to the discrepancy between the observed and expected number of events.

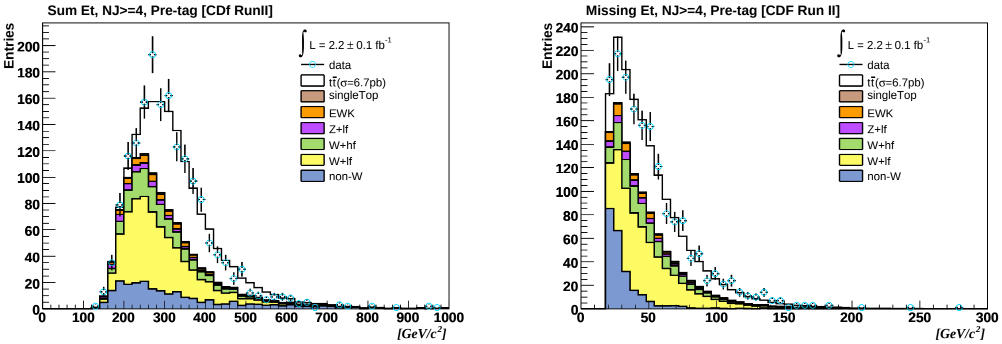

Figure 4.13: A comparison of data (crosses) with the SM expectations (filled, on top of each other) for the Sum E_T (left) and for the $\not{E}_T$ distribution (right) in pretag $t\bar{t}$ sample.

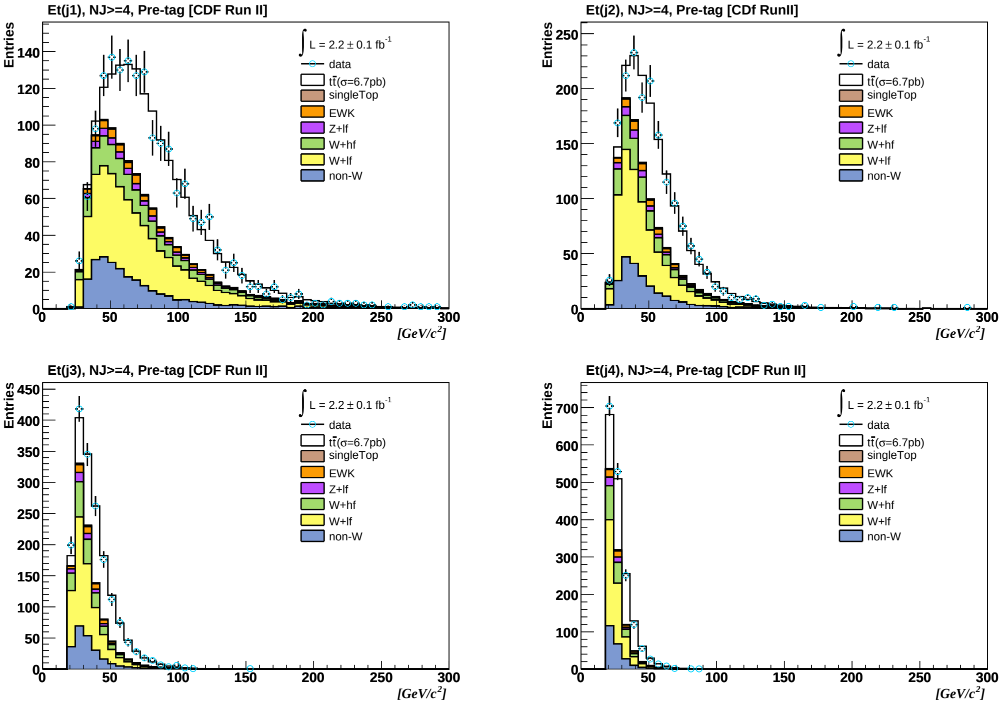

Figure 4.14: A comparison of the E_T spectrum of the leading four jets in $t\bar{t}$ events between data (crosses) and the SM expectations (filled, on top of each other) in pretag $t\bar{t}$ sample.

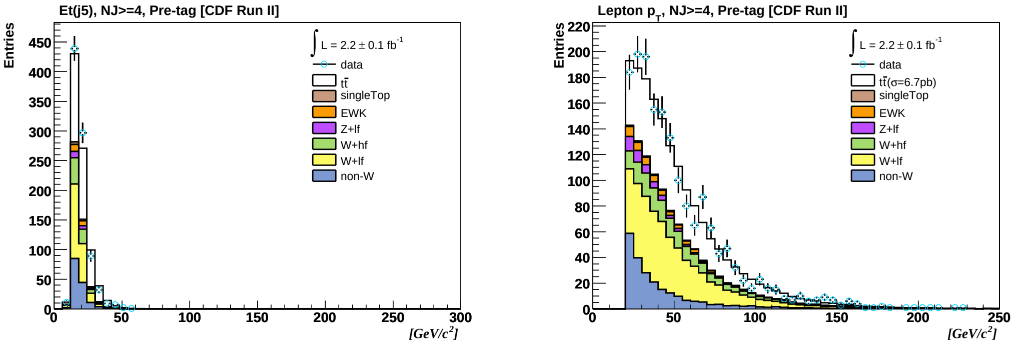

Figure 4.15: Validation plots for E_T of the 5^{th} jet (left) and the lepton p_T (right) in the pretag $t\bar{t}$ sample.

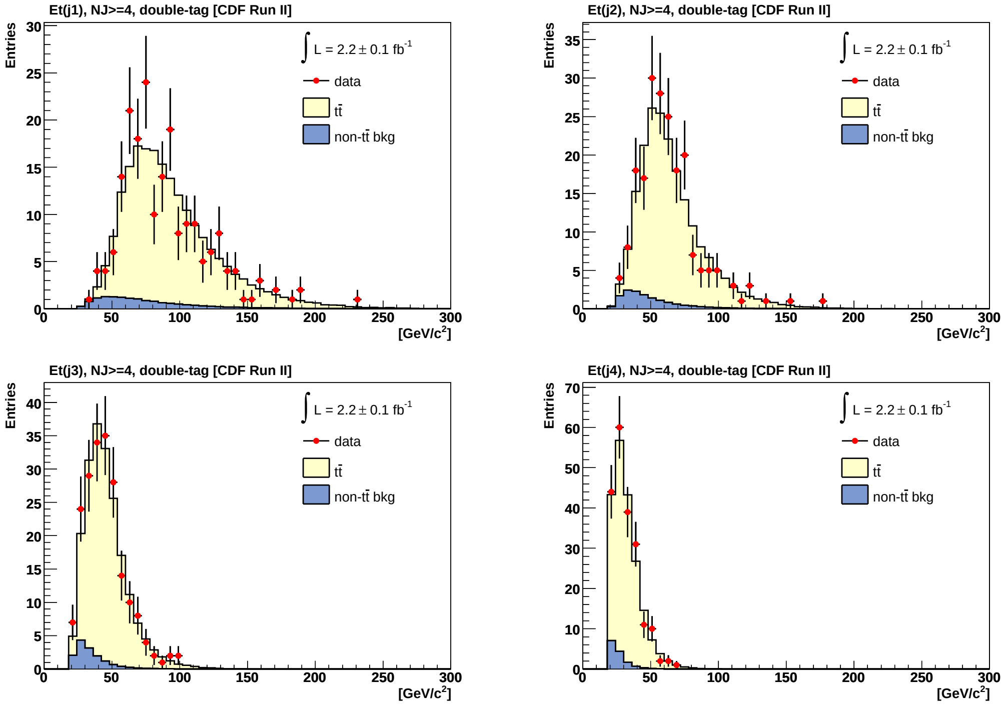

Figure 4.16: E_T spectrum of the leading four jets between data (crosses) and the SM expectations (filled, on top of each other) in $t\bar{t}$ events after two b-jets requirement.

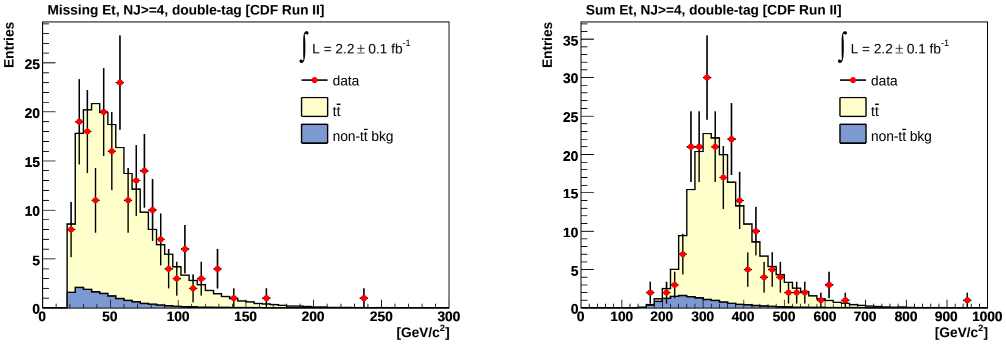

Figure 4.17: Validation plots for $\not\!\!E_T$ (left) and sum E_T (right) in $t\bar{t}$ events after two b-jets requirement.

Chapter 5

Analysis

This chapter describes studies of improvements to the charged Higgs mass reconstruction using two jets in top quark decays. We use a binned likelihood fit to the dijet mass spectrum to extract the contribution from charged Higgs bosons. Using the likelihood fit results, we estimate the upper limits on the branching ratio $\mathcal{B}(\mathrm{t} \rightarrow \mathrm{H}^{+}\mathrm{b})$ for a null-Higgs hypothesis in SM.

5.1 Dijet Mass Reconstruction

In the selected lepton+jets $t\bar{t}$ events, the hadronic boson is reconstructed using two jets. The invariant mass of the dijet reflects which boson is produced from the top quarks, therefore having a good mass resolution is important to distinguish H^{+} bosons against the W bosons in the SM $t\bar{t}$ events. The mass resolution can be improved if we reconstruct the $t\bar{t}$ pair as a whole.

A $t\bar{t}$ event is fully reconstructed in a kinematic fit using the selected final state objects: a lepton, $\not{E}_T$, and four leading jets with energies corrected up to L5 (Sec. 4.2). This kinematic fitter was developed for the template-based precision measurement of the top quark mass in CDF Run I [78]. Here, the fitter is modified for the charged Higgs search in top quark decays. It assigns the selected objects to the tree level $t\bar{t}$ decay particles. The lepton and $\not{E}_T$ are exclusively assigned to the daughter particles of the leptonic W boson. The four most energetic jets are assigned to the two b-quarks (one from each top decay) and two light quarks that originate from the hadronic boson (W or H^+). The assignment is evaluated in a form of χ^2,

$$\begin{aligned}\chi^2 &= \sum_{i=l,4\text{jets}} \frac{(p_T^{i,\text{fit}} - p_T^{i,\text{meas}})^2}{{\sigma_i}^2} + \sum_{j=x,y} \frac{({p_j}^{\text{UE,fit}} - {p_j}^{\text{UE,meas}})^2}{{\sigma_{\text{UE}}}^2} \\ &+ \frac{(M_{l\nu} - M_W)^2}{{\Gamma_W}^2} + \frac{(M_{bl\nu} - M_t)^2}{{\Gamma_t}^2} + \frac{(M_{bjj} - M_t)^2}{{\Gamma_t}^2}. \end{aligned} \tag{5.1}$$

In order to reduce the matching ambiguity, SecVtx tagged jets are assigned to the either b-quarks (b) and the other jets are assigned to the light quarks (j) in the χ^2. Unclustered energy (UE) is sum of all lost energies at the particle level jet reconstruction, i.e. the energies of particles outside of the jet reconstruction cone. The UE is used to correct the neutrino's transverse energy (p_T^ν) as

$$p_T^\nu = -(\sum_{i=l,4\text{jets}}^{4} {p_T}^i + {p_T}^{UE}). \tag{5.2}$$

The χ^2 is minimized by constraining the invariant mass of the lepton and neutrino to be the W mass (80.4 GeV/c^2) and constraining the two top quark decays, $bl\nu$ and bjj, to have the same invariant mass of 175 GeV/c^2. In the process of constraining the W and top quark masses, energies (p^{meas}) of the lepton, the leading jets, and the UE (thereby $\not{E}_T$) are fitted (p^{fit}) within the experimental resolutions (σ). The minimum χ^2 fit is done using the MINUIT program [79]. In the original version of the fitter [78], the χ^2 equation has an extra term which constrains the dijet (jj) to have the invariant mass of the W boson and allows the top mass to float. In this analysis, we constrain the top mass and allow the dijet mass from a hadronic boson to float instead.

Twelve combinations are available for the jet-quark assignments in a lepton+jets $t\bar{t}$ event, and the number of combinations is doubled since each combination has two possible values for the neutrino's longitudinal momentum (See Appendix A). However, the assignment of the b-tagged jets to the b-quarks reduces the number of possible combinations and the probability of wrong jet assignment. In an ideal $t\bar{t}$ event, only two combinations remain for the two b-jets assignment because other two jets are assigned to the same boson. The fitter runs for each combination, and the combination with the smallest χ^2 is used in this analysis.

Top-Specific Corrections

In addition to the generic jet energy corrections (Sec. 4.2.3), a special correction, called top-specific correction, is applied to jets produced in $t\bar{t}$ events. The detector's response to a jet depends on the original quark's flavor because of the different fragmentation and p_T spectra of the hadron components of the jet [78] [80]. If a jet originates from b, c, or s-quark, the jet can involve kaons whose rest mass energies are not measured in the calorimeters. The top-specific correction adjusts the measured jet energy according to the flavor of the parton assigned to the jet; this is referred to as a flavor-dependent correction. The top-specific correction is estimated using a detector response function to a jet defined as:

$$\text{Response} = \frac{p_T(\text{GEN}) - p_T(\text{L5})}{p_T(\text{L5})} = \frac{p_T(\text{GEN})}{p_T(\text{L5})} - 1. \tag{5.3}$$

Figure 5.1 compares the response to b-jets and light quark-jets in PYTHIA $t\bar{t}$ Monte Carlo (MC) sample. The response is parameterized as a function of input jet p_T:

$$\text{Response} = e^{A+B\cdot p_T} + C, \tag{5.4}$$

where A, B, and C are fit parameters. The jet energy resolution (σ_i) is determined along with the flavor dependent correction and used in the χ^2 kinematic fitter.

Dijet Invariant Mass Distribution

Improvement of the dijet invariant mass by the energy corrections is shown in Fig. 5.2(a) for a 120 GeV/c^2 MC Higgs sample. The reconstructed mass using raw calorimeter jets has a lower mean value due to lost energies which are not accounted for in the jet reconstruction. The dijet mass using fully corrected jet energies, including the top-specific corrections, is closer to the true mass. Then, the mass resolution is greatly improved by incorporating adjustments from the

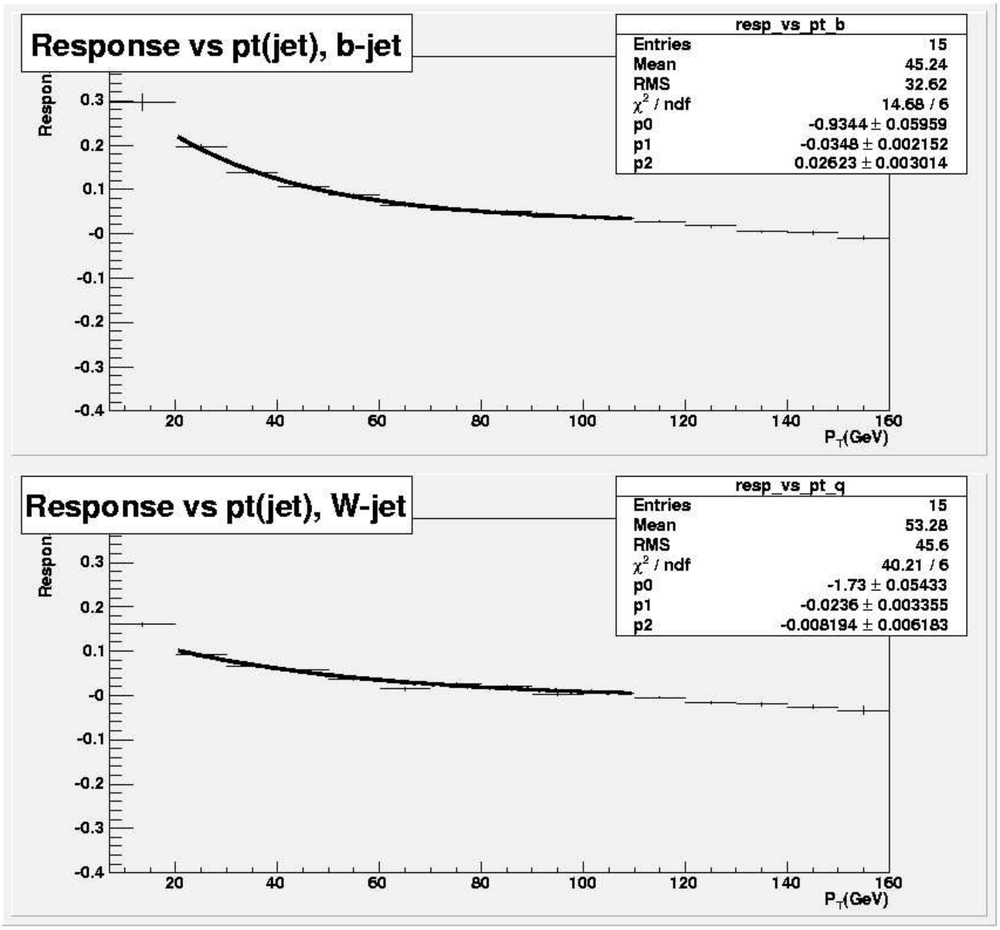

Figure 5.1: Top-specific corrections for b-jets (top) and for light quark-jets from W decays (bottom).

top quark mass constraints in the fitter. To make a clear comparison between the correction levels, we use clean $t\bar{t}$ events having well identified Higgs jets. Figure 5.2(b) compares the reconstructed mass of W bosons and 120 GeV/c^2 Higgs bosons without filtering the generator information (as would be the case with real data). The analysis of the MC events shows a broad mass resolution with longer tails for the H^+ boson. This observation motivate further studies to improve the dijet H^+ mass resolution as discussed in the next section.

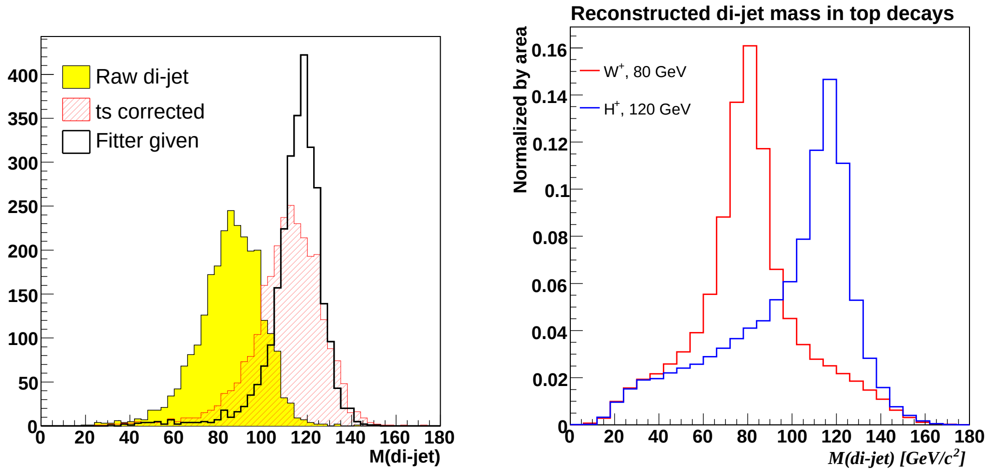

Figure 5.2: (a) Reconstructed dijet invariant mass distribution for 120 GeV/c^2 H^+ MC sample with no jet correction (filled), generic + top-specific corrections (hatched), and fitter corrections from the top mass constraints (solid). (b) Dijet invariant mass from two different sources, H^+ bosons with true mass of 120 GeV/c^2 and W bosons in top quark decays.

5.2 Improvement in the Reconstruction of Dijet Mass

Studies aimed at improving the dijet mass reconstruction were motivated by the m_{H^+} distribution shown in Fig. 5.2(b). The tails in the reconstructed m_{H^+} distribution persist at the very low end of the kinematic boundary and include the W mass region. The tails right below the H^+ mass peak may originate from an energy loss due to a hard QCD gluon radiation in the H^+ decays. Section 5.2.1 describes the improvement in the dijet mass resolution achieved from including an extra final state jet in the reconstruction fit.

Another cause of a wider mass distribution is a possible mis-assignment of a jet to a specific parton. This could originate either from mistakenly selecting hard QCD gluon radiation jets as leading jets in $t\bar{t}$ decays (leading jet contamination), or from a wrong jet-parton assignment in the $t\bar{t}$ reconstruction fit. These sources are discussed in Sec. 5.2.2. Using the generator level information provided in the MC samples, we have developed a special jet identification algorithm which is intensively used in the mass improvement studies. Details of the algorithm are described in Appendix B.

5.2.1 Merging an Extra Jet with the Closest Leading Jet

The low dijet mass tail could originate from energy loss by a hard QCD final state radiation (FSR) in the H^+ decays. In that case, the hard radiation forms an individual final state jet. Figure 5.3 shows the dijet mass distribution in 120 GeV/c^2 H^+ sample for the $t\bar{t}$ events with exact four jets and more than four jets in the final state. The $t\bar{t}$ events used in the plots are required to have four leading jets which are decayed from the four tree level quarks. Comparing the dijet mass reconstructed from two well identified h-jets (magenta colored distribution in Fig. 5.3), the dijet mass distribution is lower and wider in the events with more than four jets than the exact four jets case. The correlation between the worse mass distribution and the number of final state jets implies a real energy loss by a FSR jet. Since almost a half of the MC $t\bar{t}$ events with 120 GeV/c^2 H^+ boson has more than four final state jets, we study the possible improvement in the dijet mass resolution by using the FSR jets.

To recover the energy loss, we involve a fifth (5^{th}) energetic jet in the $t\bar{t}$ reconstruction if the 5^{th} jet has $E_T > 12$ GeV and $|\eta| < 2.4$. The sources of a 5^{th} jet in 120 GeV/c^2 Higgs MC events are identified in Fig. 5.4 using the jet identification algorithm (Appendix B). Our study indicates that the 5^{th} jet is predominantly radiated from either the Higgs decay daughters (i.e. Higgs FSR-jet) or from the incoming quarks, i.e. the Initial State Radiation jet (ISR).

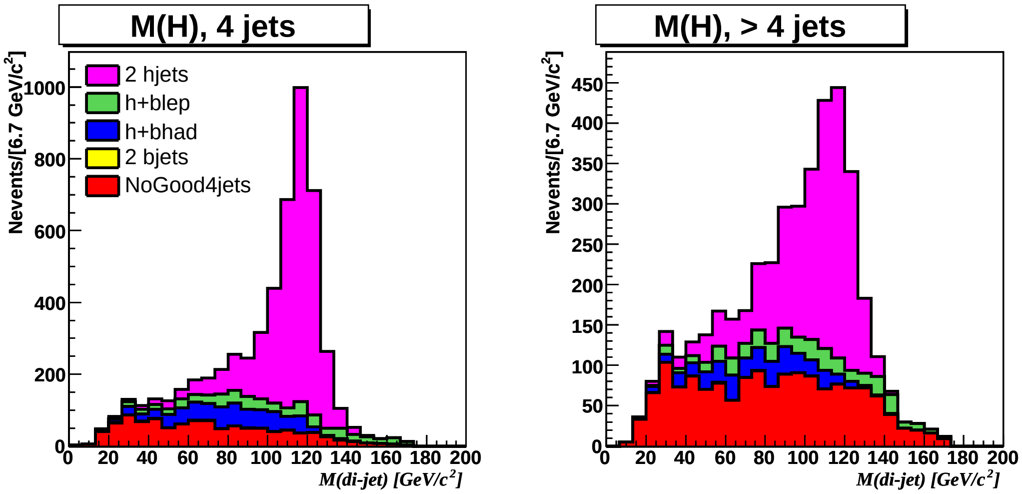

Figure 5.3: Dijet mass in $t\bar{t}$ events with exactly four jets (left) and more than four jets (right) in 120 GeV/c^2 H^+ MC sample. Each color represents combinations of two identified jets: two correct h-jets (magenta), one h-jet and one b-jet (blue and green), two b-jets (yellow), leading jet contamination (red).

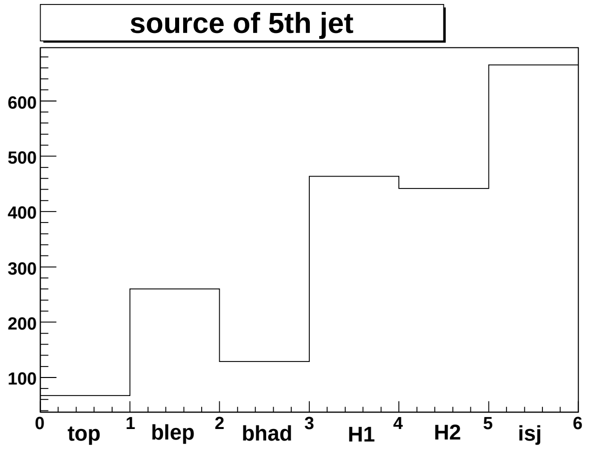

Figure 5.4: Source of a fifth energetic jet in $t\bar{t}$ events with 120 GeV/c^2 H^+. The fifth jet is radiated from top quark (**top**), leptonic/hadronic side b-jet (**blep/bhad**), either h-jet (**H1, H2**), and from the incoming quarks (**isj**).

Here, we look at how the 5^{th} jet is distributed along with the leading jets. The 5^{th} jet from FSR is supposed to be a hard radiation jet from the tree-level parton, thereby close to its mother parton. The distance between jets is calculated by a ΔR $(= \sqrt{(\eta_{\rm jet1} - \eta_{\rm jet2})^2 + (\phi_{\rm jet1} - \phi_{\rm jet2})^2})$. The angular distance between the 5^{th} jet and the closest h-jet or b-jet is compared in two dimensional plot of ΔR (5^{th} jet, h-jet) versus ΔR(5^{th} jet, b-jet) in Fig. 5.5. We see that the 5^{th} jet originating from a Higgs decay has a relatively small angular distance from a h-jet, and is located randomly away from a b-jet (see magenta plot in Fig. 5.5). In the same sense, the 5^{th} jet decayed from a b-quark is closer to the b-jet than the h-jet. If the 5^{th} jet is an ISR jet (green in the Fig. 5.5), the ISR jet is randomly distributed from the closest leading jet.

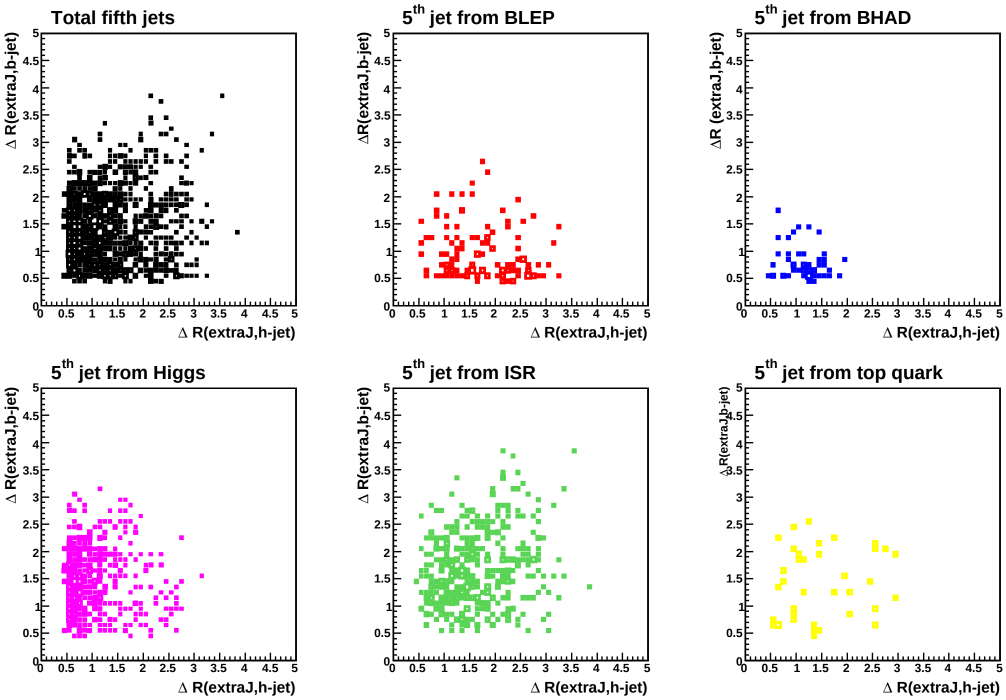

Figure 5.5: Angular distance (ΔR) of the fifth energetic jet to the closest h-jet (x-axis) and to the closest b-jet (y-axis) in the 120 GeV/c^2 H^+ sample. From the top left, plot shows the overall angular distances, and the distances per each source of the 5^{th} jet: leptonic side b-quark (red), hadronic side b-quark (blue), Higgs (magenta), ISR (green), and top quarks (yellow).

In order to recover the energy loss due to the FSR-jet, the 5^{th} jet is merged with the closest leading jet, either a b-jet or a h-jet, when its angular distance (ΔR) is less than 1.0. Otherwise the 5^{th} jet is not used for the analysis. In the 120 GeV/c^2 Higgs sample, with the $\Delta R < 1.0$ requirement, 55% of the Higgs FSR-jets is merged with the Higgs jet, whereas only 17% of ISR jets are incorrectly merged with the Higgs jet. Among the 5^{th} jets, that are selected to be merged with the Higgs boson, 78% of the jets are identified real Higgs FSR jets. Note that the 5^{th} jet merging is performed before the $t\bar{t}$ event reconstruction. As another jet is merged with the leading jet, the energy and direction of the leading jet are revised. In conclusion, the merging process corrects energies of all $t\bar{t}$ decay daughters in the reconstruction fitter.

Both mean and resolution of the dijet invariant mass are improved after merging the 5^{th} jet with the closest leading jet. The mean (RMS) of the dijet mass is improved from 103.3 (21.8) GeV/c^2 to 105.7 (20.8) GeV/c^2 for the 120 GeV/c^2 Higgs bosons, and is improved from 74.76 (16.27) GeV/c^2 to a mean of 75.39 (16.03) GeV/c^2 for the W bosons in SM $t\bar{t}$ MC events. In general, the effect of merging 5^{th} jet is more significant in the higher H^+ samples as shown in Fig. 5.6. The exact values of mean and RMS of those dijet masses are listed in Table 5.1.

m_{H^+} [GeV/c^2]	before merging (mean ± RMS)	after merging (mean ± RMS)
80 (W)	74.8 ± 16.3	75.4 ± 16.0
100	89.5 ± 18.4	90.6 ± 17.7
120	103.3 ± 21.8	105.7 ± 20.8
150	123.1 ± 29.6	127.7 ± 25.8

Table 5.1: Mean and RMS of the dijet mass distribution before and after merging the 5^{th} jet with the closest leading jet.

Validation of the 5^{th} jet

The kinematic distribution of the 5^{th} jet is also validated with the SM simulation samples. Especially, we concern whether the MC program models the ΔR between the 5^{th} jet and the closest reading jet. Figure 5.7 compares the 5^{th} jet E_T distributions for the case of $\Delta R < 1.0$ and $\Delta R \geq 1.0$ in the pretag sample. Figure 5.8 shows additional validation plots , ΔR distribution and the reconstruction χ^2, in the $t\bar{t}$ events with two b-jets. As observed from those validation plots, data agrees with the SM expectation pretty well regardless of the b-jet requirement.

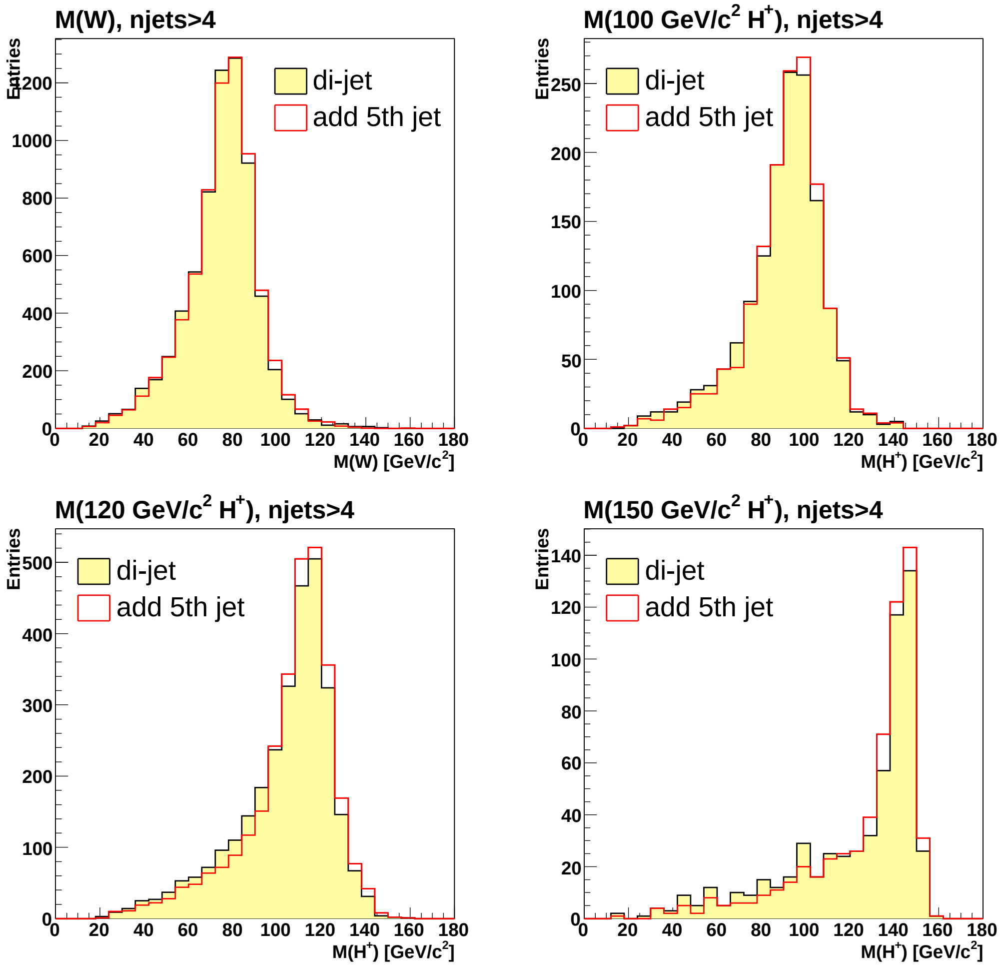

Figure 5.6: Dijet invariant mass before (yellow filled) and after (red solid) merging the 5^{th} jet with the closest leading jet. We use the $t\bar{t}$ samples with hadronic W (80.4 Gev/c^2) and H^+ with masses of 100, 120, 150 GeV/c^2.

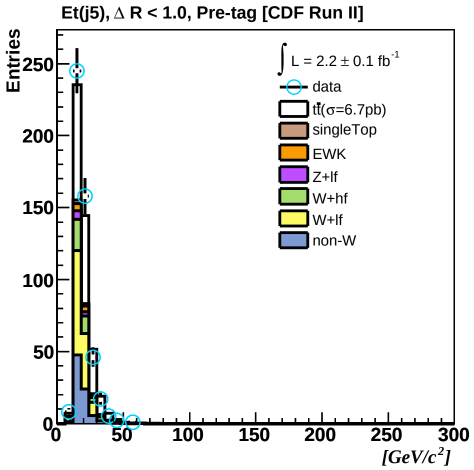

Et(j5), Δ R < 1.0, Pre-tag [CDF Run II]

Et(j5), Δ R >= 1.0, Pre-tag [CDF Run II]

Figure 5.7: E_T distribution of the 5^{th} jet for $\Delta R < 1.0$ (left) and > 1.0 (right) in pretag sample.

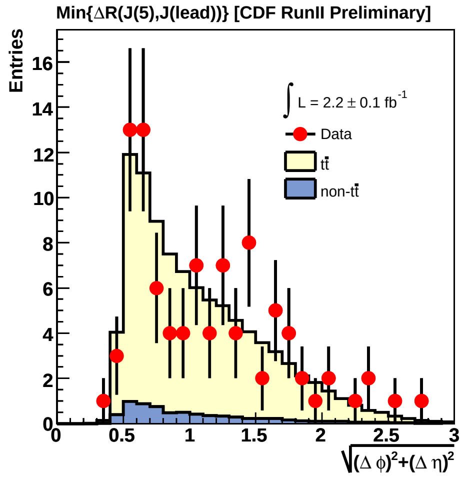

Min{ΔR(J(5),J(lead))} [CDF RunII Preliminary]

Reconstruction χ² [CDF RunII Preliminary]

Figure 5.8: ΔR between 5^{th} jet and the closest leading jet and the $t\bar{t}$ reconstruction χ^2 in $t\bar{t}$ events with two b-jets.

5.2.2 Mis-Assignments

Another cause of broadening the dijet mass distribution is a jet-parton mis-assignments in the $t\bar{t}$ event reconstruction. Figure 5.9 shows the dijet mass distribution for correct and incorrect jet-parton assignments. The correct combinations show clear mass peaks and good separation among MC samples of different Higgs masses. However, the reconstructed mass using wrongly assigned jets is spread all over the kinematically allowed mass region, and the mass separation between the MC samples is not achieved. The mis-assignment brings a common combinatory background in the kinematic reconstruction of the $t\bar{t}$ events.

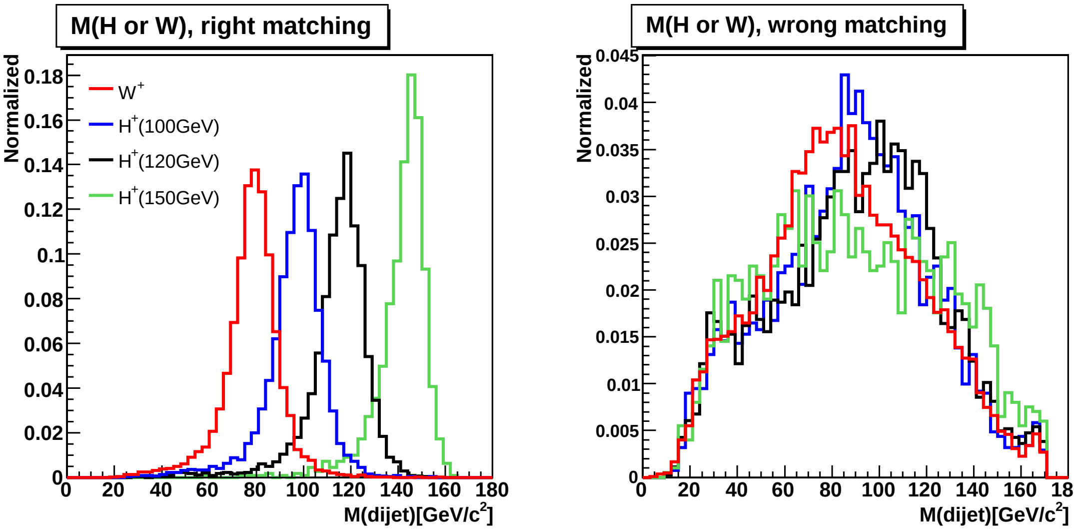

Figure 5.9: Dijet invariant mass distributions with four leading jets assigned to the correct partons (left) and to wrong partons (right). Each distribution is normalized by its area. Colors represents different MC samples, W in the SM $t\bar{t}$ (red), 100 GeV/c^2 H^+ (blue), 120 GeV/c^2 H^+ (black), and 150 GeV/c^2 H^+ (green).

Mis-assignments primarily happen in the selection of leading four jets when one or more jets do not originate directly from the $t\bar{t}$ decays. The jets decayed from the tree-level quarks are in general more energetic than the typical QCD gluon radiation jets. Since we choose the leading jets based on the jet E_T, a possibility exists that a hard gluon radiation jet (FSR or ISR) is selected as the leading jet. In the MC study, approximately 30% of the selected events have at least one leading jet coming out of the tree-level $t\bar{t}$ decays, called contaminated leading jet. Since all four leading jets are used in the kinematic fit, even one contaminated jet affects the entire energy corrections. Consequently, it results in a broader dijet mass distribution. Dijet mass contribution from the contaminated leading jet is shown in in red color in the Fig. 5.3.

The mis-assignment also comes from the imperfect $t\bar{t}$ reconstruction fitter. The χ^2 is the only criterion to determine the jets assignment to the tree-level partons. In the fitter, b-tagged jets are forced to be assigned to the b-quarks. If there are more than two b-jets in an event, only two of them are assigned to the b-quarks based on the χ^2 value; the b-jet assignment with minimum χ^2 is chosen to use. In particular, the $c\bar{s}$ decay in the H^+ sample may result in an additional b-tagged jet because the energetic c-jet can be tagged as a b-jet. The likelihood of a light quark-jet to be tagged as a b-jet is smaller. It is also possible that the c-jet from $W \to c\bar{s}$ decays is tagged as a b-jet. When all the selected leading four jets are decayed from tree-level quarks, the kinematic fitter chooses correct assignment in 80% of the time for the SM $t\bar{t}$ events, and in about 70% of the time for the Higgs $t\bar{t}$ events based on the MC study. The different rates in the mis-assignment primarily originates from c-jets contribution to the b-tags.

In order to reduce the mis-assignment rate, thereby improving the dijet mass resolution, we have carried out following studies. (1) If the reconstruction χ^2 is large, we release the jet assignment and ignore the b-tagging information for the less significant b-tagged jet. Then, we perform the kinematic fit again to choose the best assignment. (2) We remove poorly reconstructed $t\bar{t}$ events by imposing on a high-end χ^2 cut. Unfortunately these proposed methods do not improve the search sensitivity, thus they are not used in this analysis. Additional details on those studies are described in Appendix C and Appendix D.

5.3 Maximum Binned Likelihood Method

The dijet mass spectrum of the $t\bar{t}$ candidates includes primarily the W bosons, non-$t\bar{t}$ backgrounds which fake the $t\bar{t}$ events, and a possible H^+ signal in top quark decays. A maximum binned likelihood method is used to determine the relative contributions of these sources that best describes a given dijet mass distribution. The fit that yields the maximum likelihood value returns the best fractional compositions of the reconstructed dijet mass distribution. Assuming no H^+ signal beyond the SM, we estimate 95% C.L. upper limit on $\mathcal{B}(t \to H^+b)$ as extracted from the likelihood fit values. This is referred to as the SM expectation of the 95% C.L. upper limit.

5.3.1 Binned Likelihood Fitter Construction

A binned likelihood fitter is constructed employing Poisson probabilities:

$$\begin{aligned} LH &= \prod \frac{\nu_i^{n_i} \times e^{-\nu_i}}{n_i!} \bigotimes G(N_{\rm bkg}, \sigma_{N_{\rm bkg}}), \qquad (5.5)\\ \text{where} \quad \nu_i &= N_{t\bar{t}} \times (1 - \mathcal{B}(t \to H^+b)) \times \mathcal{B}(t \to H^+b) \times 2.0 \times \mathcal{A}_{H^+} \times P_i^{H^+} \\ &\times \mathcal{B}(W \to e/\mu/\tau + \nu) + N_{t\bar{t}} \times (1 - \mathcal{B}(t \to H^+b))^2 \times \mathcal{A}_W \times P_i^W \\ &+ N_{\rm bkg} \times P_i^{\rm bkg}. \end{aligned}$$

The Poisson probability is computed from the number of observed events, n_i, and the number of expected events, ν_i, in each mass bin. Here, each ν_i term corresponds to the sum of expected events from each H^+, W, and non-$t\bar{t}$ background with three fit parameters: $\mathcal{B}(t \to H^+b)$, $N_{t\bar{t}}$ ($= \sigma_{t\bar{t}} \times \mathcal{L}_{\rm int}$), and $N_{\rm bkg}$. The prior probability (P_i) of finding events in a bin i is obtained from simulated dijet mass distributions of H^+, W, and non-$t\bar{t}$ backgrounds which are referred to as templates. Here, $\mathcal{A}_{H^+}$ and $\mathcal{A}_W$ are the selection acceptances for H^+ and W events as discussed in the section 4.3. The leptonic W decay rate ($\mathcal{B}(W \to e/\mu/\tau + \nu)$ = 0.3257) is included in the first term above (the N_{H^+} component) because the charged Higgs MC samples are generated only with leptonic decays of the W (i.e. $W \to e/\mu/\tau + \bar{\nu}$). The $\mathcal{A}_W$ is calculated from an inclusive W sample, thus the W decay branching ratio is not specified in the second term (SM $t\bar{t}$ component).

The non-$t\bar{t}$ backgrounds estimate is discussed in Sec. 4.4. These events are a common background to both H^+ and W boson from $t\bar{t}$, since both are decay products of real $t\bar{t}$ events. Thus, in the likelihood (LH) fit, the parameter $N_{\rm bkg}$ is

Gaussian constrained within its uncertainty. Unlike the non-$t\bar{t}$ backgrounds, the fit parameters for the number of H^+ and W events are free to vary within -1.0 $\leq \mathcal{B}(t \rightarrow H^+b) \leq$ 1.0.

There are a few additional assumptions in the LH fit. These include (1) the sum of the total number of H^+, W, and non-$t\bar{t}$ backgrounds in the LH fit ($\sum_i \nu_i$) is Gaussian constrained to the total number of observed events ($\sum_i n_i$); (2) as mentioned earlier in the Higgs MC sample, the H^+ is assumed to decay 100% into $c\bar{s}$ (which is referred to as the leptophobic Higgs model); (3) The top quark decays 100% to either H^+ or W, thus satisfying the constraint $\mathcal{B}(t \rightarrow H^+b) + \mathcal{B}(t \rightarrow Wb) = 1$.

5.3.2 Mass Spectrum Templates

Templates consist of simulated dijet mass distributions for W, H^+, and non-$t\bar{t}$ background events. The H^+ signal templates for m_{H^+} values ranging from 60 to 150 GeV/c^2 are shown in Fig. 5.10 and compared to the W boson signal template from SM $t\bar{t}$ events.

The dijet mass contributions from various non-$t\bar{t}$ background sources are shown in the top plot of Fig. 5.11. Each background contribution is normalized to the estimated number of events as listed in Table 4.6. In the LH fit, a parametrized smooth background shape is used for the non-$t\bar{t}$ background template as shown in the bottom plot of Fig. 5.11.

5.3.3 Likelihood Fit

For a given dijet mass distribution, the MINUIT software package is used to minimize $-\ln LH$ (Eqn. 5.6). Fig. 5.12 shows an example of a fit to a pseudo-data sample, which is constructed to have the same number of W, H^+, and non-$t\bar{t}$ ($N_W = N_{H^+} = N_{\text{bkg}}$). This fit example shows good separations between the mass templates and a good agreement between the fit result and the pseudo-data distribution.

Performance of the LH fit is further tested using many pseudo-experiments (PE), which simulate the SM dijet mass distribution by a bin-to-bin Poisson

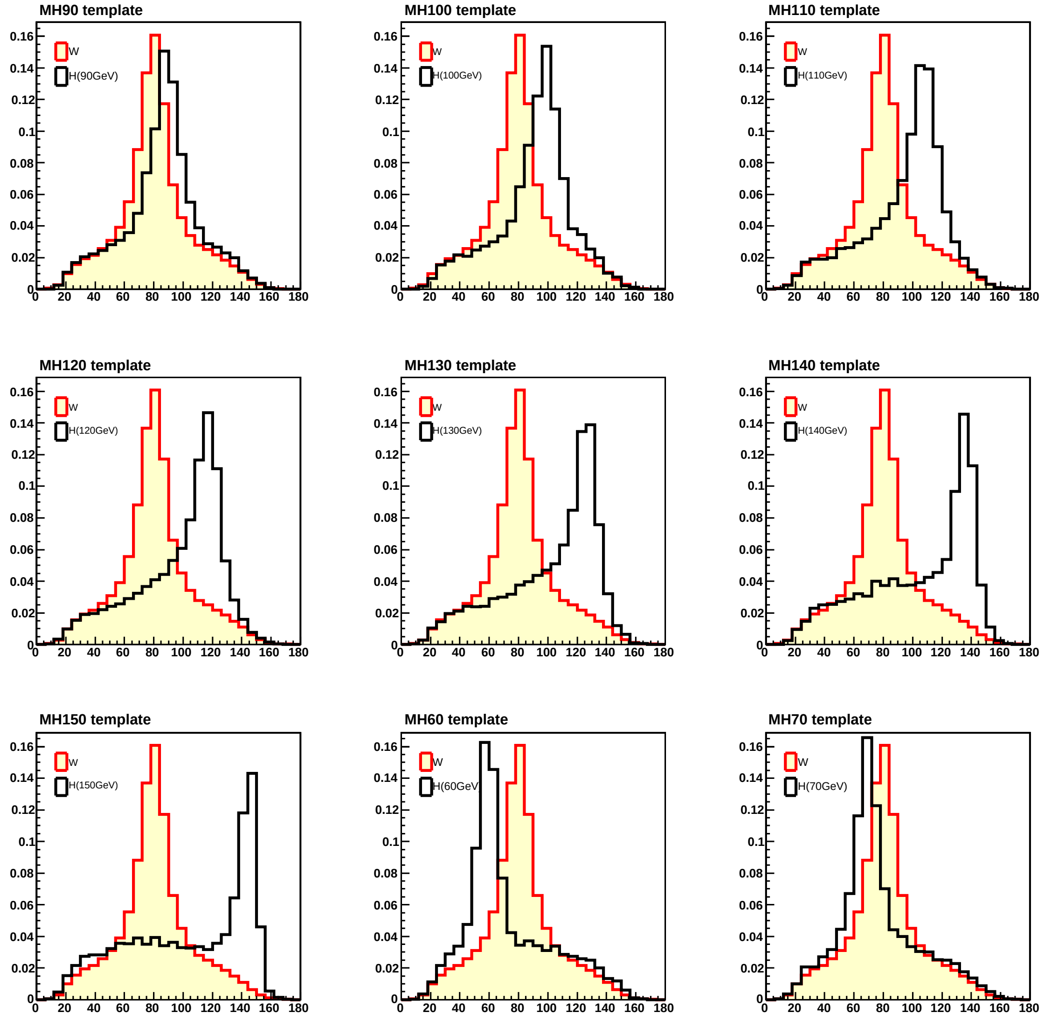

Figure 5.10: Signal m_{H^+} templates (black) compared with the W boson template (red, filled with yellow). From top left to bottom right, templates are shown for the assumed H^+ mass of 90, 100, 110, 120, 130, 140, 150, 60, and 70 GeV/c^2, respectively.

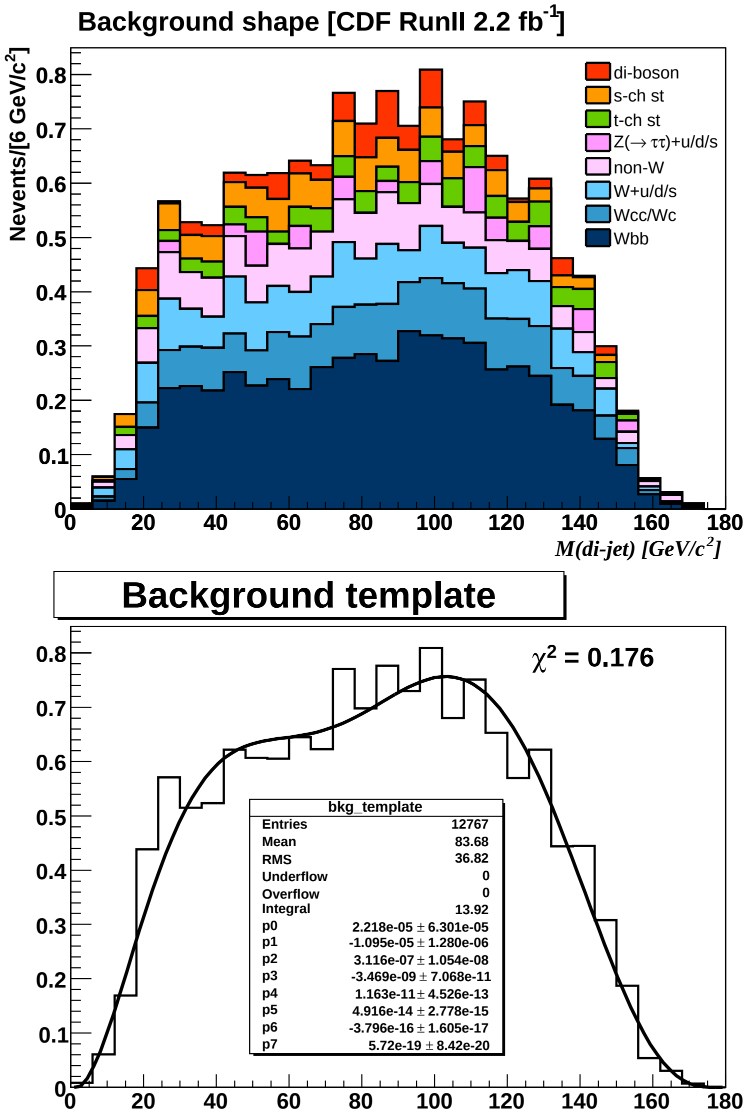

bkg_template	
Entries	12767
Mean	83.68
RMS	36.82
Underflow	0
Overflow	0
Integral	13.92
p0	2.218e-05 ± 6.301e-05
p1	-1.095e-05 ± 1.280e-06
p2	3.116e-07 ± 1.054e-08
p3	-3.469e-09 ± 7.068e-11
p4	1.163e-11 ± 4.526e-13
p5	4.916e-14 ± 2.778e-15
p6	-3.796e-16 ± 1.605e-17
p7	5.72e-19 ± 8.42e-20

Figure 5.11: Top: dijet mass distributions from the non-$t\bar{t}$ backgrounds in the selected $t\bar{t}$ candidates. Bottom: non-$t\bar{t}$ background template (solid line) as parameterized by a polynomial fit to the top plot.

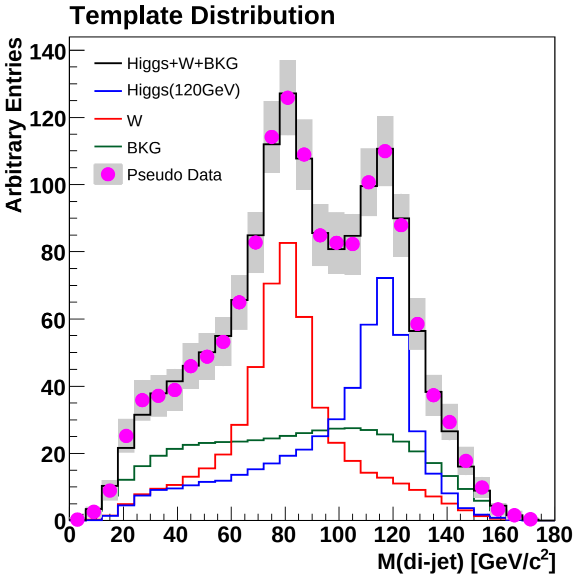

Figure 5.12: An example (for 120 GeV/c^2 H^+) of a likelihood fit to a dummy pseudo-data sample. The pseudo-data is constructed to have the same number of W, H^+, and non-$t\bar{t}$ ($N_W = N_{H^+} = N_{\rm bkg}$) events.

fluctuation of the templates. The three LH fit parameters for a thousand SM pseudo-experiments are shown in Fig. 5.13, where the simulated PEs are constructed to include only W $t\bar{t}$ signal and non-$t\bar{t}$ background events.

Figure 5.14 compares the output $\mathcal{B}(t \to H^+b)$ and the fit errors with expectation in the LH fits to a thousand SM PEs, for different Higgs masses of 60 to 150 GeV/c^2. Since no Higgs events are included in the PEs, the fit result for the branching ratio, $\mathcal{B}(t \to H^+b)$, is expected to be zero. Pull distributions[1] show that the LH fit returns $\mathcal{B}(t \to H^+b)$ output as expected in the SM (which is zero) within 0.1 of the fit error, σ, for any H^+ mass. Also the individual fit errors for the $\mathcal{B}(t \to H^+b)$ are consistent among all PE sets[2]. In conclusion, the LH fit does

---

[1] Pull distribution for variable k shows how the average measured value compares to the expected value and defined as: $\dfrac{k_{\rm measured} - k_{\rm expected}}{\sigma_k}$.

[2] Pull width is calculated as $\frac{\sum_{\rm i}^{\rm n} \sigma_{\rm i}/{\rm n}}{\sigma}$, where n is the number of PEs, σ_i is an individual fit error, and σ is width of output $\mathcal{B}(t \to H^+b)$ distributions.

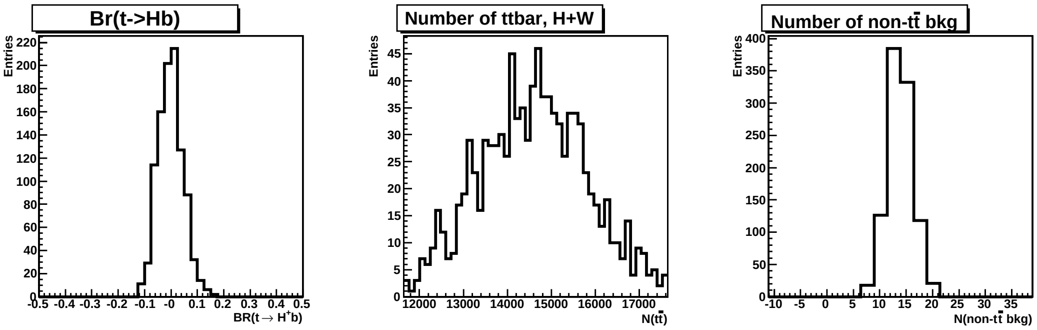

Figure 5.13: LH fit results from a thousand null-Higgs pseudo-experiments; $\mathcal{B}(t \to H^+b)$, $N_{t\bar{t}}$, and $N_{\rm bkg}$.

not have any bias in the determination of the $\mathcal{B}(t \to H^+b)$ and the association error, regardless of the H^+ mass. Additional LH integrity tests are discussed in Appendix E.

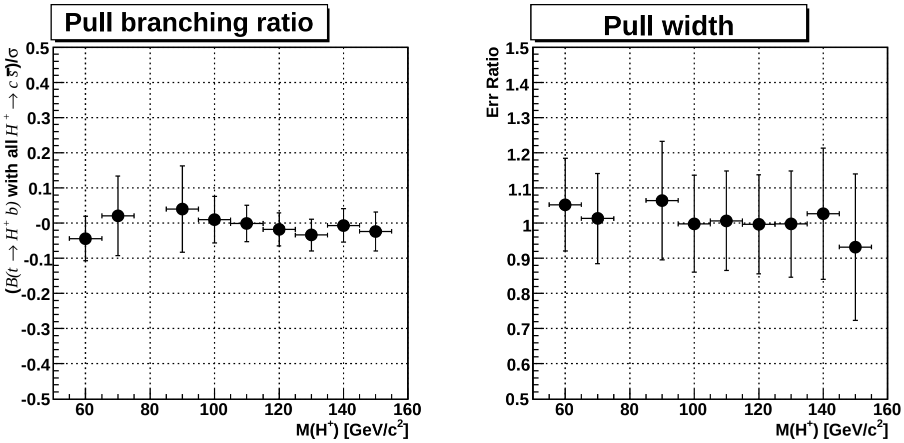

Figure 5.14: (Left) Pull distribution of the $\mathcal{B}(t \to H^+b)$ fit results (expected to be zero) as a function of charged Higgs mass. (Right) The average of the individual fit errors on the $\mathcal{B}(t \to H^+b)$ divided by the width of the output $\mathcal{B}(t \to H^+b)$ distribution (expected to be 1.0).

5.3.4 Extracting an Upper Limit

The upper limit on $\mathcal{B}(t \to H^+b)$ at 95% confidence level (C.L.) is extracted using the likelihood shape as a function of $\mathcal{B}(t \to H^+b)$. The likelihood values is computed by fixing $N_{t\bar{t}}$ and N_{bkg} to the best values obtained from the maximum LH fit, and manually varying the $\mathcal{B}(t \to H^+b)$ from -1 to 1. The upper limit is estimated from the integration of the LH values in the positive $\mathcal{B}(t \to H^+b)$ region as shown in Fig. 5.15. The negative branching ratio region is not used for the limit because negative $\mathcal{B}(t \to H^+b)$ is unphysical. The negatives originate from a downward fluctuation in the dijet mass distribution in the PE. The projection on to the x-axis where the integration reaches 95% of total positive area is the upper limit on $\mathcal{B}(t \to H^+b)$ at 95% C.L. This upper limit calculation method is based on Bayes' theorem assuming a flat prior probability.

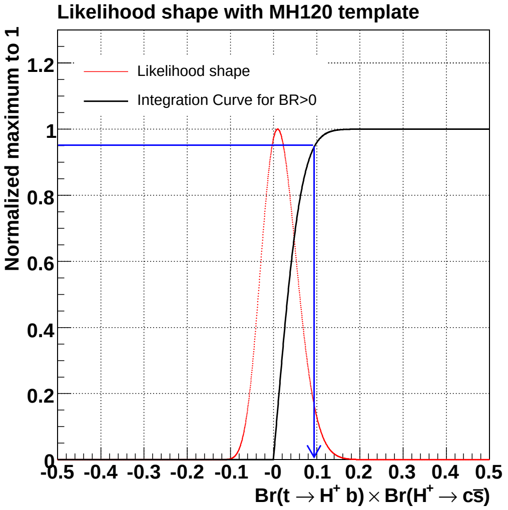

Figure 5.15: Likelihood shape (red dots) from a fit to a pseudo-experiment and the integration over positive $\mathcal{B}(t \to H^+b)$ values (black solid) for the determination of a 95% C.L. estimate (blue arrow).

The SM expectation of the 95% C.L. upper limit on $\mathcal{B}(t \to H^+b)$ is obtained by the averaged outputs of the LH fits to a thousand null-Higgs PEs, consisting of SM $t\bar{t}$ and non-$t\bar{t}$ background events. An upper limit with 95% C.L. is calculated for each PE. Then, the upper limits from a thousand PEs are distributed as shown in the Fig. 5.16. The mean of the upper limit distributions is referred to as the SM expectation of the 95 % C.L. upper limit on $\mathcal{B}(t \rightarrow H^+b)$. The upper and lower bounds that contain central 68% and 95% of the upper limit results are defined as the 1σ and 2σ statistical fluctuations in the determination of the 95% C.L. upper limit.

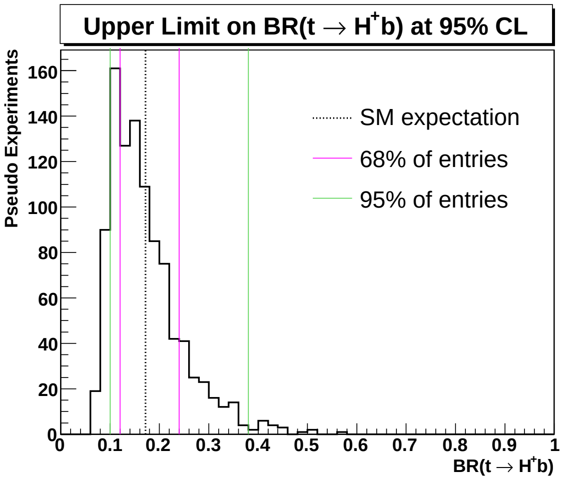

Figure 5.16: The 95% C.L. upper limit distributions from LH fits to a thousand pseudo-experiments. Dotted line represents the mean of the histogram, and the magenta and green lines show the boundaries where 68% and 95% of the pseudo-experiments are included.

Repeating the same process for different H^+ mass templates yields the SM expected upper limits on $\mathcal{B}(t \rightarrow H^+b)$ as a function of m_{H^+}. The 95 % C.L. upper limits, and 1σ and 2σ bands are shown in Fig. 5.17. These limits do not include the effects of systematic uncertainties. The systematic uncertainty estimation follows, and the limits including systematic uncertainties are shown later in Fig. 5.30.

5.4 Systematic Uncertainty

There are a number of sources of systematic uncertainties that affect the result of the LH fit. These include uncertainties from the jet energy scale (JES) corrections, modeling the initial and final state radiations (ISR and FSR), the choice

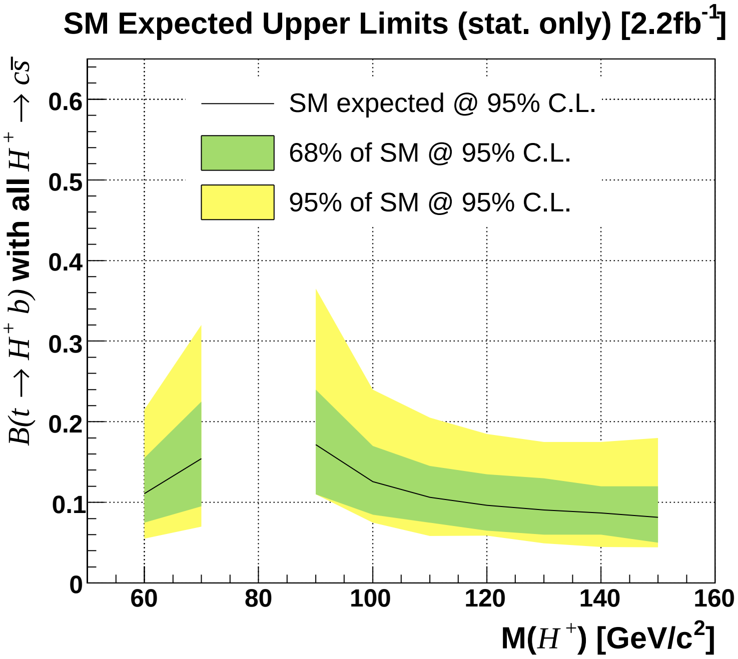

Figure 5.17: The 95% C.L. upper limits on $\mathcal{B}(t \to H^+ b)$ for H^+ masses of 60 to 150 GeV/c^2 from a thousand simulated pseudo-experiments, assuming CDF data sample of 2.2 fb^{-1}. The 68% and 95% statistical fluctuations of the upper limit are shown.

of Q^2 scale in the W+jets background simulations, the choice of MC generators in the simulations, and from the b-tagging efficiency scale factor.

These systematic sources, except for the b-tagging efficiency scale factor, perturb the shape of the dijet mass distribution and therefore result in a shift in the extracted value of $\mathcal{B}(t \to H^+ b)$. The systematic uncertainty is estimated as a change in $\mathcal{B}(t \to H^+ b)$ for a $\pm 1\sigma$ change of each systematic source. The perturbed dijet mass for each systematic error is simulated with MC samples. Then a thousand pseudo-experiments are generated using the perturbed dijet mass to mimic perturbed data for each systematic source. Then, the shift in the output $\mathcal{B}(t \to H^+ b)$ is extracted by comparing the output branching ratio of the perturbed PEs with that of the unperturbed PEs.

The systematic uncertainties in the b-tagging efficiency scale factor, JES, ISR, FSR, and choice of MC generator also change the selection acceptances for H^+

and W events ($\mathcal{A}_W$ and $\mathcal{A}_{H^+}$). The acceptance shifts from systematic sources are combined in quadrature and listed in Table 4.4. The systematic uncertainty is estimated by replacing the $\mathcal{A}_W$ and $\mathcal{A}_{H^+}$ with the shifted acceptances.

The systematic uncertainty, the shift in $\mathcal{B}(t \to H^+b)$, is parameterized as a linear function of the input $\mathcal{B}(t \to H^+b)$. Five different sets of PEs are used for the estimation of the systematic uncertainty; each PE set includes 0, 2, 5, 10, or 20 H^+ events in the sample distribution, separately. Total number of $t\bar{t}$ ($= N_{H^+} + N_W$) and non-$t\bar{t}$ events in the sample are normalized to the expected numbers in Sec. 4.4. The input $\mathcal{B}(t \to H^+b)$ for the corresponding number of H^+ events is calculated by taking into account the acceptances for each m_{H^+} assumption.

5.4.1 Jet Energy Scale Correction

The jet energy scale systematic sample is simulated by scaling each correction value by $\pm 1\sigma$. A positive (negative) shift in the JES correction moves the dijet mass peak slightly higher (lower) than the nominal JES correction since the reconstructed jets are more (less) energetic as shown in Fig. 5.18. The shift in the output $\mathcal{B}(t \to H^+b)$ due to the uncertainty in the JES correction is shown in Fig. 5.19.

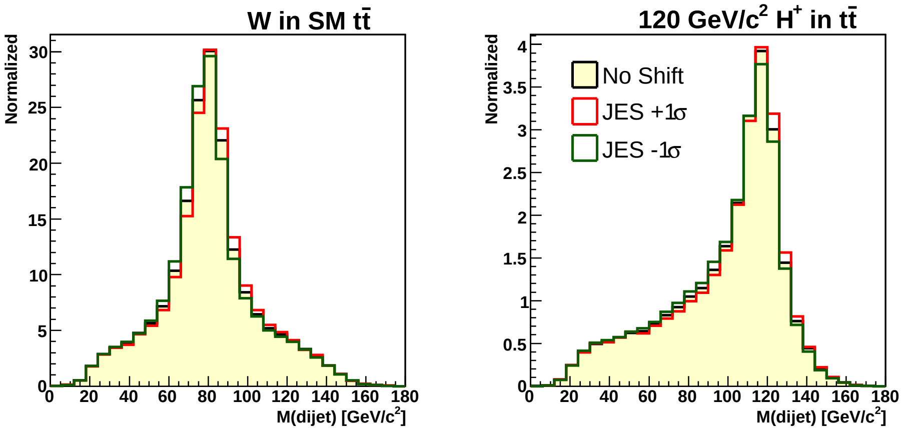

Figure 5.18: The template compared with the perturbed dijet mass distributions with a $\pm 1\sigma$ JES shift.

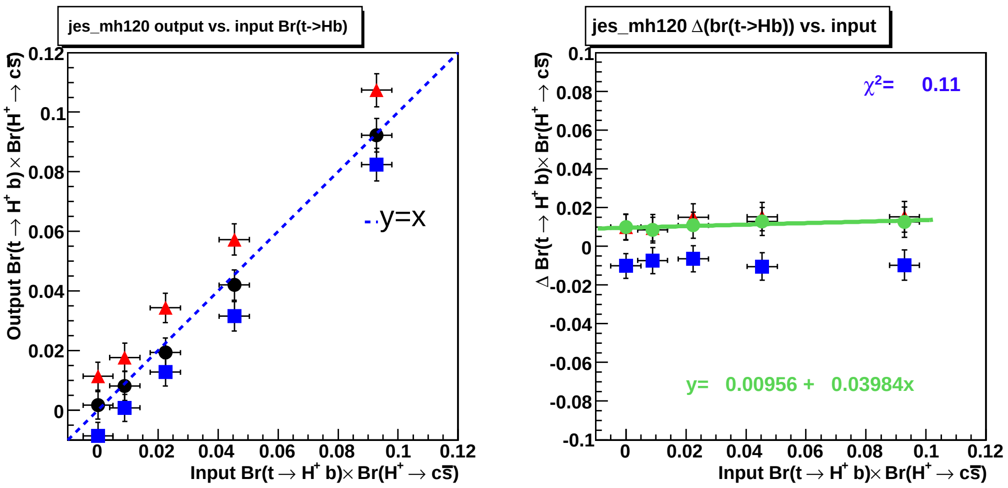

Figure 5.19: (Left) Output $\mathcal{B}(t \rightarrow H^+b)$ shift due to the $\pm1\sigma$ JES in the 120 GeV/c^2 H^+ sample. (Right) The difference of the output $\mathcal{B}(t \rightarrow H^+b)$ in the JES perturbed sample as a function of input $\mathcal{B}(t \rightarrow H^+b)$. Black dot: normal output, red(blue) dot: output with +1(-1)σ shift, green line: linear fit to the absolute average shifts in the output branching ratio.

5.4.2 Monte Carlo Generator

In this analysis, all the $t\bar{t}$ samples are simulated with the PYTHIA MC program. The PYTHIA program is chosen because of the relative ease in the tuning of simulation parameters, e.g. the gluon radiation tuning. For this MC the predicted p_T spectra are in agreement with experimental data. However, no single simulation program can perfectly describe all the features of experimental data. This may result in an unintentional bias in the analysis.

We use $t\bar{t}$ simulated samples generated by using the HERWIG MC program [81] in order to estimate a possible bias that originates from using PYTHIA MC samples only. Each of the two MC programs has different deficiencies in the event generation and parton showering modeling. For example, PYTHIA simulates the underlying events but HERWIG does not. On the other hand, HERWIG includes spin correlations in the matrix element calculation, but PYTHIA does not.

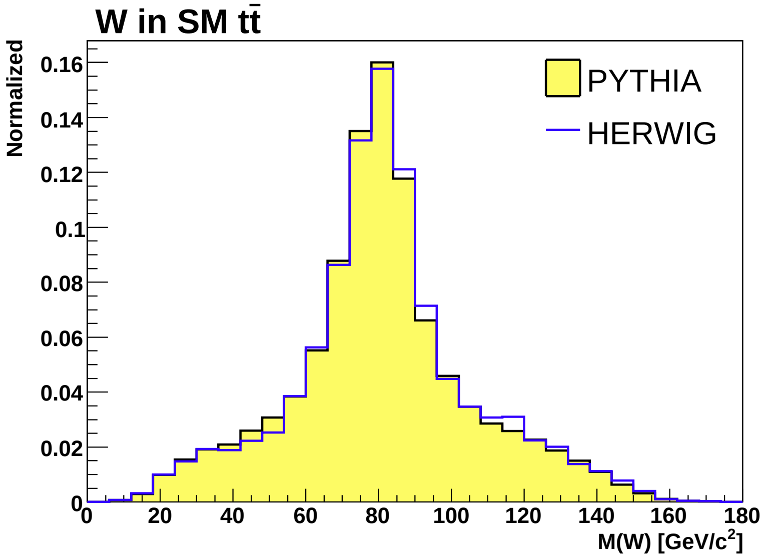

Figure 5.20: Reconstructed hadronic W mass distribution in $t\bar{t}$ events simulated by PYTHIA and HERWIG MC programs.

Figure 5.20 compares the reconstructed W mass from PYTHIA and HERWIG event generators. The W boson samples are generated with almost the same input mass in both MC programs (80.42 ± 2.124 GeV/c^2 in PYTHIA and 80.33 ± 2.123 GeV/c^2 in HERWIG). However, the width of the W reconstruction mass distribution for events simulated with HERWIG is slightly wider than the corresponding distribution for events simulated with PYTHIA. This is possibly caused by different parton showering algorithms. The systematic uncertainty is estimated by comparing the LH output $\mathcal{B}(t \to H^+b)$ results extracted using PEs with those MC generators as shown in Fig. 5.21.

5.4.3 Initial/Final State Radiation

To estimate the effect of QCD gluon radiation, the standard parameters in the PYTHIA MC simulation are tuned to enhance or reduce the initial and final state radiation by a factor of 2.0 and 0.5, respectively. As discussed in Sec. 5.2.1, ISR is the QCD gluon radiation from the incoming partons in the proton and antiproton, and FSR is the QCD radiation from the final state quarks in $t\bar{t}$ decays.

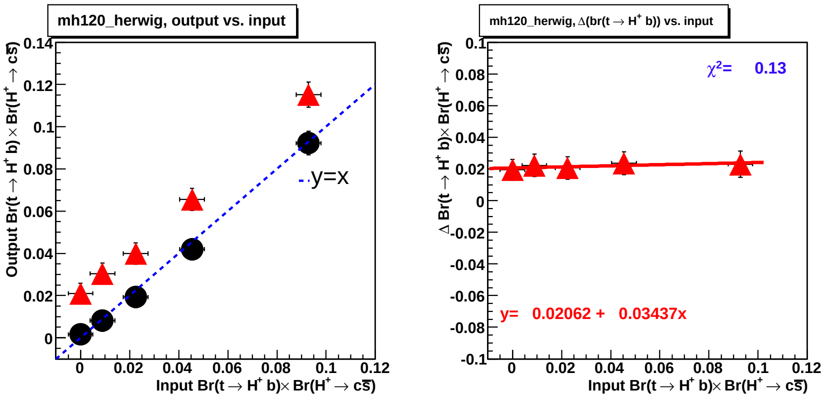

Figure 5.21: (Left) Output $\mathcal{B}(t \to H^+b)$ shift resulting from the HERWIG W dijet mass (red triangles) as compared to the outputs from PYTHIA W dijet mass (black dots). (Right) The differences between the two results as a function of input $\mathcal{B}(t \to H^+b)$ for 120 GeV/c^2 Higgs. The red line is a linear fit to the shift in the output branching ratio.

The ISR/FSR samples are simulated for the $t\bar{t}$ production with W, 120 GeV/c^2 H^+, and 150 GeV/c^2 H^+ as shown in Fig. 5.22.

This systematic uncertainty is estimated for the m_{H^+} of 120 and 150 GeV/c^2 as is done for the uncertainty measurement in the JES correction. The uncertainty for other H^+ masses for which we do not have the ISR/FSR MC samples is extrapolated or interpolated linearly from the measured uncertainties as shown in Fig. 5.23. The extrapolated uncertainty should not exceed either measured values; for that case, we assign the smallest measured value instead. Table 5.2 lists the shifts in the branching ratios ($\Delta\mathcal{B}(t \to H^+b)$) that originate from the ISR/FSR systematic for all H^+ masses for input $\mathcal{B}(t \to H^+b)$ of 0. The uncertainties for non-zero input values of $\mathcal{B}(t \to H^+b)$ are determined assuming 2, 5, 10, and 20 H^+ events, then are linearly parameterized as shown in Fig. 5.27.

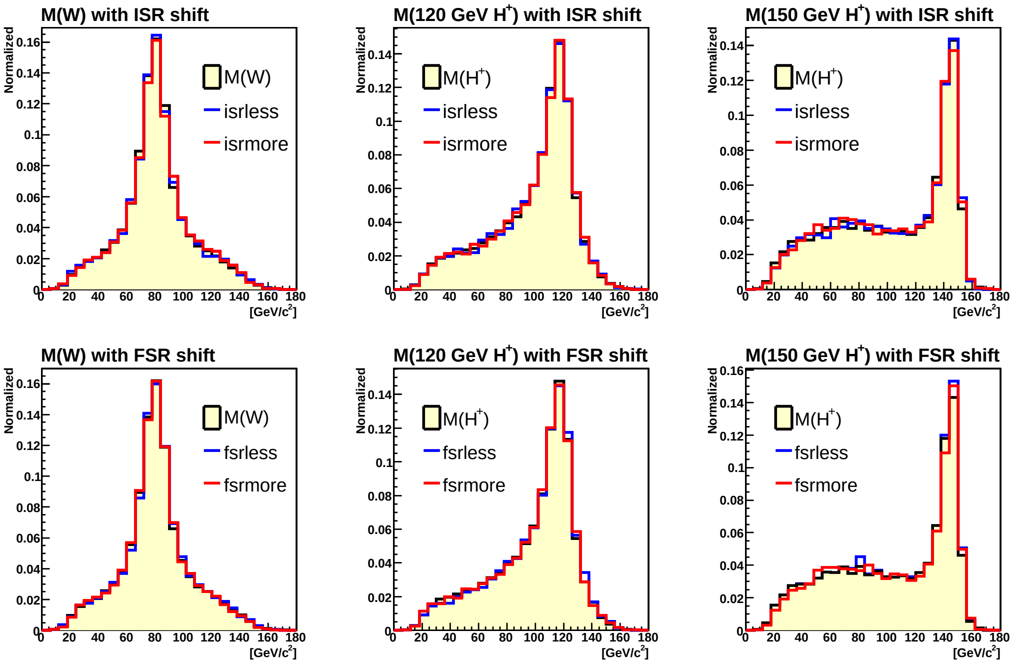
M(W) with ISR shift

M(120 GeV H^+) with ISR shift

M(150 GeV H^+) with ISR shift

M(W) with FSR shift

M(120 GeV H^+) with FSR shift

M(150 GeV H^+) with FSR shift

Figure 5.22: Perturbed dijet mass distributions with enhanced and reduced ISR (top) and FSR (bottom) by a factor of 2.0 and 0.5, respectively.

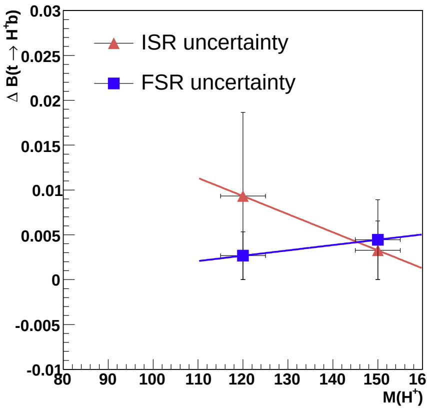

Figure 5.23: Shift in the output $\mathcal{B}(t \to H^+b)$ for 120 and 150 GeV/c^2 H^+ bosons and the linear extrapolation fits (with enhanced and reduced ISR and FSR by a factor of 2.0 and 0.5, respectively)

m_{H^+} (GeV/c^2)	ISR $\Delta\mathcal{B}(t \to H^+b)$	FSR $\Delta\mathcal{B}(t \to H^+b)$
120	0.00932	0.00267
150	0.00327	0.00445
90	0.01537	0.00267
100	0.01336	0.00267
110	0.01134	0.00267
130	0.00730	0.00326
140	0.00529	0.00386

Table 5.2: Averaged output branching ratio shift from ISR/FSR enhanced and reduced samples by a factor or 2.0 and 0.5 for the 120 GeV/c^2 and 150 GeV/c^2 H^+ bosons, where input $\mathcal{B}(t \to H^+b) = 0$. The uncertainties for other H^+ masses are linearly extrapolated/interpolated using the measured uncertainties.

5.4.4 *b*-tagging Efficiency Scale Factor

The ratio of the loose *b*-tagging efficiency between the data and MC simulation is determined to be 0.95 ± 0.05 (Eqn. 4.6). In the acceptance calculation, the *b*-tagging efficiency scale factor is directly applied to the selected MC events. Therefore, a $\pm 1\sigma$ difference in the scale factor for the *b*-tagging efficiency changes the acceptance as shown in Table 5.3. However, the shape of dijet mass distribution is intact in such changes in the *b*-tagging scale factor.

The systematic uncertainty from the *b*-tagging efficiency scale factor is measured by using the shifted acceptances (from the $\pm 1\sigma$ uncertainty in the *b*-tagging efficiency scale factor) instead of the normal acceptances in the Eqn. 5.6. Figure 5.24 shows that there is a negligible shift in the output branching ratio although we expect higher branching ratio (e.g. $\Delta\mathcal{B}(t \to H^+b)$ at input $\mathcal{B}(t \to H^+b)$= 0.2 is only 0.00075).

m_{H^+} (GeV/c^2)	$+1\sigma$ (%)	b-tag SF = 0.95 (%)	-1σ (%)
standard $t\bar{t}$ ($W^{\pm}$)	2.557±0.208	2.319 ± 0.189	2.090 ± 0.170
60	2.357±0.298	2.145±0.272	1.940±0.247
70	2.471±0.312	2.250±0.285	2.036±0.259
90	2.632±0.330	2.397±0.302	2.169 ± 0.274
100	2.662±0.334	2.424±0.305	2.194±0.277
110	2.670±0.335	2.432±0.306	2.202±0.278
120	2.589±0.319	2.358±0.291	2.134±0.264
130	2.375±0.299	2.163±0.298	1.958±0.249
140	1.942±0.247	1.767±0.226	1.598±0.205
150	1.391±0.180	1.262±0.164	1.138±0.149

Table 5.3: Selection acceptances of the SM $t\bar{t}$ and H^+ events for a $\pm 1\sigma$ shift in the b-tagging efficiency scale factor.

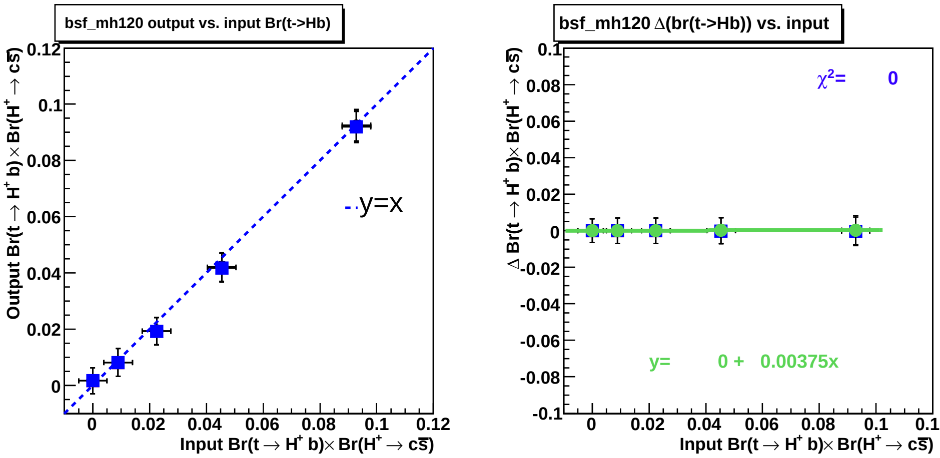

Figure 5.24: (Left) Output $\mathcal{B}(t \to H^+b)$ shift and (Right) the differences resulting from the acceptance changes due to $\pm 1\sigma$ shift in b-tag scale factor for 120 GeV/c^2 H^+. Black (normal output), red (with $+1\sigma$) and blue (with -1σ) dots are overlapped in the left plots. The average $\Delta\mathcal{B}(t \to H^+b)$ is shown in green on the right plot.

5.4.5 QCD Q^2 Scale and the W+jets Background

There is an uncertainty in the dijet mass distribution for the backgrounds from W+jet events. It results from the large uncertainty in the theory prediction of the W+jets production energy scale. This systematic uncertainty is estimated by using various momentum transfer which is used as the scale $(Q^2)^3$, where the theoretical cross sections are calculated. In order to get the perturbed background dijet mass distribution, the W+jets samples are simulated with twice and a half of the nominal Q^2 value, respectively. This is done using the ALPGEN generator with PYTHIA parton showering in the MC simulation. Figure 5.25 compares the dijet mass distributions in MC samples generated with two different Q^2 scale factors. The $\mathcal{B}(t \rightarrow H^+b)$ shift from the perturbed background shape is shown in Fig. 5.26. The average branching ratio shift from both samples is taken as the systematic uncertainty for the W+jets background production scale.

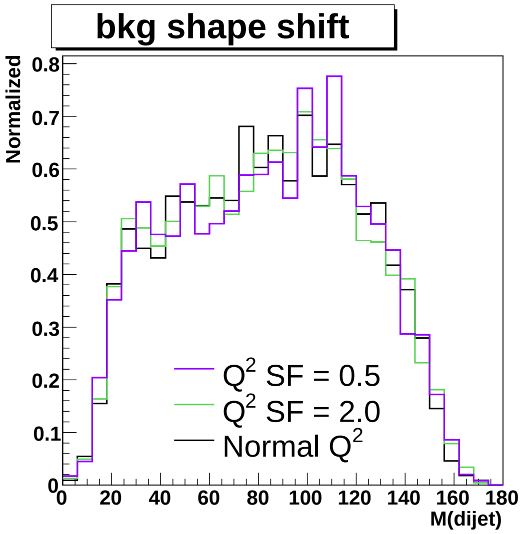

Figure 5.25: W+jets dijet mass perturbation from varying the QCD Q^2 production scale.

---

[3] Here Q^2 is defined as $\sqrt{{m_W}^2 + \sum_{\text{jets}} {m_T}^2}$ in the ALPGEN event generator.

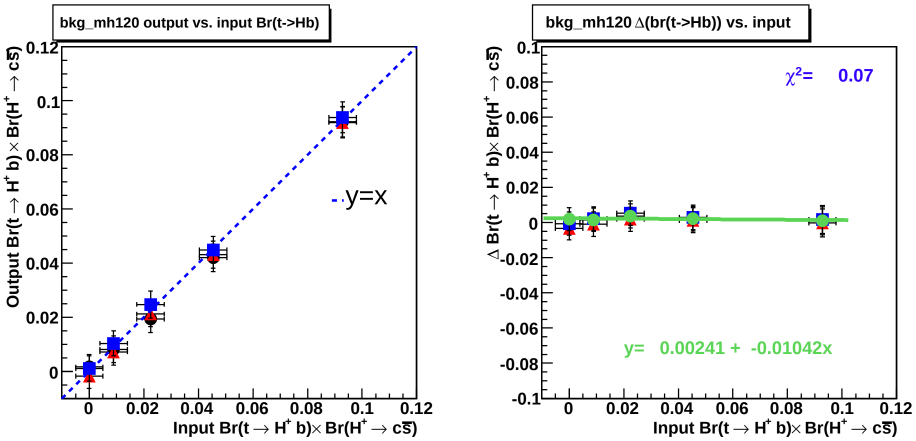

Figure 5.26: (Left) Output $\mathcal{B}(t \to H^+b)$ shift originating from the various W+jet background production scale. (Right) The differences in output $\mathcal{B}(t \to H^+b)$ are shown as a function of input $\mathcal{B}(t \to H^+b)$ for 120 GeV/c^2 H^+. Black dot: normal output, red dot: Q^2 scale factor = 2.0, blue dot: Q^2 scale factor = 0.5, green line: average of the absolute $\mathcal{B}(t \to H^+b)$ shifts.

5.4.6 The Total Systematic Uncertainty

All the systematic uncertainties are summarized in Fig. 5.27. The uncertainties are extrapolated or interpolated for each systematic error using a linear function of input $\mathcal{B}(t \to H^+b)$ for H^+ masses of 60 to 150 GeV/c^2. The uncertainty from the JES is dominant as m_{H^+} approaches to the m_W, otherwise the uncertainty originating from the choice of MC generators is significant. It should be noted that the uncertainties due to the acceptance changes are negligible compared to the shape systematic uncertainties based on the study of b-tagging scale factor uncertainty. Figure 5.28 shows the total systematic uncertainty estimated by combining the individual systematic uncertainties in quadrature.

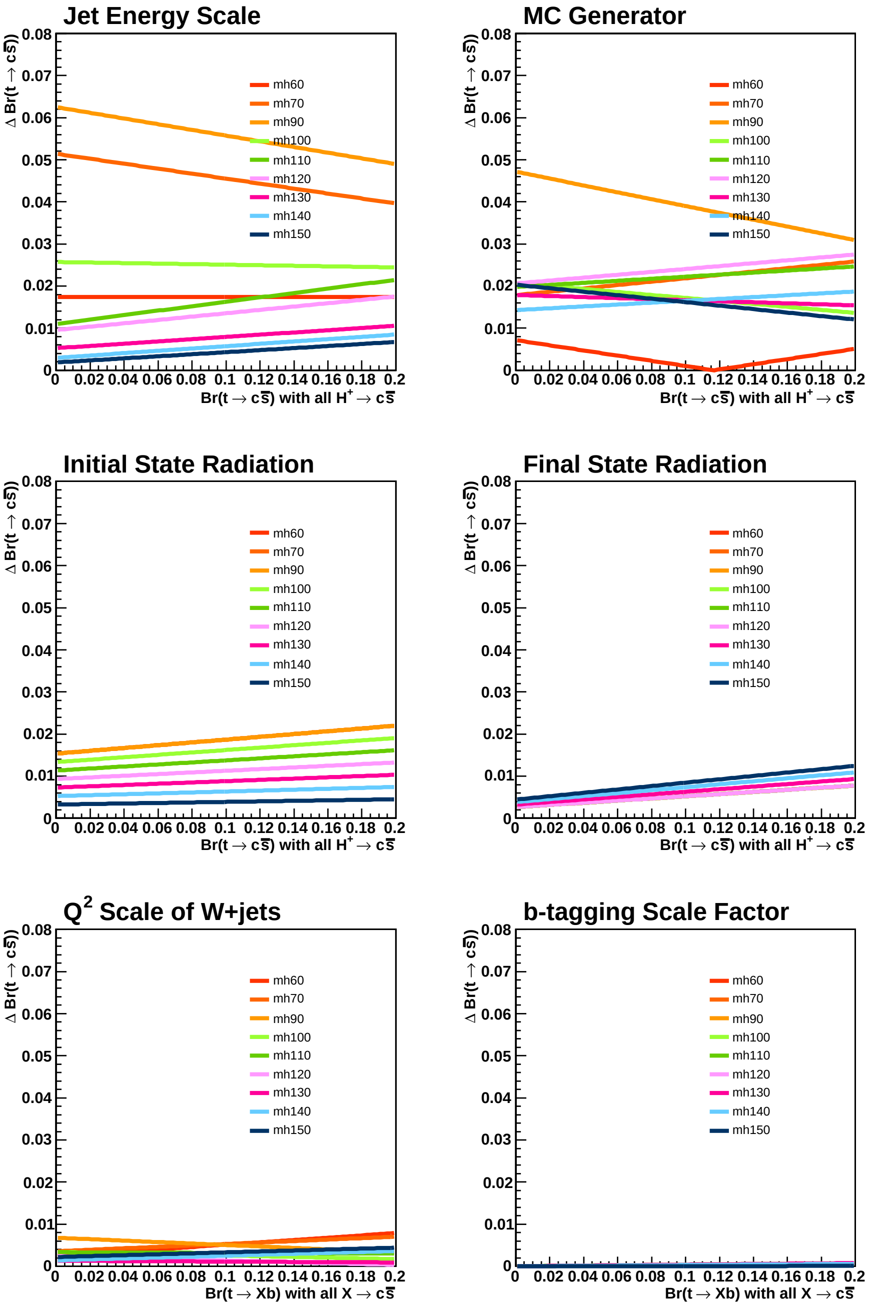

Figure 5.27: Systematic uncertainty from the JES, MC generator, ISR, FSR, W+jets production scale, and the b-tagging scale factors. The uncertainties are estimated as a linear function of $\mathcal{B}(t \to H^+ b)$ for H^+ masses of 60 to 150 GeV/c^2.

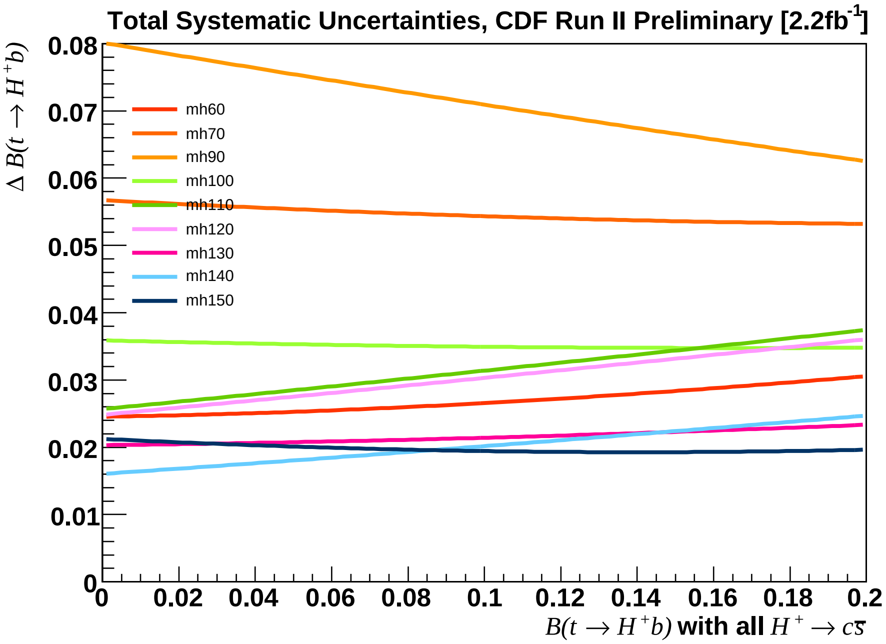

Figure 5.28: Combined systematic uncertainty (Δx) as a linear function of $\mathcal{B}(t \to H^+b)$ for H^+ masses of 60 to 150 GeV/c^2.

Uncertainty from the Top Quark Mass Constraint

We finally investigate a possible shift in $\mathcal{B}(t \to H^+b)$ originating from uncertainty in the value of the top quark mass used as a constraint in the LH fit. In this analysis, the top quark is assumed to have a mass of 175 GeV/c^2, and all the $t\bar{t}$ events in the data are kinematically reconstructed by constraining each top quark mass to be 175 GeV/c^2 (See Sec. 5.1). However, this assumed value of m_t is different from the current best measured top quark mass, which is 172.4 ± 0.7 (stat) ± 1.0 (syst) GeV/c^2 (as of summer 2008 [82]). In order to estimate a possible bias in the output $\mathcal{B}(t \to H^+b)$ from constraining wrong m_t, the same analysis is performed by constraining m_t to 170 GeV/c^2 instead of 175 GeV/c^2 (true m_t in the simulation sample is still 175 GeV/c^2). The template distributions are changed according to the new m_t constraint. Then, the systematic uncertainty is evaluated by the shift in the output $\mathcal{B}(t \to H^+b)$ from using $m_t = 170$ GeV/c^2

as compared to the output $\mathcal{B}(t \to H^+b)$ with $m_t = 175$ GeV/c^2. A comparison of this shift with the other systematic uncertainties is given in Table 5.4 for input $\mathcal{B}(t \to H^+b) = 0$. We find that the uncertainty from constraining the top quark mass to 175 GeV/c^2 instead of 172.4 GeV/c^2 would be negligible compared to the other systematic uncertainties for all H^+ masses.

m_{H^+} (GeV/c^2)	JES	MC gen.	ISR	FSR	Q^2	m_t= 170 GeV/c^2
60	0.017	0.007	0.015	0.003	0.002	0.001
70	0.051	0.018	0.015	0.003	0.004	0.002
90	0.063	0.047	0.015	0.003	0.008	0.001
100	0.026	0.021	0.013	0.003	0.003	0.002
110	0.011	0.020	0.011	0.003	0.003	0.001
120	0.010	0.021	0.009	0.002	0.002	0.001
130	0.005	0.018	0.007	0.003	0.003	0.002
140	0.003	0.014	0.005	0.004	0.001	0.001
150	0.002	0.020	0.003	0.004	0.002	0.001

Table 5.4: Systematic uncertainty estimation, $|\Delta\mathcal{B}(t \to H^+b)|$, for the case of null-Higgs (SM) assumption, $\mathcal{B}(t \to H^+b) = 0$.

5.5 Setting Upper Limits on $\mathcal{B}(t \to H^+b)$

In the SM, the top quark exclusively decays to a W boson and a bottom quark. However, imperfections in particle reconstruction results in a much broader W mass than its natural width. and the limitation of the statistics cause fluctuations of the events. So far, we have only accounted for statistical fluctuations in the dijet mass spectrum in SM $t\bar{t}$ events for the upper limit on $\mathcal{B}(t \to H^+b)$.

The SM expectation of the upper limits on $\mathcal{B}(t \to H^+b)$ without systematic errors is shown in Fig. 5.17. However, the output $\mathcal{B}(t \to H^+b)$ in the LH fit can be shifted by various additional systematic errors. To take into account the systematic errors, we use the total systematic uncertainty Δx as a function of $x = \mathcal{B}(t \to H^+b)$ in Fig. 5.28. The systematic uncertainty is used to smear the likelihood shape as

$$LH'(x') = \int_0^1 LH(x) \times \frac{1}{\Delta(x')\sqrt{2\pi}}\ exp(-\frac{1}{2}(\frac{x'-x}{\Delta(x')})^2)dx. \tag{5.6}$$

Here, $LH(x)$ is the extracted LH value from Sec. 5.3.4 as a function of x. Both x and x' represent the input $\mathcal{B}(t \rightarrow H^+b)$ and vary between 0 and 1. The smeared LH value at a branching ratio x' ($LH'(x')$) is computed from $LH(x)$ convoluted with the Gaussian probability for allowed branching ratio ($0 \leq x \leq 1$). The maximum contribution to $LH'(x')$ comes from the $LH(x)$ at $x = x'$. However, $LH(x)$ at $x \neq x'$ can also contribute to the $LH(x')$ according to the Gaussian smearing with the systematic uncertainty, $\Delta(x')$.

Figure 5.29 shows how $LH(x)$ is smeared out to $LH'(x')$ when systematic uncertainties are included. The upper limit is recalculated from the smeared LH values as well. Based on the simulation study, the upper limits including systematic uncertainty increase by 10% to as much as 25% for values of m_{H^+} close to m_{W^+}. Figure 5.30 shows the 95% C.L. upper limits on $\mathcal{B}(t \rightarrow H^+b)$ including the systematic uncertainty for H^+ masses of 60 to 150 GeV/c^2. The upper limits are obtained from pseudo-experiments assuming a CDF II data sample of 2.2 fb^{-1} and no H^+ boson in the $t\bar{t}$ events. The ±1, 2σ fluctuations in the average SM expected upper limits are shown as colored bands.

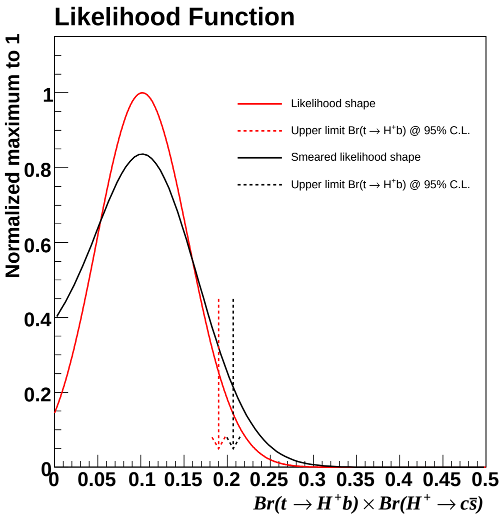

Figure 5.29: Gaussian smearing of the likelihood (black) with the systematic uncertainties as compared with the original likelihood value (red). The upper limit on $\mathcal{B}(t \to H^+b)$ is increased by the effect of systematic errors (red to black arrow).

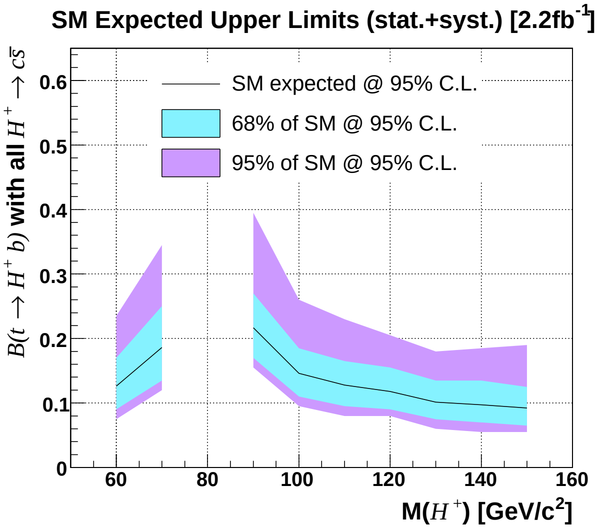

Figure 5.30: The 95% C.L. upper limit on $\mathcal{B}(t \to H^+b)$ including the systematic uncertainties assuming 2.2 fb^{-1} CDF II data sample and null H^+ in the SM. The $\pm 1, 2\sigma$ fluctuations of the upper limit expectations are shown as colored bands.

Chapter 6

Results and Conclusions

We report on the results of the search for a MSSM charged Higgs in top quark decays. Then, we extend the result to include any generic scalar boson production in top quark decays. We conclude this thesis with a discussion of prospects for future searches.

6.1 Results

We observe two hundred lepton+jets $t\bar{t}$ candidates in the 2.2 fb^{-1} data sample collected by the CDF II detector. The dijet mass distribution of the observed $t\bar{t}$ candidates shows a good agreement with the SM expectations (W bosons in $t\bar{t}$ and non-$t\bar{t}$ backgrounds) as shown in Fig. 6.1. Since the number of observed events is larger than the expectations (167 events), the normalizations of the SM events are obtained by the binned likelihood fit assuming no H^+ bosons in the observed dijet mass (number of H^+ events fixed to zero). Note that the LH results are obtained based on the dijet mass templates, which is independent of the assumed $t\bar{t}$ production cross section.

The discrepancy between the observed and expected number of events is expected due to the difference between the assumed SM $t\bar{t}$ production cross section ($\sigma_{t\bar{t}} = 6.7$ pb) and the true $\sigma_{t\bar{t}}$. As estimated in Sec. 4.4, real SM $t\bar{t}$ events are dominant in the selected $t\bar{t}$ candidate, and the $\sigma_{t\bar{t}}$ of 6.7 pb is predicted assuming a top quark mass (m_t) of 175 GeV/c^2. The SM prediction for $\sigma_{t\bar{t}}$ has a linear re-

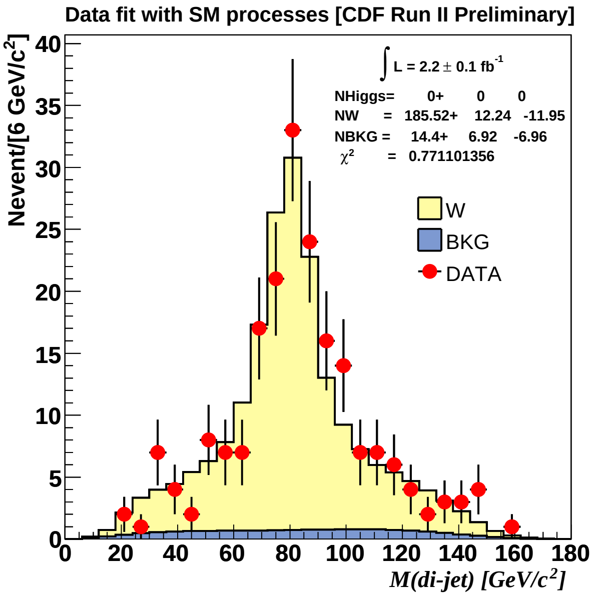

Figure 6.1: Observed dijet mass distribution with the SM expectations in the 2.2 fb^{-1} CDF II data sample.

lation with the m_t as shown in Fig. 6.2; the $\sigma_{t\bar{t}}$ is anticipated to increase by ~0.2 pb for a 1.0 GeV/c^2 decrease in the value of m_t. The current best determination of the top quark mass is 172.4 GeV/c^2 as of August 2008 [82]. The measured m_t corresponds to the $\sigma_{t\bar{t}}$ around 7.2 pb, which is larger than the $\sigma_{t\bar{t}}$ assumption in this analysis. In the mean while, the non-$t\bar{t}$ background is known to be consistent in various $\sigma_{t\bar{t}}$ [77].

Since there is no indication of an anomalous second peak in the observed dijet mass spectrum, we place the upper limits on the $\mathcal{B}(t \to H^+b)$ in Sec. 6.1.1. These limits can also be used as model independent limits because no specific MSSM parameter is used in the analysis. The extension of the analysis to include a search for any generic scalar charged boson production is discussed in Sec. 6.1.2.

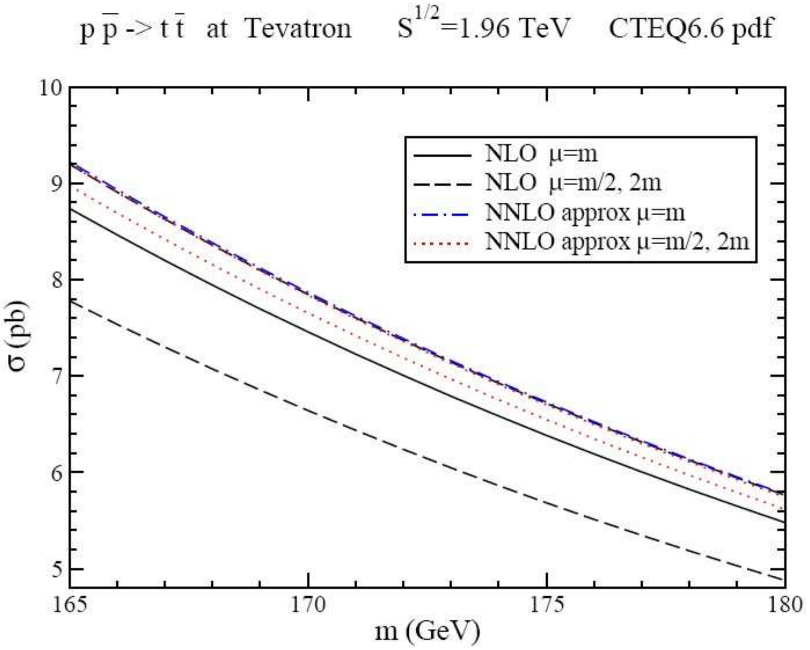

Figure 6.2: Theoretical prediction for the $t\bar{t}$ production cross section at the Tevatron ($\sqrt{s}$ = 1.96 TeV) as a function of top quark mass [83].

6.1.1 Search for $H^+ \to c\bar{s}$ in MSSM

In the framework of MSSM, the charged Higgs boson with a mass below the W mass is already excluded by the direct searches for H^+H^- in electron-positron collisions at LEP [20] (see Sec. 2.4). We perform the first direct search for $H^+ \to c\bar{s}$ in top quark decays for m_{H^+} of 90 to 150 GeV/c^2. The upper limits on the production rate for H^+ in top quark decays ($\mathcal{B}(t \to H^+b)$) are shown in Fig. 6.3. These limits are obtained by the binned likelihood fit to the observed dijet mass spectrum assuming the branching ratio $\mathcal{B}(H^+ \to c\bar{s}) = 1.0$ and $\mathcal{B}(t \to H^+b) + \mathcal{B}(t \to Wb) = 1.0$. The observed limits are consistent with the SM expectations within the uncertainty. Figure 6.4 shows an example dijet mass distribution of 120 GeV/c^2 H^+ bosons, which is normalized by the 95% C.L. upper limit, $\mathcal{B}(t \to H^+b) = 0.1$. We see no evidence of such a H^+ mass peak in 2.2 fb^{-1} CDF II data sample.

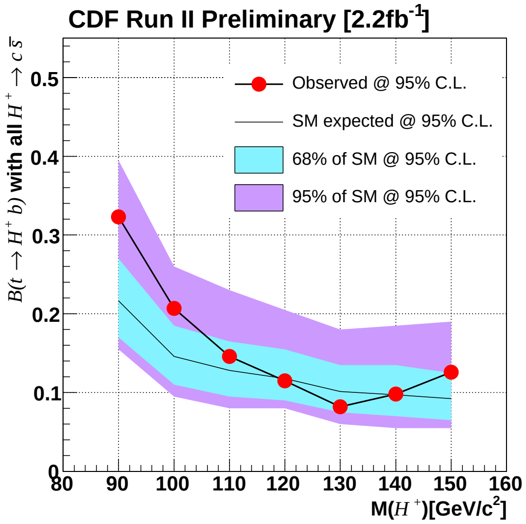

Figure 6.3: Observed 95% C.L. upper limits (dots) on $\mathcal{B}(t \rightarrow H^+b)$ compared with the SM expected upper limits (solid line) with 1, 2 σ uncertainties in 2.2 fb^{-1} CDF II data sample.

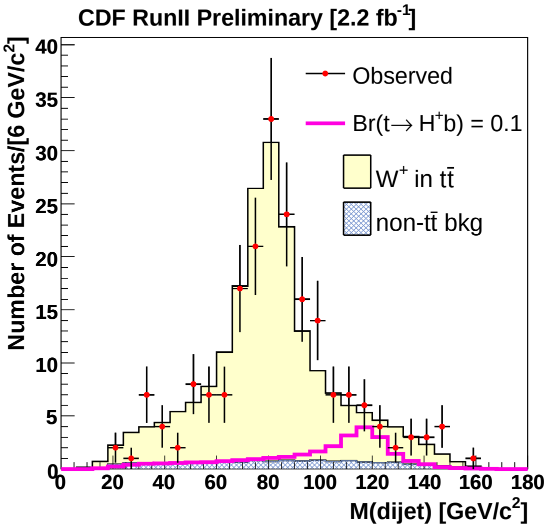

Figure 6.4: Observed dijet mass distribution compared with the SM expectations in 2.2 fb^{-1} data sample. An example of the dijet mass distribution of 120 GeV/c^2 H^+ bosons (bold line) is overlaid assuming $\mathcal{B}(t \rightarrow H^+b) = 0.1$, which corresponds to our 95% C.L. upper limit.

Unfortunately, this analysis is not optimal for improving the exclusion limits in the MSSM parameter plane (m_{H^+}, $\tan\beta$), e.g. Fig. 2.3, because the other H^+ decay channels (shown in Fig. 1.3) are not considered. However, this limitation holds only for MSSM and is not necessarily so in other SUSY models or in non-SUSY frameworks (e.g. Technicolor). As this is the first direct search for this decay mode, we also extract model independent limits that can be used to exclude parameter regions in other models with H^+-like particles.

6.1.2 Model Independent Limit

Our analysis is performed with no assumptions on any specific parameters of the physics beyond the SM except that the scalar boson has a narrow width and $\mathcal{B}(H^+ \to c\bar{s}) = 1.0$. Therefore, the results are model independent, and the upper limits on the branching ratio $\mathcal{B}(t \to H^+ b)$ are also valid for any theoretical model for production of new H^+-like bosons (X^+) in top quark decays.

Assuming a generic scalar charged boson, we extend the search down to m_{H^+} (or X^+ mass) as low as 60 GeV/c^2, lower than the W mass. We also extract the upper limits for other possible hadronic decay channels of the $X^+(\to u\bar{d})$. This extended search is done by using $t \to X^+(\to u\bar{d})b$ PYTHIA MC samples with a X^+ mass of 60, 100, and 120 GeV/c^2. The input parameters to generate the X^+ samples are exactly the same as done for the H^+ samples except for the different hadronic decay mode of the charged boson. Using these light quark hadronic final state samples, we extract upper limits on $\mathcal{B}(t \to X^+ b)$ and compare the results with the limits from the $H^+ \to c\bar{s}$ decay mode.

Study for $X^+ \to u\bar{d}$

The $t \to X^+ b$ analysis follows the same technique used for the $t \to H^+ b$ mode. At first, the selection acceptances for X^+ bosons produced in $t\bar{t}$ events are calculated by applying the same lepton+jets $t\bar{t}$ selection cuts. The acceptances of the $u\bar{d}$ MC samples are listed in Table 6.1 and compared with the acceptances from the $c\bar{s}$ samples. The small difference in the acceptances mostly originates from the two SecVtx b-tagged jets requirement. An additional source of b-tag for $u\bar{d}$ final states can only occur as a result of mistags (false SecVtx tags from light quark-jet). In contrast, a charm quark decay can also make a displaced secondary vertex (e.g. from a long-lived charm hadron) and be tagged as a b-jet. This results in a higher SecVtx tagging efficiency and therefore leads to a somewhat larger acceptance for events with a $c\bar{s}$ decay in the final state.

m_{H^+} [GeV/c^2]	$u\bar{d}$ (%)	$c\bar{s}$ (%)
60	1.823±0.147	2.145±0.272
100	2.079±0.167	2.424±0.305
120	1.936±0.157	2.358±0.291

Table 6.1: Selection acceptances of the $X^+ \rightarrow u\bar{d}$ events and $H^+ \rightarrow c\bar{s}$ events for the charged boson masses of 60, 100, 120 GeV/c^2.

Fig. 6.5 compares the dijet mass distributions in the $u\bar{d}$ decays with the $c\bar{s}$ decays using the MC samples. As mentioned in the Sec. 5.2.2, the dijet mass resolution is correlated with the jet-parton assignment in the $t\bar{t}$ kinematic reconstruction fit. In the $u\bar{d}$ samples, most SecVtx tagged jets are from real b-quarks. Therefore, most of the time the assignment of b-tagged jets to b-quarks is correct, and the other two jets reconstruct the X^+ with a good mass resolution. In contrast, a SecVtx tagged c-jet from the $c\bar{s}$ decays has some probability of being identified as a b-jet (Appendix C.2), which results in an incorrect reconstruction of the H^+ mass. This also contributes to the tails in the dijet mass distribution. Consequently $u\bar{d}$ decays have a better dijet mass resolution than $c\bar{s}$ decays.

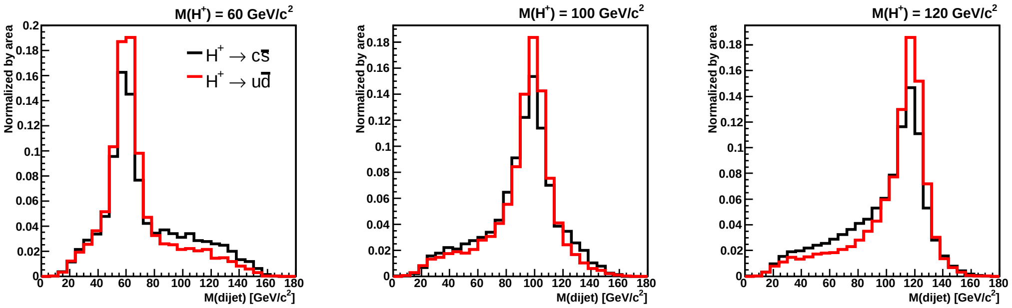

Figure 6.5: Invariant mass distributions of $u\bar{d}$ decays compared with $c\bar{s}$ decays for the charged boson masses of 60, 100, and 120 GeV/c^2.

Upper Limit on $\mathcal{B}(t \to X^+(\to u\bar{d})b)$

The upper limit on $\mathcal{B}(t \to X^+(\to u\bar{d})b)$ is determined using the selection acceptances and mass templates from the $u\bar{d}$ decays instead of those from the $c\bar{s}$ decays. The better mass resolution in the $u\bar{d}$ decays results in a better discrimination between the X^+ boson and the W boson in the dijet mass spectrum. This also results in better upper limits on the production rate of the X^+ bosons in top quark decays. The 95% C.L. upper limits on $\mathcal{B}(t \to X^+(\to u\bar{d})b)$ are compared with the limits on $\mathcal{B}(t \to H^+(\to c\bar{s})b)$ in Fig. 6.6. In general, the upper limits on $\mathcal{B}(t \to X^+(\to u\bar{d})b)$ are roughly 10% lower than the upper limits for $c\bar{s}$ decays. When systematic errors are included, the upper limits are about 25% lower than the upper limits for $c\bar{s}$ decays.

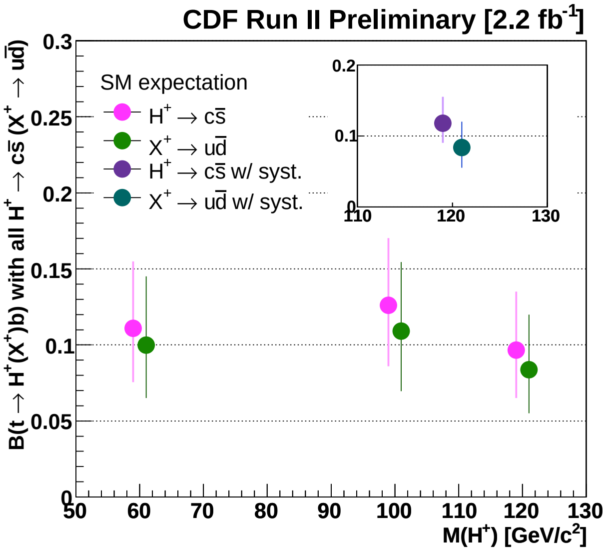

Figure 6.6: 95% C.L. upper limits on $\mathcal{B}(t \to X^+(\to u\bar{d})b)$ compared with the upper limits on $\mathcal{B}(t \to H^+(\to c\bar{s})b)$ for charged boson masses of 60, 100, and 120 GeV/c^2. The inset compares the upper limits with all systematic errors included for the case of 120 GeV/c^2 charged boson.

6.2 Conclusion

We report on the first direct search for non-SM scalar charged boson in decays of top quarks in a CDF II data sample corresponding to an integrated luminosity of 2.2 fb^{-1}. We primarily focus on the $c\bar{s}$ decay mode for the charged Higgs boson in the MSSM prediction. This search is performed by looking for a second mass peak in the dijet invariant mass spectrum. We see no evidence for a charged Higgs boson in the lepton+jets $t\bar{t}$ candidates. Hence, we place the 95% C.L. upper limits for the rate of charged Higgs production in top quark decays.

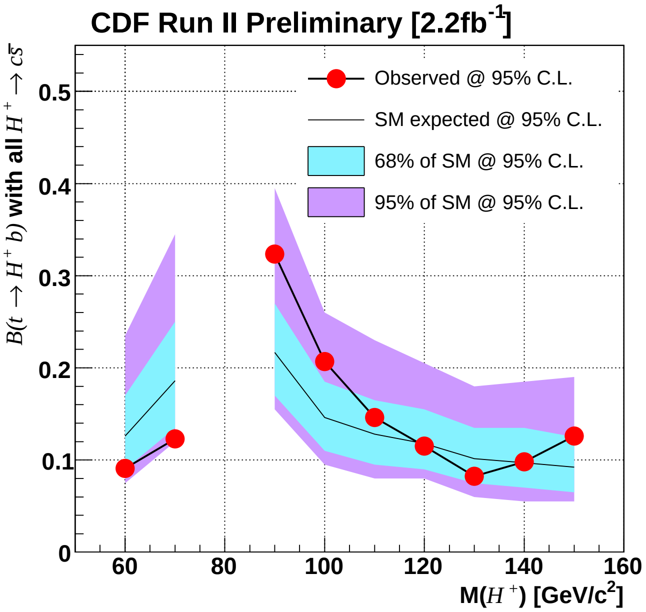

Figure 6.7: Observed 95% C.L. upper limits on $\mathcal{B}(t \rightarrow H^+b)$ (points) in the 2.2 fb^{-1} CDF II data sample compared with the SM expected upper limits (solid line). The 1σ, 2σ uncertainty bands are obtained from a thousand SM pseudo-data sample assuming no H^+ boson.

This analysis is particularly sensitive to a leptophobic charged Higgs model which has the branching ratio $\mathcal{B}(H^+ \rightarrow c\bar{s}) = 1.0$. Such $H^+ \rightarrow c\bar{s}$ decays are predicted in the MSSM for low values of $\tan\beta$ ($\lesssim 1.0$) and also in other models. The upper limits on $\mathcal{B}(t \rightarrow H^+b)$ are obtained in Fig. 6.7 for the H^+ masses of 60 to 150 GeV/c^2, assuming $\mathcal{B}(H^+ \rightarrow c\bar{s}) = 1.0$ and $\mathcal{B}(t \rightarrow H^+b) + \mathcal{B}(t \rightarrow Wb)$

= 1.0. The observed limits in the 2.2 fb^{-1} CDF II data are consistent within the statistical fluctuations of the expected upper limits assuming no new physics beyond the SM.

Since our search is performed without any model specific parameters, the upper limits are valid for any model of non-SM scalar boson production in top quark decays. Assuming a generic dijet decay with the extended search mass down to 60 GeV/c^2, MC simulations show that the upper limits on $\mathcal{B}(t \rightarrow H^+(\rightarrow c\bar{s})b)$ are higher than the upper limits on $\mathcal{B}(t \rightarrow X^+(\rightarrow u\bar{d})b)$. Therefore, the 95% C.L. upper limits in Fig. 6.7 can be viewed as conservative upper limits (better than 95% C.L.) on the production of any anomalous scalar charged boson (which decays to either $c\bar{s}$, or $u\bar{d}$, or a combination of both) in top quark decays.

This analysis is summarized in a paper and released to public via e-print [84]. The paper is to be published in the physics review letter. The content of the paper is attached in Appendix F.

6.3 Future Prospects

The search for charged Higgs in top quark decays is currently statistically limited and can be improved in the future with larger $t\bar{t}$ event samples. In particular, the rapid increase in the integrated luminosity at Tevatron will provide larger event samples. Doubling the amount of data with the CDF II detector would result in 25% lower upper limit than the current limit. The result can be more improved by using a complicated analysis technique, such as floating the Jet Energy Scale in the binned likelihood fit or allowing the selection acceptances to vary within Gaussian error.

In the near future, the higher energy Large Hadron Collider (LHC) will commence its operation. The LHC is a proton-proton collider located at the CERN laboratory in Geneva, Switzerland. The LHC collides protons at a center of mass (CM) energy of fourteen TeV (seven times higher than the Tevatron CM energy) with a target peak luminosity of 2.3×10^{34} $\text{cm}^{-2}\text{s}^{-1}$ (or ×60 of the current peak luminosity of the Tevatron). At the LHC, two experiments (the CMS and ATLAS detectors) are in preparation for collecting the high energy data. At such high energies, the cross section of the $t\bar{t}$ production is predicted to be 833 ± 83 pb (from a QCD next to leading order calculation) as compared to 7.2 pb (estimated from the best measured top quark mass of 172.4 GeV/c^2) at the Tevatron. The large $t\bar{t}$ production rate would allow precision studies of top quark properties as well as the precision measurements of the top quark mass and the production cross section. It would also provides great opportunities for non-SM particle searches associating with the top quark production and decays.

At Tevatron energy the direct production cross section of the charged Higgs is very small (~fb), thus it is very challenging to separate the charged Higgs signal from huge other SM processes such as the large QCD backgrounds. Therefore, we search for a signal in the decays top quarks where the background is much smaller at the Tevatron. However, this search is only relevant for light charged Higgs; i.e. the mass of the charged Higgs is lower than or similar to the mass of the top quark. At LHC energy the direct production cross section of H^+ in association with a top quark is sizable for both light and heavy charged Higgs. Two promising H^+ search channels are shown in Fig. 6.8 [85]: $pp \rightarrow gb \rightarrow tH^-$ and $pp \rightarrow gg \rightarrow tH^-\bar{b}$.

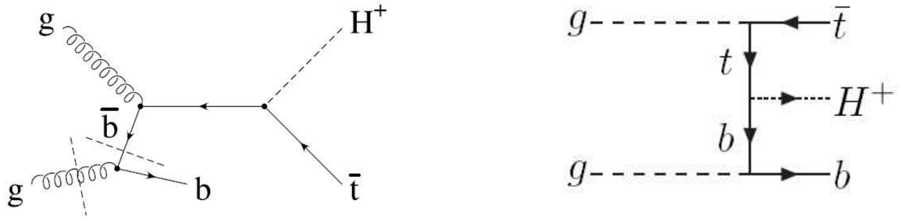

Figure 6.8: Feynman diagrams of two promising channels for H^+ production in association with a top quark in pp collisions at the LHC.

The H^+ search strategy depends on the H^+ decay channel; the decay branching ratios for the MSSM charged Higgs are shown in Fig. 1.3 [8] with two different values of $\tan\beta$. As shown in the figure, $H^+ \rightarrow tb$ is dominant for the heavy H^+, where the m_{H^+} is larger than the mass of the top quark. Therefore signatures of the heavy H^+ production will be $t\bar{t}$ + 1 b-jet (for $gb \rightarrow tH^-$) or $t\bar{t}$ + 2b-jet (for $gg \rightarrow tH^-\bar{b}$). Fig. 6.9 shows the expected production cross section of

$gg \rightarrow tH^-(\rightarrow \bar{t}b)\bar{b}$ in the lepton+jets $t\bar{t}$ final state as a function of m_{H^+}. The signature here is rather clean and consists of a $t\bar{t}$ pair detected in the lepton+jets mode including four b-tagged jets in the event. A feasibility study shows that a statistical significances ($S/\sqrt{B}$) of 3.5 to 12.5 can be achieved (depending m_{H^+}) in the first 100 fb^{-1} of pp collisions [86] at the LHC. The other H^+ production channel, $gb \rightarrow tH^-$, is expected to have a cross section which is approximately three times larger than the tH^-b production cross section.

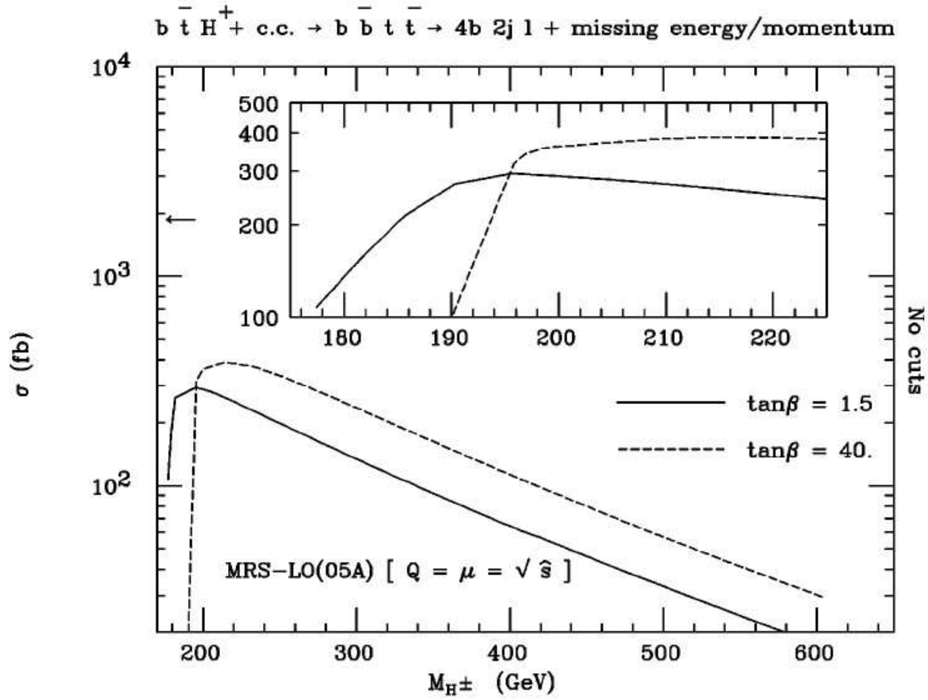

Figure 6.9: Production cross section at the LHC for the $gg \rightarrow tH^-(\rightarrow \bar{t}b)\bar{b}$ process with a final state $l\nu$ + jj + four b-jets as a function of m_{H^+}. The cross section is presented for two values (1.5 and 40) of $\tan\beta$. The cross section around m_{H^+} = m_t is enlarged in the inset. The arrow on the y-axis represents the size of the background.

Figure 6.10 shows the 5σ discovery potential for a H^+ boson with the ATLAS detector [87] assuming 300 fb^{-1} of data ($\sim$ 3 years of data taking at the LHC). Below $m_{H^+} \sim 160$ GeV/c^2, the process $t \rightarrow bH^+(\rightarrow \tau^+\nu)$ provides sensitivity for most of the $\tan\beta$ region. Above $m_{H^+} \sim 175$ GeV/c^2, the $gb \rightarrow bH^-(\rightarrow \tau\bar{\nu})$ provides sensitivity in the high $\tan\beta$ region ($\tan\beta \gtrsim 10$). However, those H^+ decays are sensitive only in $\tan\beta \lesssim 4$ or $\tan\beta \gtrsim 15$. In the intermediate $\tan\beta$ region, charged Higgs decays to SM particles are undetectable, but the SUSY decay daughters can be used as a signature for a H^+ search, $H^\pm \rightarrow \tilde{\chi}^\pm_{1,2}\tilde{\chi}^0_{1,2,3,4} \rightarrow 3l + \not{E}_T$.

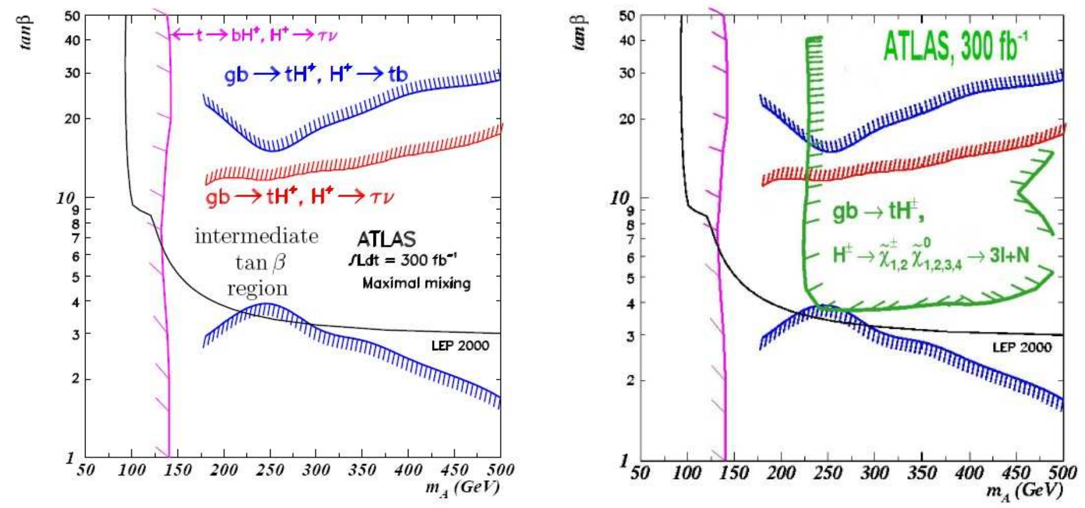

Figure 6.10: The ATLAS LHC 5σ discovery contour for a charged Higgs with SM particles final states (left) and SUSY particles final states (right).

The LHC turn on in late 2009 would provide a unique opportunity to direct search for new particles in the high mass region and new physics beyond the Standard Model. In addition, we will hopefully begin to address the remaining unresolved questions in the SM as well as the mechanism of electroweak symmetry breaking.

Bibliography

[1] S. Glashow, Nucl. Phys. **20**, 579 (1961); S. Weinberg, Phys. Rev. Lett. **19**, 1264 (1967); A. Salam, Elementary Particle Theory, *eds.*: Svartholm, Almquist, and Wiksells, Stockholm, 367 (1968); S. Glashow, J. Iliopoulos, and L. Maiani, Phys. Rev. **D2**, 1285 (1970).

[2] P. W. Higgs, Phys. Lett. **12**, 132 (1964); *idem.*, Phys. Rev. **145**, 1156 (1966); F. Englert and R. Brout, Phys. Rev. Lett. **13**, 321 (1964); G. S. Guralnik, C. R. Hagen, and T. W. B. Kibble, Phys. Rev. Lett. **13**, 585 (1964).

[3] S. L. Glashow and S. Weinberg, Phys. Rev. D **15**, 1958 (1977); J. F. Donoghue and L. F. Li, Phys. Rev. D **19**, 945 (1979).

[4] Marcela Carena and Howard E. Haber, "Higgs Boson Theory and Phenomenology", Prog. Part. Nucl. Phys. **50** 63-152 (2003), arXiv:hep-ph/0208209.

[5] J. S. Lee *et al.*, Comput. Phys. Commun. **156**, 283 (2004), hep-ph/0307377.

[6] R. Eusebi, Ph.D. thesis, University of Rochester, 2005.

[7] M. Carena, S. Heinemeyer, C.E.M. Wagner, and G. Weiglein, “Suggestions for benchmark scenarios for MSSM Higgs boson searches at hadron colliders “, Eur. Phys. J. C26:601-607, 2003.

[8] Nils Gollub, “Top-Quark and Charged Higgs Boson Production at Hadron Colliders, Digital Comprehensive Summaries of Uppsala Dissertations from the Faculty of Science and Technoloty 126.

[9] T. D. Lee and C. N. Yang, “Question of Parity Conservation in Weak Interactions”, Phys. Rev., **104** (1956) 254-258; C. S. Wu, E. Ambler, R. W. Hayward, D. D. Hopper and R. F. Hudson, Phys. Rev. **105**, 1413 (1957).

[10] F. Halzen and A. D. Martin, “QUARKS & LEPTONS”, Published by John Wiley & Sons (1984).

[11] J. F. Gunion, H. E. Haber, G. Kane, and S. Dawson, “THE HIGGS HUNTER’S GUIDE”, Published by Westview Press, 2000.

[12] David McMahon, “Quantum Field Theory Demystified”, Published by McGraw-Hill Professional (2008).

[13] ALEPH, DELPHI, L3, and OPAL Collaborations, The LEP Working Group for Higgs Boson Searches, Eur. Phys. J. **C47**, 547 (2006).

[14] Tevatron New Phenomena & Higgs Working Group, “Combined CDF and D Upper Limits on Standard-Model Higgs-Boson Production”, arXiv:0808.0534v1 [hep-ex].

[15] J. Erler, “SM Precision Constraints at the LHC/ILC”, arXiv:hep-ph/0701261.

[16] C. Amsler *et al.* (Particle Data Group), Phys. Lett. **B667**, 1 (2008). (URL: http://pdg.lbl.gov)

[17] Stephen P. Martin, “A Supersymmetry Primer”, arXiv.org:hep-ph/9709356.

[18] S. Dimopoulos and H. Georgi, “SOFTLY BROKEN SUPERSYMMETRY AND SU(5)”, Nucl. Phys, **B193**, 150-162 (1981).

[19] D. M. Pierce, J. A. Bagger, K. T. Matchev, and R. J. Zhang, “Precision corrections in the minimal supersymmetric standard model”, Nucl. Phys. B **491**, 3 (1997), arXiv:hep-ph/9606211; S, Heinemeyer, W. Hollik, and G. Weiglein, “QCD corrections to the masses of the neutral CP-even Higgs bosons in the MSSM”, Phys. Rev. D **58**, 091701 (1998).

[20] LEP Higgs Working Group (2001), arXiv:hep-ex/0107031v1.

[21] A. Abulencia *et al.* (CDF Collaboration), “Search for charged Higgs bosons from top quark decays in $p\bar{p}$ collisions at $\sqrt{s} = 1.96$ TeV”, Phys. Rev. Lett. **96**, 042003 (2006);

[22] V.M. Abazov *et al.* (DØ Collaboration), “Search for charged Higgs bosons decaying to top and bottom quarks in $p\bar{p}$ collisions”, Fermilab-Pub-08-229-E.

[23] N. Cabbibo, Phys. Rev. Lett., **10** (1963) 531; M. Kobayashi and T. Maskawa, Prog. Theor. Phys., **49** (1973) 652.

[24] K. Ikado *et al.* (Belle Collaboration), “Evidence of the Purely Leptonic Decay $B^- \to \tau^- \bar{\nu_\tau}$”, Belle Preprint 2006-11, arXiv:hep-ex/0604018v3; K. Hara,

"Rare B decay with leptons at Belle", Presented in 34^{th} International Conference on High Energy Physics, Philadelphia, 2008, arXiv:0810.3301v1 [hep-ex].

[25] A.V. Gritsan, "Hot Topics from the BaBar Experiment", SLAC-PUB-12569, Presented in Flavor Physics and CP Violation Conference, Bled, 2007, arXiv:0706.2030v1 [hep-ex].

[26] J. Charles *et al.* (CKMfitter Group), Eur. Phys. J. C **41**, 1 (2005).

[27] M.S. Alam *et al.* (CLEO Collaboration), "Fitst Measurement of the Rate for the Inclusive Radiative Penguin Decay $b \to s\gamma$", Phys. Rev. Lett. **74** (1995) 15.

[28] Cai-Dian Lü, "$b \to s\gamma$ DECAY IN THE TWO HIGGS DOUBLET MODEL", arXiv:hep-ph/950845v1.

[29] http://www.fnal.gov/pub/about/whatis/history.html

[30] http://www.ura-hq.org/about/index.html

[31] S. W. Herb *et al.*, "Observation of a Dimuon Resonance at 9.5 GeV in 400 GeV Proton-Nucleus Collisions," Phys. Rev. Lett. **39**, (1977) 252; Leon M. Lederman, "The Upsilon Particle," Scientific American, **239**, (1978) pp. 72-80.

[32] F. Abe *et al.* (CDF Collaboration), Phys. Rev. Lett. **7**4, 2626 (1995); S. Abachi *et al.* (DØ Collaboration), Phys. Rev. Lett. **7**4, 2632 (1995).

[33] Kodama, K. *et al.* (DONUT Collaboration), "Observation of tau-neutrino interactions," Phys. Lett. **B**504 (2001) 218, arXiv:hep-ex/0012035.

[34] T. Aaltonen *et al* (CDF Collaboration), "First Observation of Electroweak Single Top Quark Production", arXiv:0903.0885v2; V.M. Abazov *et al* (DØ Collaboration), "Observation of Single Top Quark Production", arXiv:0903.0850v1.

[35] T. Aaltonen *et al.* (CDF Collaboration), "First Observation of Heavy Baryons Σ_b and $Sigma_b^*$", Phys. Rev. Lett. 99, (2007) 202001.

[36] http://www.fnal.gov/faw/experimentsprojects/index.html

[37] http://www-bdnew.fnal.gov/operations/rookie_books/Concepts_v3.1.pdf

[38] http://www.fnal.gov/pub/news04/update_archive/update_9-10.html

[39] http://history.fnal.gov/linac.html

[40] http://www-bdnew.fnal.gov/operations/rookie_books/Booster_V3_1.pdf

[41] http://www-boone.fnal.gov

[42] http://www-bdnew.fnal.gov/operations/rookie_books/Main_Injector_v1.pdf

[43] http://www-numi.fnal.gov/

[44] http://www-bdnew.fnal.gov/operations/rookie_books/Pbar_V1_1.pdf

[45] http://www-bdnew.fnal.gov/operations/rookie_books/Recycler_RB_v1.2.pdf

[46] http://www-bdnew.fnal.gov/operations/rookie_books/Tevatron_v1.pdf

[47] http://www-bdnew.fnal.gov/operations/rookie_books/Switchyard_v2.1.pdf

[48] Peter Dong *et al., "Beam Condition Monitoring With Diamonds at CDF", IEEE TRANSACTIONS ON NUCLEAR SCIENCE"* 55 (2008) 328.

[49] www-cdf.fnal.gov/virtualtour.

[50] CDF Collaboration, *"The CDF II detector. Technical Design Report"*, FERMILAB-Pub-96/390-E (1996).

[51] C. S. Hill, *L00: Operational Experience and Performance of the CDFII Silicon Detector*, FERMILAB-CONF-03/412-E (2004); Nucl. Instrum. & Meth A *530* 1 (2004).

[52] A. Sill., *SVX-II: CDF Run II Silicon Tracking Projects*, Nucl. Instrum. & Meth. A **447** 1 (2000).

[53] A. Affolder *et al.*, *ISL: Intermediate Silicon Layers Detector for the CDF Experiment*, Nucl. Instrum. & Meth. A **453** 84 (2000).

[54] T. Affolder *et al.*, Nucl. Instrum. & Meth. A **526** 249 (2004).

[55] L. Balka *et al.*, Nucl. Instrum. & Meth. A **267** 272 (1988).

[56] S. Bertolucci *et al.*, Nucl. Instrum. & Meth. A **267** 301 (1988).

[57] M. Albrow *et al.*, Nucl. Instrum. & Meth. A **480** 524 (2002).

[58] G. Ascoli *et al.*, Nucl. Instrum. & Meth.A268:33,1988 A. Artikov *et al.*. Nucl. Instrum. & Methods A **538** 358 (2005).

[59] D. Acosta *et al.*, Nucl.Instrum. Meth. A **494** 57 (2002); D. Acosta *et al.* Nucl. Instrum. & Meth.A **461** 540 (2001).

[60] D. Acosta *et al.*, Nucl. Instrum. & Meth. A **518** 605 (2004); C. Grozis *et al.* Int. J.Mod. Phys. A16S1C:1119-1121 (2001); C. Paus *et al.* Nucl. Instrum. & Meth. A **461** 579 (2001)

[61] S. Lami, "The CDF MiniPlug Calorimeters at the Tevatron", in proceedings of Frontier Detectors for Frontier Physics, Elba 2003, Italy.

[62] Conceptual Design of a Deadtimeless Trigger for the CDF Trigger Upgrade, CDF internal note 2038.

[63] CDF DAQ Group, "The CDF data acquisition system for Tevatron run II", FERMILAB-CONF-01-242-E, Aug 2001. 4pp.

[64] M. Shimojima *et al.*, "Consumer-Server/Logger System for the CDF Experiment", IEEE Trans. Nucl. Sci. Vol 47, 236 (2000); I. Bizjak *et al.*, "Upgrade of the CDF Run II Data Logger", Real-Time Conference, 2007 15th IEEE-NPSS.

[65] T. Sjostrand *et al.*, Comput. Phys. Commun. **135**, 238 (2001).

[66] A. Borisovich, Thesis (ITEP, Moscow), "Search for Anomalous Production of Events with a High Energy Lepton and Photon at the Tevatron", arXiv:hep-ex/0703011v1.

[67] A. Bhatti *et al.*, Nucl. Instrum. Methods. A **566**, 375 (2006).

[68] F. Abe *et al.* (CDF Collaboration), Phys. Rev. **D** 45, 1448 (1992).

[69] A. Bhatti and K. Hatakeyama, “Relative jet energy corrections using missing E_T projection fraction and dijet balancing”, CDF note 6854.

[70] Christopher Neu, “CDF b-tagging: Measuring Efficiency and False Positive Rate”, in Proceedings of International Workshop on Top Quark Physics, January 12-15, 2006, Coimbra, Portugal.

[71] D. Acosta *et al.*. “Measurement of the $t\bar{t}$ production cross section in $p\bar{p}$ collisions at $\sqrt{s} = 1.96$ TeV using lepton+jets events with secondary vertex b-tagging”, Phys. Rev. **D** 71, 052003 (2005).

[72] J. Freemam, T. Junk, E. Palencia, and S. Grinstein, “SecVtx Mistag Matrices for 2.2 fb^{-1} of Data”, cdf note 9280.

[73] J. Adelman *et al.*, “Method II For You”, CDF note 9185; D. Sherman *et al.*, “Method II Backgrounds for 1.12/fb Lepton+Jets Analyses”, CDF note 8766.

[74] Michelangelo L. Mangano *et al.*, J. High Energy **307** Phys. 001 (2003).

[75] Andrew Ivanov, Tom Schwarz, and Robin Erbacher, “Calibration of Heavy-Flavor Content in W+jets Data”, CDF note 9403.

[76] Johan Alwall, Pavel Demin, Simon de Visscher, Rikkert Frederix, Michel Herquet, Fabio Maltoni, Tilman Plehn, David L. Rainwater and Tim Stelzer, J. High Energy Phys. **0709**, 028 (2007), hep-ph/0706.2334; F. Maltoni and T. Stelzer, J. High Enenrgy Phys.**0302** 027 (2003), hep-ph/0208156

[77] Sherman, Franklin, Grinstein, and Guimarães da Costa, “Measurement of Top Pair Cross Section in Lepton+Jets in 1.12/fb”, CDF note 8767.

[78] A. Abulencia *et al.* (CDF Collaboration), "Top Quark Mass Measurement Using the Template Method in the Lepton+Jets Channel CDF II" , Phys. Rev. **D** 73, 032003 (2006).

[79] A computer program of function Minimization and Error Analysis, F. James, CERN program library.

[80] Nan Yang and Pekka K. Sinervo, "The Effects of Using Top Quark Mass Specific Jet Corrections on the Top Quark Mass Measurement", CDF note 8020; Jean-Francois Arguin in Top Mass Template Working group, http://hep.physics.utoronto.ca/JeanFrancoisArguin/topspec_corr /gen5lev5_corr/ttopel_jetcorr03_nt5.html.

[81] G. Corcella, I.G. Knowles, G. Marchesini, S. Moretti, K. Odagiri, P. Richardson, M.H. Seymour and B.R. Webber, JHEP 0101 (2001) 010 [hep-ph/0011363]; hep-ph/0210213.

[82] The Tevatron Electroweak Working Group, for the CDF, D0 Collaborations, "Combination of CDF and DØ Results on the Mass of the Top Quark", FERMILAB-TM-2413-E, arXiv:0808.1089v1.

[83] M. Cacciari, S. Frixione, G. Ridolfi, M. Mangano and P. Nason, J. High Energy Phys. **404**, 68 (2004); N. Kidonakis and R. Vogt, Phys. Rev. D **68**, 114014 (2003).

[84] CDF Collaboration, "Search for charged Higgs bosons in decays of top quarks in $p\bar{p}$ collisions at $\sqrt{s} = 1.96$ TeV; to be published in Phys. Rev. Lett.

[85] A. Datta, A. Djouadi, M. Guchait, and Y. Mambrini, “Charged Higgs production from SUSY particle cascade decays at the LHC”, arXiv:hep-ph/0107271v1.

[86] D.J. Miller, S. Moretti, D.P. Roy, and W.J. Stirling, “Detecting heavy charged Higgs bosons at the CERN LHC with four b-quark tags”, Phys. Rev. D **61** (2000) 055011.

[87] C. Hansen, N. Gollub, K. Assamagan, and T. Ekelof, “Discovery potential for a charged Higgs boson decaying in the chargino-neutralino channel of the ATLAS detector at the LHC”, Eur. Phys. J, C44S2:1-9(2005), Erratum-ibid, C44S2:11, 2005.

[88] Particles with a superscript (H^+) include the opposite charged particle (H^-), and decay processes such as $t \to H^+b$ imply also their charge conjugate processes.

[89] The t^* is a virtual top quark with an off-shell mass.

[90] T. Affolder *et al.* (CDF Collaboration), Phys. Rev. D **62**, 012004 (2000); F. Abe *et al.* (CDF Collaboration), Phys. Rev. Lett **79**, 357 (1997); V.M. Abazov *et al.* (D0 Collaboration), arXiv:0906.5326 (2009).

[91] A. Abulencia *et al.* (CDF Collaboration), Phys. Rev. Lett. **96**, 042003 (2006); B. Abbott *et al.* (DØ Collaboration), Phys. Rev. Lett **82**, 4975 (1999).

[92] The positive and negative charged weak boson ($W^{\pm}$) is presented as W in this Letter.

[93] In this Letter, the word lepton (l) stands for an electron or a muon. The tau lepton is not referred to as a lepton, but is specified as τ.

[94] The detector uses cylindrical coordinates where θ is the polar angle with respect to the proton beam and ϕ is the azimuthal angle. The direction of a particle in the detector is expressed with the pseudorapidity, $\eta = -\ln\tan(\theta/2)$.

[95] Transverse energy is $E_T = E\sin\theta$, where E is the measured energy. Transverse momentum, p_T, of charged particles, is calculated similarly. From energy-momentum conservation, $\sum_i E_T^i \hat{n}_i = 0$ for radial unit vector $\hat{n}_i$ in the azimuthal plane. Missing transverse energy is defined as $-\sum_i E_T^i \hat{n}_i$, representing undetected particles such as neutrinos. The missing E_T is further corrected for the energy and momentum of identified muons.

[96] Daniel B. Rowe, *Multivariate Bayesian Statistics* (CRC, Chapman & Hall, 2003), p117.

Appendix A

Neutrino Longitudinal Momentum

As described in Sec. 4.2.4, the imbalance in the transverse energy is used as a measurement of the neutrino's transverse momentum. However, we have no measurement of the longitudinal component. The neutrino's longitudinal momentum (p_z^ν) is mathematically determined (with two solutions) when we constrain the mass of the W that decays leptonically in the $t\bar{t}$ reconstruction fit (See Sec. 5.1). The longitudinal component is calculated using the invariance of the Lorentz transformation; inner product of the four-vector sum before and after the decay process should be equal. For $W \rightarrow e/\mu + \nu$ decays, the W boson mass is an invariant quantity. The four-vectors of the W, the lepton (l), and the neutrino (ν) are represented as

$$(E^l + E^\nu, p_x^l + p_x^\nu, p_y^l + p_y^\nu, p_z^l + p_z^\nu) \quad \text{for} \quad W^+ \text{ boson,} \tag{A.1}$$

$$(E^l, p_x^l, p_y^l, p_z^l) \quad \text{for} \quad \text{a lepton,} \tag{A.2}$$

$$(E^\nu, p_x^\nu, p_y^\nu, p_z^\nu) \quad \text{for} \quad \text{a neutrino,} \tag{A.3}$$

where E^ν is the neutrino energy ($= \sqrt{p_x^{\nu 2} + p_y^{\nu 2} + p_z^{\nu 2}}$). The masses of the lepton and the neutrino are significantly smaller than the W boson mass and can be ignored.

The missing longitudinal component of the neutrino momentum, p_z^ν, is calculated as follows:

$$(E^l + E^\nu)^2 - (p_x^l + p_x^\nu)^2 - (p_y^l + p_y^\nu)^2 - (p_z^l + p_z^\nu)^2 = m_W^2 \tag{A.4}$$

$$E^l E^\nu - p_x^l p_x^\nu - p_y^l p_y^\nu - p_z^l p_z^\nu = \frac{1}{2} m_W^2 \tag{A.5}$$

$$E^l \sqrt{p_t^{\nu 2} + p_z^{\nu 2}} = \alpha + p_z^l p_z^\nu \tag{A.6}$$

$$\alpha = \frac{1}{2} {m_W}^2 + p_x^l p_x^\nu + p_y^l p_y^\nu, \ {p_t}^2 = {p_x}^2 + {p_y}^2$$

$$(E^{l2} - {p_z^l}^2) p_z^{\nu 2} - 2\alpha p_z^l p_z^\nu + E^{l2} p_t^{\nu 2} - \alpha^2 = 0 \tag{A.7}$$

The quadratic equation (A. 7) yields two solutions for p_z^ν:

$$p_z^\nu = \frac{\alpha p_z^l \pm \sqrt{\alpha^2 {p_z^l}^2 - (E^{l2} - {p_z^l}^2)(E^{l2} p_t^{\nu 2} - \alpha^2)}}{E^{l2} - {p_z^l}^2}. \tag{A.8}$$

Appendix B

Jet Identification Algorithm

In Monte Carlo events, reconstructed jets in the calorimeter (calorimeter jets) can be matched with the parent partons at the generator level since the origin of the jets is known. The jets are processed through hadronizations, and may co-mingle with gluon jets from QCD initial state radiations ISR. In addition to the initial state quarks, final state high energy quarks, e.g. tree-level quarks produced in $t\bar{t}$ decays, can also radiate gluons (FSR). Simply matching the calorimeter jets to tree-level parton cannot be applied to the radiated jets or to quark jets which are deflected after radiation. Therefore a jet identification algorithm has been developed using intermediate jets.

Jets are clustered in three stages depending on the particle information used for the jet reconstruction: parton jets, particle jets, and calorimeter jets (Fig. 4.3). In Monte Carlo events the first two kinds of jets can be reconstructed by using generator level particle information provided by the event generator. Thus those jets are available in simulation samples only. The parton jets are clustered with particles which directly fragmented from the tree-level quarks. Particle jets are formed from final stable hadrons after the hadronization process. While calorimeter jets are clustered using the deposited energies in the calorimeter towers, parton and particle jets use the four momenta of the particles. All jets used in this analysis are reconstructed with a cone size (ΔR) of 0.4.

The MC simulation samples provide the particle ID, mothers and daughters, and status of the decaying process of generated events. The status index is important to filter the particle candidates for the parton and particle jet clustering. The PYTHIA program uses `stdhep` for the status index. A particle with `stdhep` = 3 is the tree-level particle, which yields daughter particles with `stdhep` = 1 or 2. A particle with `stdhep` = 2 yields an intermediate decaying process and decays into either other intermediate state particles with `stdhep` = 2 or a stable particles with `stdhep` = 1. After the decaying process all the intermediate particles end as stable particles (`stdhep` = 1). The parton jets are reconstructed using the particles with `stdhep` = 2 which have a direct mother with `stdhep` = 3. However, particle jets use only stable particles with `stdhep` = 1.

Table B.1 lists an example of the generated particles for a $t\bar{t}$ event in a PYTHIA H^+ MC sample. In the colliding $p\bar{p}$ (ID = 2212, -2212), a u-quark (ID = 2) from the proton and a $\bar{u}$-quark (ID = -2) from the antiproton undergo a hard collision resulting in the production of a $t\bar{t}$ (ID = 6, -6) pair. The top quark (index = 6) decays to a b-quark (ID = 5) and a H^+ (ID = 37, index = 8), which further decays to $c\bar{s}$ (ID = 4, -3). The antitop quark (index = 7) decays to a $\bar{b}$-quark (ID = -5) and a W (ID = -24, index = 17), which decays to $\mu\bar{\nu}$ (ID = 13, -14). Since the final state $\mu\bar{\nu}$ includes two stable particles, the process ends quickly (index = 18, 19). However, the initial and final state quarks generate many gluons (ID = 21) in their hadronizations. Through a long list of intermediate particles, the generated quarks end up as stable particles, e.g. π^0(ID = 111) $\rightarrow \gamma\gamma$(ID = 22), $\pi^+\pi^-$ (ID = 211, -211), or K^0_L (ID = 130) in indices 501-506.

To identify the origin of the jets in the calorimeter, the parton jets and the particle jets must be identified first. Even in the generate-level, the parton jets and particle jets do not originate from only one source. The mother of a jet is determined by the energy weight of each jet component; a parton that contributes the largest energy portion of the jet is assigned as the mother. Figure B.1 shows the angular distance between a particle jet and its mother parton jet. Since the leading four jets are required to originate from final state partons in lepton+jets $t\bar{t}$ events, the fifth energetic jet is supposed to be a QCD radiated jet. We find that the origin of a fifth radiated jet can be found as it is usually emitted within a reasonably small angular cone as compared to the jet cone size of 0.4.

Index	ID	Stdhep	Mo1	Mo2	Index	ID	Stdhep	Mo1	Mo2
0	2212	3	0	0	21	21	2	9	0
1	-2212	3	0	0	22	21	2	9	0
2	2	3	0	0	23	-1	2	9	0
3	-2	3	1	0	24	1	2	9	0
4	2	3	2	0	25	21	2	0	0
5	-2	3	3	0	26	21	2	0	0
6	6	3	4	5	27	21	2	2	0
7	-6	3	4	5	28	21	2	2	0
8	37	3	6	0	29	21	2	2	0
9	5	3	6	0	30	21	2	2	0
10	-24	3	7	0	31	21	2	2	0
11	-5	3	7	0	32	2103	2	0	0
12	-3	3	8	0	33	-5	2	11	0
13	4	3	8	0	34	21	2	11	0
14	13	3	10	0			. . .		
15	-14	3	10	0	501	211	1	172	0
16	37	2	8	0	502	-211	1	172	0
17	-24	2	10	0	503	111	2	172	0
18	13	1	14	0	504	130	1	500	0
19	-14	1	15	0	505	22	1	503	0
20	5	2	9	0	506	22	1	503	0

Table B.1: List of generated particles in a $t\bar{t}$ event ($t \to H^+(\to c\bar{s})b$, $\bar{t} \to W(\to \mu\bar{\nu})\bar{b}$) in a PYTHIA MC sample. Listed are each particle's ID, status (`stdhep`), and indices of the mother particles in order of procedure. The particle ID follows the standard numbering scheme [16].

The origin of the calorimeter jet follows the mother of the closest particle jet. The ΔR between the calorimeter jet and the matched mother particle jet is shown in Fig. B.2. The ΔR(calorimeter jet, particle jet) is larger than ΔR(particle jet, parton jet). This is understood because the measured energy in the detector is smeared over a larger region in space. Usually softer jets are smeared more than harder jets because the lower energy charged particles are bent more in the magnetic field[1] and more energy is lost in the jet reconstruction with a fixed cone

---

[1] A charged particle traverses a circle in a uniform magnetic field. The radius (ρ) of the circle is determined as $\rho = \frac{p}{qB}$, where B is strength of the magnetic field and q is the electric charge. Thus softer particle with low momentum (p) follows sharper curve and spreads further out.

size (See Sec. 4.2.3). Therefore, the ΔR between the fifth energetic calorimeter jet and its mother particle jet is worse than the that ΔR for the the leading jet.

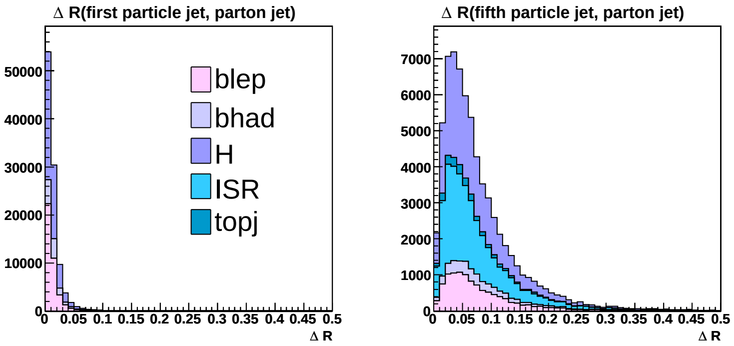

Figure B.1: Angular distance (ΔR) between a particle jet and its mother parton jet in a 120 GeV/c^2 H^+ sample. Left plot shows the ΔR between the most energetic jets with its initial parton, and the right plot show the same quantity for the fifth jet.

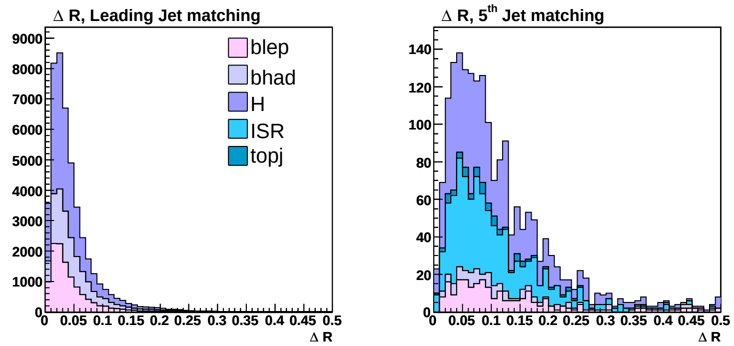

Figure B.2: Angular distance (ΔR) between a calorimeter jet and its mother particle jet for different jets in a 120 GeV/c^2 H^+ MC sample. Left plot shows the ΔR for matching of the leading four jets and the right plot shows ΔR for the fifth jets.

Appendix C

b-jet Assignment Study

We investigate how often a b-tagged jet originates from a real b-quark and how often a tagged b-jet is assigned to the correct b-quark. Since the b-tagged jets are forced to be assigned to the b-quarks, any mistagged jet will be assigned incorrectly and lead to a broad reconstructed m_{H^+} mass distribution. In particular the hard c-quark originating from the decay of a heavy H^+ boson may end up as b-tagged. If the selected event has more than two b-tagged jets, the kinematic fitter would assign the b-jet based on the minimum χ^2 in the $t\bar{t}$ reconstruction. Therefore, if any assigned b-jet is actually a mistagged jet, a wrong H^+ mass is reconstructed.

In order to reduce the number of wrong jet assignments that result from a mistagged jet, we attempt to release the tagging information of the less significant b-tagged jet if the χ^2 is greater then a certain value (as described below). The fitter then treats a double b-tagged event as a single b-tagged event. In such a case, the smallest χ^2 should in principle select the most probable jet-parton assignment without being affected by a bias from the mistagged jet. To select the most significant b-tagged jet in an event, we test four different methods. At the end, an algorithm is judged to be a better algorithm only if the final extracted upper limit on the H^+ production cross section is found to be smaller. Unfortunately, the methods which were investigated and described below did not satisfy this criteria.

C.1 Selection of the Most Significant *b*-jet

The kinematic fitter checks whether each jet is *b*-tagged or not before assigning it to a *b*-quark. Treating a double *b*-tagged event as a single *b*-tagged event is simply done by ignoring the tagging information for the less significant *b*-tagged jet. The question is how to select the less or more significant *b*-tagged jet. Four methods of using the secondary vertex information are considered in selecting the most probable potential *b*-jet. For each of the four methods the most probable *b*-jet in a two or more *b*-jets samples remains as a *b*-jet under following condition:

1. $L_{2D}/\sigma_{L_{2D}}$ (SecLxy) is larger (See Sec. 4.2.3)
2. Mass of the secondary vertex is larger (SecMass)
3. Linear sum of scaled $L_{2D}/\sigma_{L_{2D}}$ and secondary vertex mass is larger (Lxy+Mass)
4. *b*-jet energy correction is smaller (SecVal).

The last condition is based on the assumption that the kinematic fitter would require a larger energy correction to a jet when it is assigned to a wrong parton. Figure C.1 shows the jet identification of the selected most significant *b*-tagged jet. The three methods (except for the SecVal) select the real *b*-jet with a similar efficiency. Here we describe a sensitivity study using the first method (SecLxy) for which the *b*-tagged jet with the largest SecLxy is assigned to a *b*-quark and the other tagged jets in the event are ignored (but only for events with $\chi^2 > 7$).

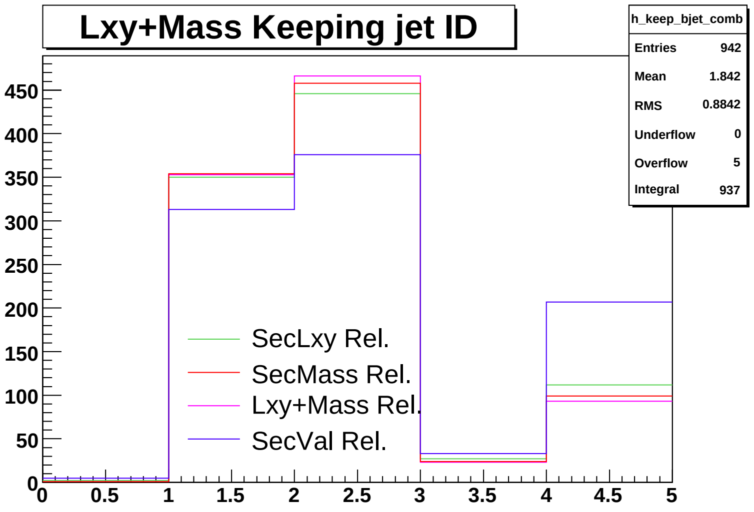

Figure C.1: Jet identification of the most significant b-jet in the events with $\chi^2 > 7$. This test is performed with the 120 GeV/c^2 H^+ MC sample. Events in bin 2 and 3 are the confirmed b-jets from leptonic side b-quarks(1) and hadronic side b-quark s(2), respectively, whereas bin 4 and 5 are jets from Higgs decays (3: s-jet, 4: c-jet). Events in bin 0 are radiated jets.

C.2 B-jet Assignment Check

The procedure of b-jet re-assignment is done as following:

1. Run the $t\bar{t}$ reconstruction fitter with two (or more) b-tagged jets which we refer to as the preliminary fit (pre-fit).

2. If the χ^2 from the pre-fit is greater than a certain value (here we use 7), keep only one b-tagged jet which has the largest SecLxy and release the other b-tagged jet(s).

3. Rerun to the reconstruction fitter as a single b-tagged jet event, which we refer to as the secondary fit (sec-fit).

Table C.1 shows the various correct and incorrect jet assignments from the preliminary and the secondary fits for different sources of h-jets. Here events with exactly four jets, identified as decay jets from tree-level partons in the $t\bar{t}$ decay

Samples	120 GeV/c^2 H^+				150 GeV/c^2 H^+			
N(b-jet)	$= 2$		> 2		$= 2$		>2	
χ^2	< 7	> 7	< 7	> 7	< 7	> 7	< 7	> 7
good H^+	3133	331(82,249)	254	10(6,4)	902	125(27,98)	75	5(2,3)
wrong H^+	838	261(145,116)	349	26(6,20)	293	111(53,58)	131	18(5,13)
($c \rightarrow$ blep)	129	84(51,33)	36	2(0,2)	41	49(29,20)	19	3(0,3)
($c \rightarrow$ bhad)	378	38(12,26)	205	7(3,4)	141	9(1,8)	83	5(2,3)
($s \rightarrow$ blep)	10	17(12,5)	7	1(1,0)	9	5(4,1)	1	1(1,0)
($s \rightarrow$ bhad)	31	7(3,4)	18	1(0,1)	33	3(1,2)	6	5(1,4)
(other)	290	115(67,48)	83	15(2,13)	69	45(18,27)	22	4(1,3)

Table C.1: The $t\bar{t}$ samples with exactly four jets are divided based on the number of b-jets in the event and the χ^2 from the pre-fit. Left column shows correct Higgs jet assignment (good H^+), b-jet contamination in Higgs (wrong H^+), and the subclasses of wrong assignment in parenthesis, e.g. c-jet replaced by leptonic side b-jet ($c \rightarrow$ blep). The number of events in each category is listed. Here, the numbers in parenthesis are the (correct,wrong) assignment from the secondary χ^2 fit.

(good leading jets), with at least two b-tagged jets are used. In the 120 GeV/c^2 and 150 GeV/c^2 Higgs MC samples, 87% and 73% of the total number of events have four good leading jets, respectively.

It is noticed that the χ^2 value for the wrong assignment (c-jet → bhad) is already small. Therefore the gain from the sec-fit is expected to be small. In addition, more than a half of the correctly assigned Higgs jets with $\chi^2 > 7$ in the pre-fit are wrongly assigned in the sec-fit, whereas half of the wrongly assigned events in the pre-fit end up with the correct combination in the sec-fit. Nevertheless, the Higgs mass distribution from the sec-fit is narrower than the mass distribution of the pre-fit for events with $\chi^2 > 7$, as shown in Fig. C.2.

C.3 Improvement in the Upper Limit

Finally the improvement from the b-jet re-assignment is evaluated to see if it results in a lower cross section limit. A new template is constructed using the dijet mass from the pre-fit for events with $\chi^2 < 3 \sim 10$ and from the sec-fit for events with larger χ^2. The upper limit on the H^+ production cross section with the new template is compared with the upper limit using pre-fit template only as

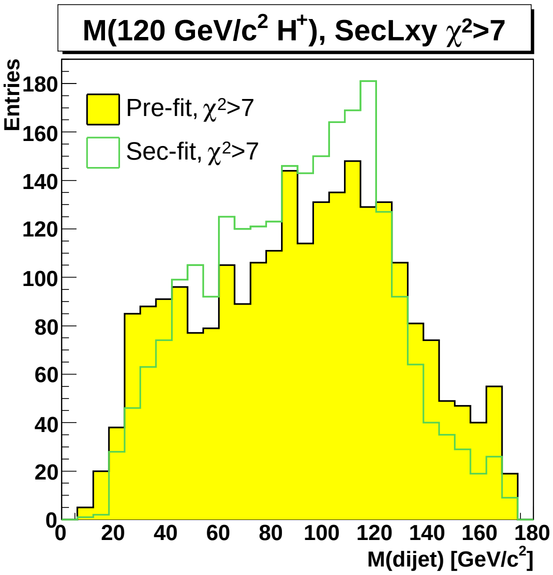

Figure C.2: Dijet mass distribution from the secondary fit (green) compared with the mass distribution from the preliminary fit (black) for events with $\chi^2 > 7$ in the 120 GeV/c^2 H^+ MC sample.

shown in the Fig. C.3. Regardless of the χ^2, the new limit results are similar or worse than the previous limit (dashed line in the Fig. C.3). This indicates that the mass distinction between H^+ and W in the new templates is worse than before. In addition, this new selection criteria brings in an additional source of systematic uncertainty. Therefore we have decided not to use the sec-fit algorithm.

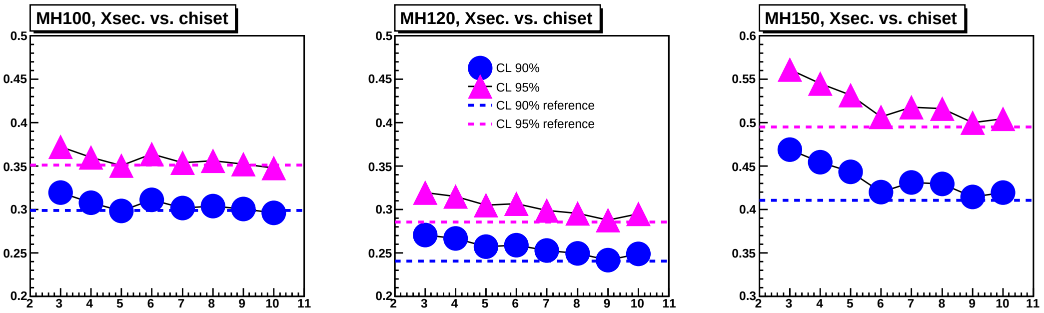

Figure C.3: The cross section upper limits on the H^+ production with 90% (blue) and 95% (magenta) C.L. Markers represent cross section limits from new template using the preliminary fit for events with $\chi^2 < 3 - 10$(x-axis) and the secondary fit for events with larger χ^2. The dashed lines show cross section limit using the template from the pre-fit only. The limits are estimated for 100 GeV/c^2, 120 GeV/c^2, and 150 GeV/c^2 Higgs sample, respectively.

Appendix D

Study of a Possible χ^2 Cut

One could possibly reject events with wrong jet-parton assignment and also reject backgrounds by removing events with a large reconstruction χ^2. Events with a large χ^2 are from poor $t\bar{t}$ reconstruction, and thus may contribute to the tails of the dijet mass distributions. Figure D.1 shows two dimensional plots of χ^2 versus hadronic side top mass (m_t) on the left, and versus H^+ mass (m_{H^+}) on the right. The high-end χ^2 cut may be useful for the case of a top quark mass measurement. This is because of the "U" shape in the plot (large and small m_t tends to have bigger χ^2). In fact the template for the measurement of the top mass selects only events with χ^2 less than 9 [78]. However, for a H^+ search in the dijet mass spectrum we do not gain much from a χ^2 cut because of the flat χ^2 distribution.

The upper limit on the H^+ production cross section is studied using various χ^2 cuts as shown in Fig. D.2. We find that any χ^2 cut does not provide a better limit as compared to the case of no χ^2 cut (for any m_{H^+}). This indicates that there is only a small number of background events in the double b-tagged sample and the χ^2 cut remove more signal events than background.

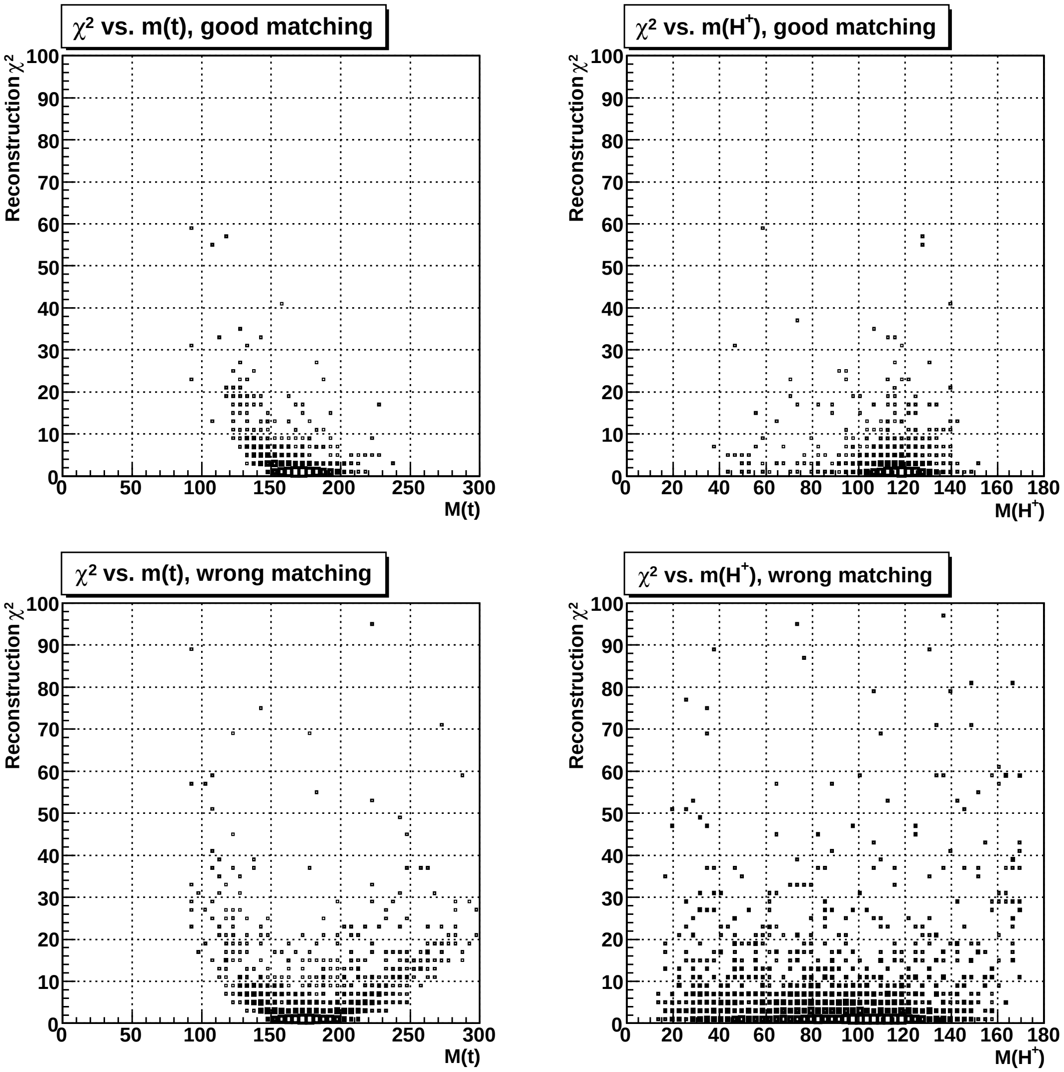

Figure D.1: Reconstruction χ^2 versus reconstructed top quark mass in the hadronic side (left) or reconstructed H^+ mass (right). To see the effect of χ^2 on the invariant mass, the 120 GeV/c^2 H^+ MC sample is divided into good jet-parton matching (top) and wrong matching (bottom) events. Note that for the case of a top quark mass measurement m_t is reconstructed without fitter correction (m_t is constrained to 175 GeV/c^2 in the the kinematic fitter for the case of a H^+ mass measurement), and the χ^2 is obtained after the full kinematic fit.

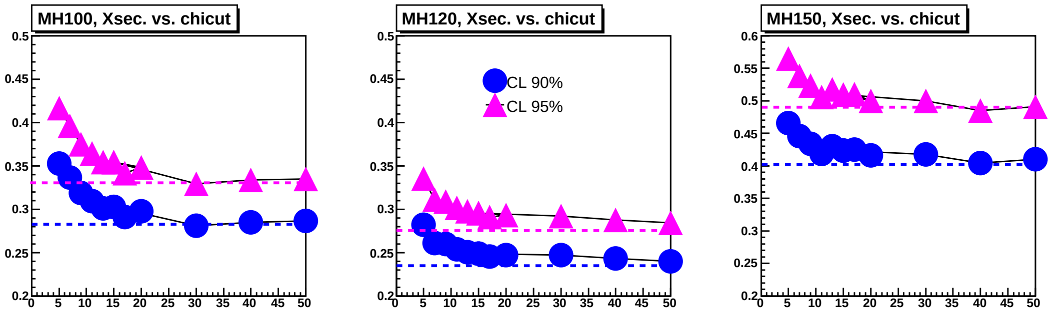

Figure D.2: Upper limits on the H^+ production cross section with 90% (blue) and 95% (magenta) C.L. as a function of χ^2 cuts for 100, 120, and 150 GeV/c^2 H^+ samples. The dashed line represents the upper limits without a χ^2 cut.

Appendix E

Likelihood Tests

E.1 Integrity Check

The integrity of the likelihood fit is tested as follows:

(1) The likelihood fit should return the same results regardless of the assumed H^+ mass for the case of a null-Higgs hypothesis. This has been discussed earlier and the results are shown in Fig. 5.14.

(2) The likelihood fitter should return expected results. For this, five pseudo-experiment (PE) data sets are generated; each set consists of a thousand pseudo experiments which include 0, 2, 5, 10, and 20 H^+ events in the sample distribution; the number of observed $t\bar{t}$ candidates after subtraction of the non-$t\bar{t}$ backgrounds is required to be equal to $N_{H^+} + N_W$. The input $\mathcal{B}(t \to H^+b)$ is calculated for each assumed m_{H^+} separately. The non-$t\bar{t}$ backgrounds are Gaussian constrained to the estimated numbers as discussed in the Sec. 4.4. Figure E.1 shows that output $\mathcal{B}(t \to H^+b)$ results agree with the input $\mathcal{B}(t \to H^+b)$ within a 1σ error regardless of the H^+ mass.

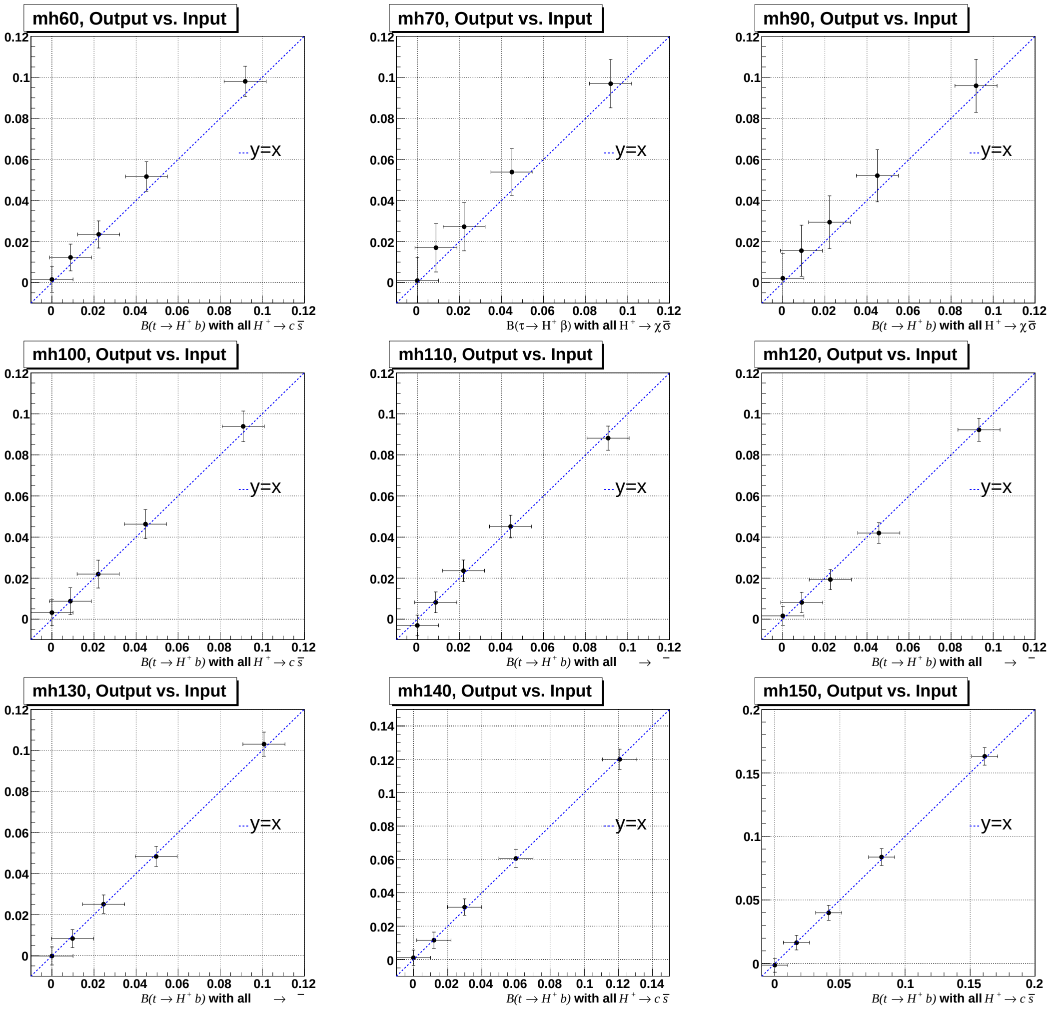

Figure E.1: Output $\mathcal{B}(t \to H^+b)$ of the LH fit versus input $\mathcal{B}(t \to H^+b)$ of the pseudo-experiments for templates with H^+ masses of 60 GeV/c^2 to 150 GeV/c^2 .

E.2 Stability Check

The templates used in the likelihood fit are normalized based on the estimated number of events as discussed in Sec. 4.4. This stability check is designed to test the likelihood for the case that the true composition of the observed dijet mass is different from expectations. Here eleven sets of pseudo-experiments are investigated as listed in Table E.1[1]. All the MC samples do not include H^+ events.

Set	N_W	N_{bkg}	Misc.
0	147.9±12.2	13.52±3.2	Normalized number of events in templates $t\bar{t}$ cross-section of 6.7 pb is assumed.
1	157.92	13.52	
2	167.92	13.52	
3	177.92	13.52	
4	187.92	13.52	
5	197.92	13.52	
6	187.92	9.52	
7	187.92	16.52	
8	187.92	9.52	N_{bkg} is not constrained.
9	187.92	16.52	N_{bkg} is not constrained.
10	147.92	13.52	N_{bkg} is not constrained.

Table E.1: Pseudo-experiments sets with various combinations of W and N_{bkg}. Each set contains a thousand pseudo-experiments, generated by bin-to-bin Poisson fluctuations in the number of events in the templates. All MC samples include no H^+ events.

Figures E.2 - E.4 show following four plots: (1) pull distribution (mean of output $\mathcal{B}(t \to H^+b)$ from the LH fit), (2) the upper limit on $\mathcal{B}(t \to H^+b)$, (3) mean of output non-$t\bar{t}$ background, and (4) the χ^2 after the LH fits. We conclude: (1) The pull distribution shows consistent null-Higgs results within 0.1 σ. This result clearly demonstrates that the LH fitter returns consistent outputs regardless of the composition of the input event (W or non-$t\bar{t}$ background). (2)

---

[1] We are aware that the normalizations of the W and non-$t\bar{t}$ distributions are slightly different from the estimations in Sec. 4.4. This is accidentally happened in the study, and it should not affect the integrity of the results of this test.

With consistent null-Higgs pseudo-experiments, an increasing number of W is reflected as smaller limits on $\mathcal{B}(t \to H^+b)$ for pseudo-experiment set 0-5. However, these limits are consistent within a 1σ uncertainty. (3) The number of non-$t\bar{t}$ backgrounds ($N_{\rm bkg}$) is Gaussian constrained in the fit. It should be noted that the LH fitter returns a value for the expected $N_{\rm bkg}$ (plot (3) among sets 8-10) and gives reasonable upper limits (plot (2) among sets 8-10) without using the Gaussian constraint. Also a small change in input N_{bkg} does not affect the upper limits (plot(2) among sets 5-10). This implies that the Gaussian constraint on $N_{\rm bkg}$ does not change the final results for the upper limits on $\mathcal{B}(t \to H^+b)$. (4) The LH fits for all the pseudo-experiments yield reasonable χ^2 values.

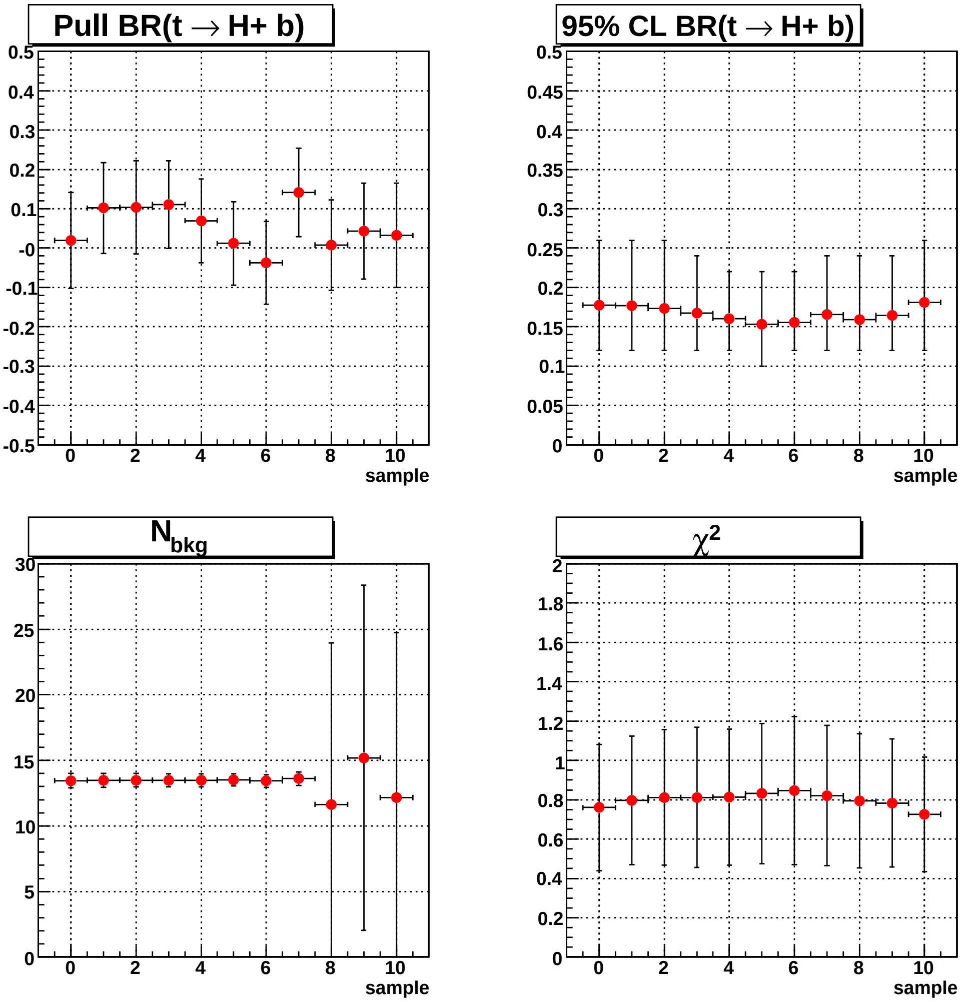

Figure E.2: From left top, the results of pull $\mathcal{B}(t \to H^+b)$, upper limit on $\mathcal{B}(t \to H^+b)$, number of non-$t\bar{t}$ backgrounds, and χ^2 of the LH fit. Fits are performed with 90 GeV/c^2 H^+ MC templates.

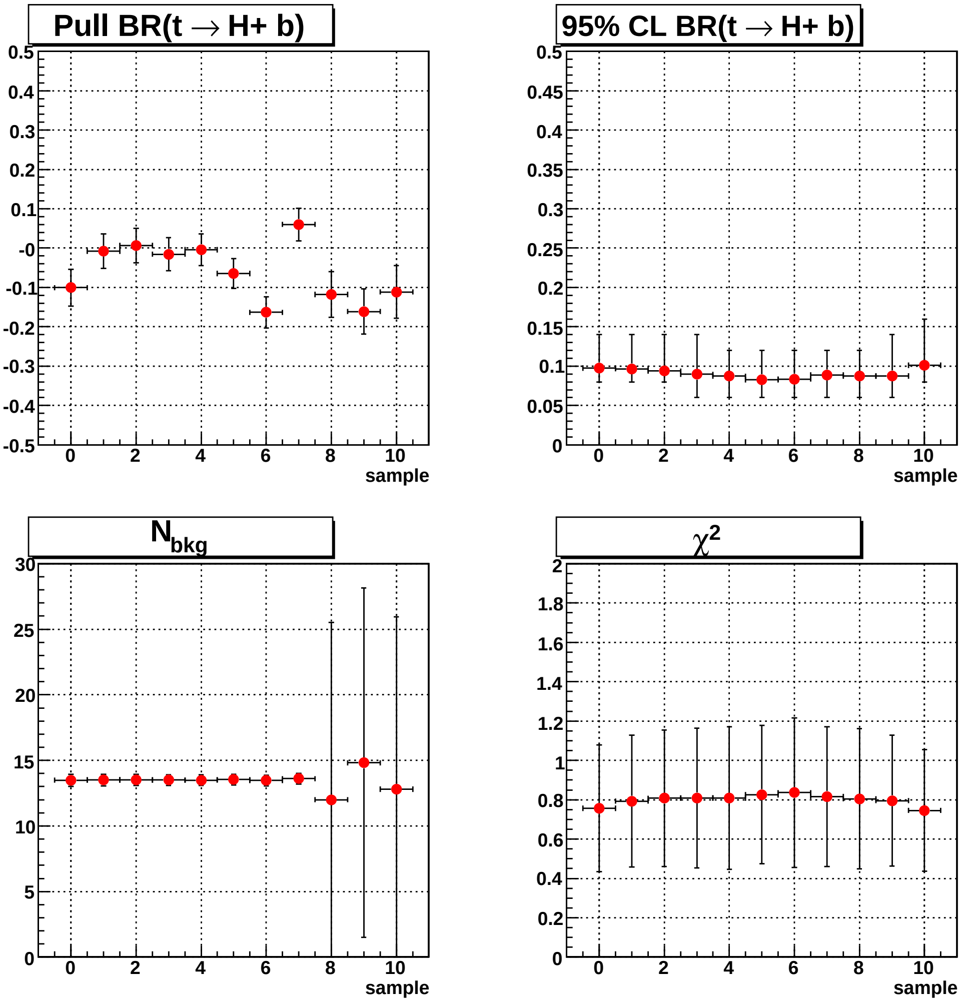

Figure E.3: From left top, the results of pull $\mathcal{B}(t \to H^+b)$, upper limit on $\mathcal{B}(t \to H^+b)$, number of non-$t\bar{t}$ backgrounds, and χ^2 of the LH fit. Fits are performed with 120 GeV/c^2 H^+ MC templates.

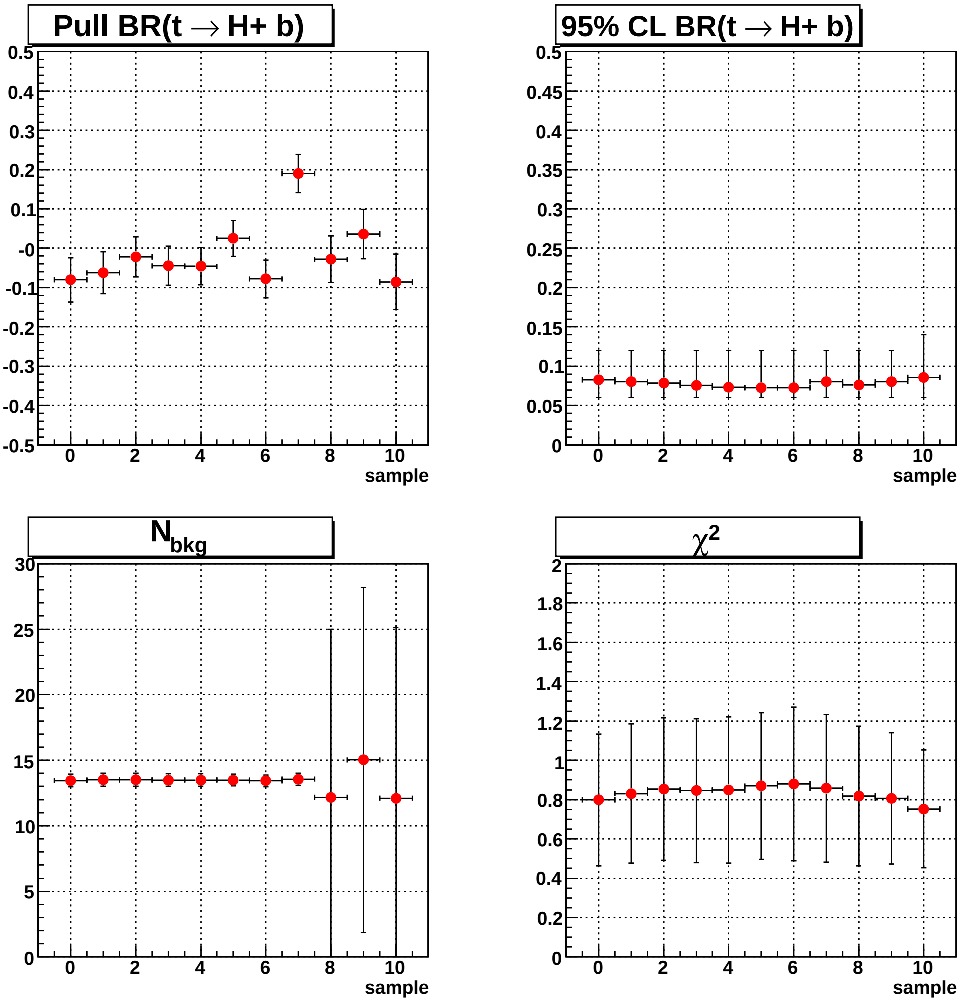

Figure E.4: From left top, the results of pull $\mathcal{B}(t \to H^+b)$, upper limit on $\mathcal{B}(t \to H^+b)$, number of non-$t\bar{t}$ backgrounds, and χ^2 of the LH fit. Fits are performed with 150 GeV/c^2 H^+ MC templates.

Appendix F

Physical Review Letter

The standard model (SM) is remarkably successful in describing the fundamental particles and their interactions. Nevertheless, it is an incomplete theory. An important unresolved question is the mechanism of electroweak symmetry breaking (EWSB). In the SM, a single complex scalar doublet field breaks the symmetry, resulting in massive electroweak gauge bosons and a single observable Higgs boson [2]. To date, the Higgs boson has not been discovered, and consequently the mechanism of EWSB remains in question.

Beyond the SM, many diverse hypotheses with extended Higgs sectors have been proposed to explain EWSB. The simplest extension is a two Higgs-doublet model (2HDM). The minimal supersymmetric standard model (MSSM) employs the type-II 2HDM, where at leading order one doublet couples to the up-type fermions and the other couples to the down-type fermions [3]. The two Higgs doublet fields manifest themselves as two charged Higgs bosons ($H^{\pm}$) and three neutral Higgs bosons (h^0, H^0, A^0).

In 2HDM and MSSM, the top quark is allowed to decay into a charged Higgs boson (H^+) [88] and a bottom quark. The tree level branching ratio of top quarks to H^+, $\mathcal{B}(t \to H^+b)$, is a function of the H^+ mass (m_{H^+}) and $\tan\beta$. The parameter $\tan\beta$ is the ratio of vacuum expectation values of the two Higgs doublets. In MSSM, $\mathcal{B}(t \to H^+b)$ also depends on extra parameters related to the masses and couplings of the other supersymmetric particles. The $\mathcal{B}(t \to H^+b)$ is relatively large if $\tan\beta$ is small ($\lesssim 1$) or large ($\gtrsim 15$) [4]. At low $\tan\beta$, H^+

predominantly decays into $c\bar{s}$ for low m_{H^+} ($\lesssim 130$ GeV/c^2) and $t^*\bar{b}$ ($\to Wb\bar{b}$) [89] for higher m_{H^+}. In the high $\tan\beta$ region, the H^+ decays into $\tau^+\nu$ almost 100% of the time.

At Tevatron collider experiments, H^+ searches have been performed for the $H^+ \to \tau\bar{\nu}$ in $t\bar{t}$ decays. Some searches placed direct upper limits on $\mathcal{B}(t \to H^+b)$ by taking advantage of the expectation that $\mathcal{B}(H^+ \to \tau\bar{\nu}) = 1.0$ at high $\tan\beta$ [90]. Other searches set limits on the MSSM parameter plane (m_{H^+}, $\tan\beta$) using inclusive H^+ decay branching ratios in the MSSM [91]. The various H^+ final states supplement the SM $t\bar{t}$ decay channels. The previous searches focused on measuring deviations from the SM prediction for the $t\bar{t}$ production and decay, rather than reconstructing H^+ bosons.

In this Letter, we report on the first direct search for $H^+ \to c\bar{s}$ produced in top quark decays by fully reconstructing the $c\bar{s}$ mass. The final state of $H^+ \to c\bar{s}$ is mostly two jets, as is the hadronic decay of the W boson [92] in SM top quark decays. The search is performed by looking for a second peak in the dijet mass spectrum (in addition to that from the W boson) in top quark decays. In the SM, each top quark decays into a W boson and a b-quark exclusively. In this analysis we use the lepton+jets $t\bar{t}$ sample [93], where in the SM one W decays to quarks ($q\bar{q}'$) and the other W decays to $e\bar{\nu}$ or $\mu\bar{\nu}$. Each final state quark is assumed to form a hadronic jet; the jets are clustered using a cone algorithm with a cone radius ΔR ($= \sqrt{(\Delta\eta)^2 + (\Delta\phi)^2}$) of 0.4 [67]. This lepton+jets sample has a good signal-to-background ratio for $t\bar{t}$ and is ideal for dijet mass analysis.

The CDF II experiment at the Fermilab Tevatron measures the products of proton-antiproton collisions at $\sqrt{s} = 1.96$ TeV. The lepton momentum is measured using an eight-layer silicon microstrip detector and a cylindrical drift chamber immersed in a 1.4 T magnetic field. The energies of electrons and jets are measured using calorimeters with acceptance up to pseudorapidity as of $|\eta| = 3.6$ [94]. Charged particle detectors outside the calorimeter identify muon candidates up to $|\eta| = 1.0$. Details of CDF II can be found elsewhere [78].

Lepton+jets $t\bar{t}$ events are selected by requiring an electron or a muon with $p_T > 20$ GeV within $|\eta|$=1 and by requiring missing transverse energy larger than 20 GeV to account for the neutrino [95]. Then, the four most energetic jets (called leading jets) within $|\eta| < 2.0$ are required to have $E_T > 20$ GeV after jet energy corrections [67]. In addition, at least two of the leading jets are required to contain a long-lived hadron containing a b-quark [71] by demanding that these jets contain tracks forming a displaced secondary vertex (called a b-tag).

The SM processes are regarded as backgrounds for the H^+ search. The largest background is W bosons in SM $t\bar{t}$ events (92% of the total background). The rest of the SM processes are referred to as non-$t\bar{t}$ backgrounds. These include W+jets, multijets, Z+jets, diboson (WW, WZ, ZZ), and single top events. Details of the non-$t\bar{t}$ background estimation method are given in [71]. Assuming a $t\bar{t}$ cross section of 6.7 pb [83] and a top quark mass of 175 GeV/c^2, we expect 152.6 ± 25.0 events from SM $t\bar{t}$ production and 13.9 ± 7.5 events from non-$t\bar{t}$ backgrounds in the 2.2 fb^{-1} CDF II data sample.

The mass of the H^+ candidate is directly reconstructed using the two jets. The mass resolution is improved by reconstructing the $t\bar{t}$ event as a whole with a kinematic fitter used for the precision top quark mass measurement described in Ref. [78]. The original kinematic fitter is modified for the H^+ search. In the fitter, the lepton, the missing E_T (from a neutrino), and the four leading jets are assigned to the decay particles from the $t\bar{t}$ event, and the quality of the assignment is evaluated using this χ^2.

$$\begin{aligned}\chi^2 &= \sum_{k=jjb,l\nu b} \frac{(M_k - M_t)^2}{{\Gamma_t}^2} + \sum_{i=l,4\text{jets}} \frac{(p_T^{i,\text{fit}} - p_T^{i,\text{meas}})^2}{{\sigma_i}^2} \\ &+ \frac{(M_{l\nu} - M_W)^2}{{\Gamma_W}^2} + \sum_{j=x,y} \frac{({p_j}^{UE,\text{fit}} - {p_j}^{UE,\text{meas}})^2}{{\sigma_{UE}}^2} \qquad \text{(F.1)}\end{aligned}$$

The χ^2 is minimized by constraining leptonic W final state ($l\nu$) to have the W invariant mass (80.4 GeV/c^2) [16] and both top quark final states ($bl\nu$ and bjj) to have the same top quark mass of 175 GeV/c^2. No constraint is imposed on the dijet mass of the hadronic boson (jj). In the mass constraints, the transverse energies of the final state objects ($p_T^{i,\text{meas}}$) are allowed to vary within measurement uncertainties (σ_i). The unclustered energy ($p_j^{UE,\mathrm{meas}}$) is sum of measured transverse energies not included in the leading jets E_T and is used to correct the missing E_T. In the jet assignment, b-tagged jets are assigned to the b-quarks. The jets assigned to the b-quarks are called b-jets, and the other two jets are called h-jets. If the $t\bar{t}$ event has more than two b-tagged jets, the jets with the best χ^2 are assigned to b-quarks. Then, we reconstruct the mass of hadronic boson using two h-jets with fit energies ($p_T^{i,\mathrm{fit}}$). In this kinematic event reconstruction, only 55% of the SM $t\bar{t}$ events have correctly matching jets. The wrong jet-parton assignments dominantly come from hard radiation jets which are selected as leading jets and from the falsely b-tagged jets originating from the hadronic decays of W bosons.

The expected dijet mass distributions of H^+ and W in top quark decays are produced using the PYTHIA generator [65] and the full CDF II detector simulation. The ALPGEN generator [74] with the PYTHIA parton shower simulation is used for non-$t\bar{t}$ backgrounds. In the simulation sample, the H^+ is forced to decay solely into $c\bar{s}$ with zero width and with masses ranging from 60 to 150 GeV/c^2.

The simulation shows that the reconstructed H^+ has a significant low-mass tail, which is predominantly caused by final-state gluon radiation (FSR) from the hadronic decays of the Higgs boson. The hard FSR results in more than four final state jets in a lepton+jets $t\bar{t}$ event. To recover the energy loss due to the FSR, the fifth most energetic jet is merged with the closest jet among the four leading ones if the pair has a ΔR distance smaller than 1.0, provided that the fifth most energetic jet has $E_T > 12$ GeV and $|\eta| <2.4$. Merging the fifth jet results in better jet energy resolution and improves the m_{H^+} resolution by approximately 5% in more than four final jets events for 120 GeV/c^2 Higgs sample.

In the CDF II data sample of 2.2 fb^{-1}, we observe 200 $t\bar{t}$ candidates in the lepton+jets decay channel. No significant excess is observed in the dijet invariant mass of top quark decays. Figure F.1 shows that the observed dijet mass distribution agrees with the SM expectations. Hence, we extract upper limits on $\mathcal{B}(t \to H^+b)$ using a binned likelihood fit on the dijet mass distribution.

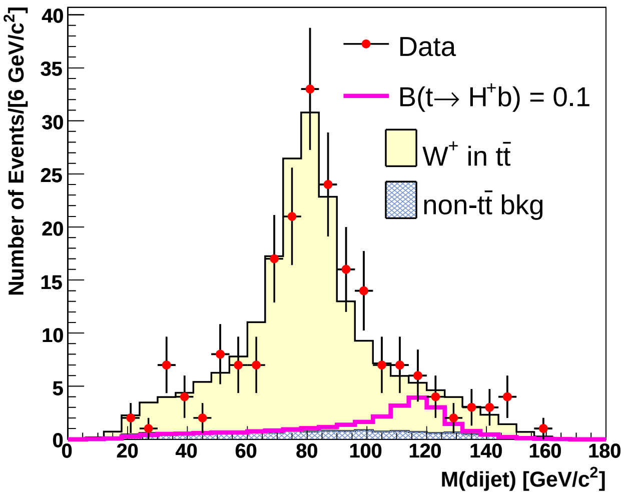

Figure F.1: Observed dijet mass distribution (crosses) compared with background distributions of W bosons (filled) and non-$t\bar{t}$ processes (cross hatched) in CDF II data sample of 2.2 fb^{-1}; the background distributions are added on top of each other. An example of the dijet mass distribution from 120 GeV/c^2 H^+ bosons (bold line) is overlaid assuming $\mathcal{B}(t \to H^+b) = 0.1$, which is about the 95% C.L. upper limit on $\mathcal{B}(t \to H^+b)$.

The binned likelihood (LH) function is constructed employing Poisson probabilities:

$$\mathcal{L} = \prod_i \frac{\nu_i^{n_i} \times e^{-\nu_i}}{n_i!} \times G(N_{\rm bkg}, \sigma_{N_{\rm bkg}}). \tag{F.2}$$

The probability of finding events in the mass bin i comes from a set of simulated dijet mass distributions of H^+, W, and non-$t\bar{t}$ backgrounds. These distributions are called templates. The Poisson probability (P^i) in each bin is computed from the number of observed events, n_i, and from the number of expected events, $\nu_i = P^i_{H^+} \times N_{H^+} + P^i_W \times N_W + P^i_{\rm bkg} \times N_{\rm bkg}$, where N_{H^+}, N_W, and $N_{\rm bkg}$ are parameters representing the total number of events in each template category. The minimization of $-\ln \mathcal{L}$ gives the most probable values for N_{H^+}, N_W, and $N_{\rm bkg}$. In the LH fit, N_{H^+} and N_W are free to vary, however, the non-$t\bar{t}$ background ($N_{\rm bkg}$) is estimated independently and is allowed to vary within its Gaussian uncertainty ($\sigma_{\rm N_{bkg}}$). Based on the number of events from the LH fit, a $\mathcal{B}(t \to H^+b)$ is extracted assuming $\mathcal{B}(H^+ \to c\bar{s}) = 1$. In Figure F.1, dijet mass distributions of the SM events are normalized by the likelihood fit to the observed dijet mass distribution with $\mathcal{B}(t \rightarrow H^+b)$ fixed to 0.

The sources of systematic uncertainty in the extracted $\mathcal{B}(t \rightarrow H^+b)$ include uncertainties in the jet energy scale corrections [67], initial state and final state radiation, modeling of the non-$t\bar{t}$ background, choice of event generators in simulation. These systematic sources perturb the shape of the dijet mass and cause a shift in the result of the LH fit. The shift in the resulting $\mathcal{B}(t \rightarrow H^+b)$ is estimated using "pseudoexperiments" of the perturbed and unperturbed dijet mass distributions for each systematic source; the pseudoexperiments are generated by the bin-to-bin Poisson fluctuations of the simulated dijet mass distributions. The dominant systematic uncertainty originates from the choice of event generators in the simulation, unless m_{H^+} is close to m_W, in which case the jet energy scale uncertainty dominates. The other systematic uncertainties from data/MC differences in b-tagging rates and top quark mass constraints in $t\bar{t}$ reconstruction are negligible compared to the uncertainties from the perturbed dijet mass shape.

The individual systematic uncertainties are combined in quadrature. The total systematic uncertainty ($\Delta\mathcal{B}(t \rightarrow H^+b)$) is represented by a nuisance parameter which adds to the branching ratio and has a Gaussian prior probability density function (pdf) with width $\Delta\mathcal{B}(t \rightarrow H^+b)$. We eliminate this nuisance parameter by Bayesian marginalization [96] and obtain a posterior pdf in $\mathcal{B}(t \rightarrow H^+b)$ assuming a uniform prior pdf in $0 \leq \mathcal{B}(t \rightarrow H^+b) \leq 1$. The expected upper limits on $\mathcal{B}(t \rightarrow H^+b)$ with 95% C.L. are derived from a thousand pseudoexperiments using the SM backgrounds events for each m_{H^+}.

The upper limits on $\mathcal{B}(t \rightarrow H^+b)$ at 95% C.L. show a good agreement between the observation and the SM expectation. The upper limits in Figure F.2 includes the systematic uncertainty in $\mathcal{B}(t \rightarrow H^+b)$. Since the LH fit has very little sensitivity for $m_{H^+} \approx m_W$, the upper limits around 80 GeV/c^2 H^+ are omitted in the Figure. The exact values of the upper limits in the Figure F.2 are listed in Table F.1.

This analysis can set model-independent limits for anomalous scalar charged bosons production in top quark decays. Besides the assumption that a scalar boson decays only to $c\bar{s}$ with zero width, no model-specific parameter is used in

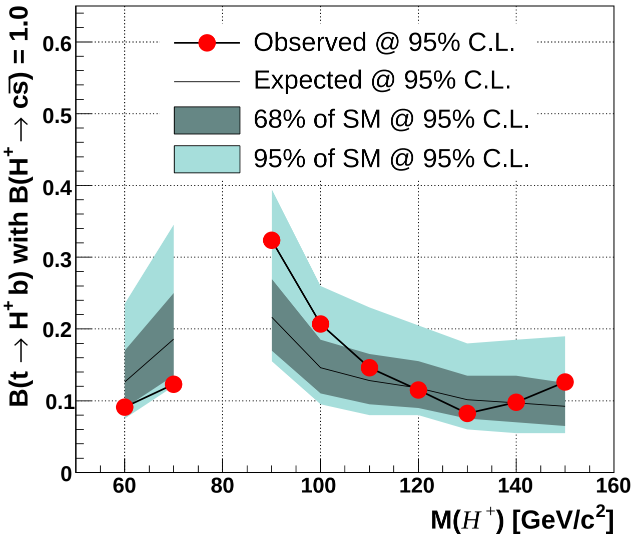

Figure F.2: The upper limits on $\mathcal{B}(t \to H^+b)$ at 95% C.L for charged Higgs masses of 60 to 150 GeV/c^2 except a region for $m_{H^+} \approx m_W$. The observed limits (points) in 2.2 fb^{-1} CDF II data are compared to the expected limits (solid line) with 68% and 95% uncertainty band.

this analysis. Therefore any generic charged boson would make a secondary peak in the dijet mass spectrum if it decays into a dijet final state like the $H^+ \to c\bar{s}$ in top quark decays. Here, we extend the search below the W boson mass [20] down to 60 GeV/c^2 for any non-SM scalar charged boson produced in top quark decays, $t \to X^+(\to u\bar{d})b$. This process is simulated for the CDF II detector and is similar to $H^+ \to c\bar{s}$. In the simulation, we obtain a better dijet mass resolution for $u\bar{d}$ decays than for the $c\bar{s}$ decays. The difference in the mass resolution comes from the smaller chance of false b-tagging from light quark final states of X^+ than

m_{H^+}(GeV/c^2)	60	70	90	100	110	120	130	140	150
Expected	0.13	0.19	0.22	0.15	0.13	0.12	0.10	0.10	0.09
Observed	0.09	0.12	0.32	0.21	0.15	0.12	0.08	0.10	0.13

Table F.1: Expected and Observed 95% C.L. upper limits on $\mathcal{B}(t \to H^+b)$ for H^+ masses of 60 to 150 GeV/c^2.

the $c\bar{s}$ decays, thus resulting in a smaller ambiguity of jet-parton assignments in the $t\bar{t}$ reconstruction. Consequently, the upper limits on $\mathcal{B}(t \rightarrow X^+(\rightarrow u\bar{d})b)$ are lower than the limits on $\mathcal{B}(t \rightarrow H^+(\rightarrow c\bar{s})b)$ regardless of the charged boson mass.

In summary, we have searched for a non-SM scalar charged boson, primarily the charged Higgs boson predicted in the MSSM, in top quark decays using lepton+jets $t\bar{t}$ candidates. This is the first attempt to search for $H^+ \rightarrow c\bar{s}$ using fully reconstructed charged Higgs bosons. In the CDF II data sample of 2.2 fb^{-1}, we find no evidence of charged Higgs bosons in the dijet mass spectrum of the top quark decays. Hence, upper limits on $\mathcal{B}(t \rightarrow H^+b)$ with 95% C.L. are placed at 0.1 to 0.3 assuming of $\mathcal{B}(H^+ \rightarrow c\bar{s}) = 1.0$ for charged Higgs masses of 60 to 150 GeV/c^2. This analysis also yields conservative upper limits on any non-SM scalar charged boson X^+ production from top quarks. Based on simulation, we find that the upper limits on the branching ratio $\mathcal{B}(X^+ \rightarrow u\bar{d})$ are always better than the upper limits on $\mathcal{B}(H^+ \rightarrow c\bar{s})$.

We thank the Fermilab staff and the technical staffs of the participating institutions for their vital contributions. This work was supported by the U.S. Department of Energy and National Science Foundation; the Italian Istituto Nazionale di Fisica Nucleare; the Ministry of Education, Culture, Sports, Science and Technology of Japan; the Natural Sciences and Engineering Research Council of Canada; the National Science Council of the Republic of China; the Swiss National Science Foundation; the A.P. Sloan Foundation; the Bundesministerium für Bildung und Forschung, Germany; the Korean Science and Engineering Foundation and the Korean Research Foundation; the Science and Technology Facilities Council and the Royal Society, UK; the Institut National de Physique Nucleaire et Physique des Particules/CNRS; the Russian Foundation for Basic Research; the Ministerio de Ciencia e Innovación, and Programa Consolider-Ingenio 2010, Spain; the Slovak R&D Agency; and the Academy of Finland.